



저작자표시-비영리-변경금지 2.0 대한민국

이용자는 아래의 조건을 따르는 경우에 한하여 자유롭게

- 이 저작물을 복제, 배포, 전송, 전시, 공연 및 방송할 수 있습니다.

다음과 같은 조건을 따라야 합니다:



저작자표시. 귀하는 원저작자를 표시하여야 합니다.



비영리. 귀하는 이 저작물을 영리 목적으로 이용할 수 없습니다.



변경금지. 귀하는 이 저작물을 개작, 변형 또는 가공할 수 없습니다.

- 귀하는, 이 저작물의 재이용이나 배포의 경우, 이 저작물에 적용된 이용허락조건을 명확하게 나타내어야 합니다.
- 저작권자로부터 별도의 허가를 받으면 이러한 조건들은 적용되지 않습니다.

저작권법에 따른 이용자의 권리는 위의 내용에 의하여 영향을 받지 않습니다.

이것은 [이용허락규약\(Legal Code\)](#)을 이해하기 쉽게 요약한 것입니다.

[Disclaimer](#)

공학박사학위논문

고내구성 저가 고분자 전해질 연료전지를
위한 계면 구조 설계 및 제작

Interfacial Structure Design and Fabrication
for Durable and Low-cost Polymer Electrolyte Fuel Cells

2022 년 8 월

서울대학교 대학원

기계항공공학부

최 지 우

고내구성 저가 고분자 전해질 연료전지를 위한 계면 구조 설계 및 제작

Interfacial Structure Design and Fabrication
for Durable and Low-cost Polymer Electrolyte Fuel Cells

지도교수 최 만 수

이 논문을 공학박사 학위논문으로 제출함

2022 년 4 월

서울대학교 대학원

기계항공공학부

최 지 우

최지우의 공학박사 학위논문을 인준함

2022 년 6 월

위 원 장 : 이 윤 석 (인)

부위원장 : 최 만 수 (인)

위 원 : 고 승 환 (인)

위 원 : 장 세 근 (인)

위 원 : 이 건 희 (인)

Interfacial Structure Design and Fabrication for Durable and Low-cost Polymer Electrolyte Fuel Cells

Jiwoo Choi

Department of Mechanical Engineering

The Graduate School

Seoul National University

Abstract

Polymer electrolyte fuel cells (PEFCs) have been spotlighted as eco-friendly energy sources. Over the past few decades, intensive research has been conducted to fabricate a highly efficient membrane electrode assembly (MEA), and as a result, the technical maturity has reached the commercialization stage. However, since expensive catalysts and membranes are essential to manufacturing MEA, the capital cost of PEFCs is not yet competitive in the market. In addition, the low stability of MEA, especially the chemical degradation of ion-conducting polymers used in

membranes and electrodes, is also a crucial constraint for successful commercialization. Generally, the current approaches to cost reduction and lifetime enhancement of MEA can severely decrease the performance of PEFCs. Therefore, a strategy for manufacturing an MEA having low fabrication cost and high stability while improving the efficiency of a fuel cell is essential. This dissertation aims to introduce novel interfacial structure approaches to develop durable and low-cost MEAs with increased power performance.

First, to enhance the chemical durability and power performance of PEFCs, simultaneously, a multi-functional structure was introduced at the interface between the membrane and electrode. To fabricate the interface structure, ion-conducting polymer resin and radical scavenging nano-sized particles were sprayed using the electrospray deposition (ESD) method. Unlike other deposition methods, the fine droplets formed by ESD are stacked in a dendritic structure rather than a membrane shape due to van der Waals force and electrostatic force. As a result, the structure increased electrochemical surface area (ECSA), and a micro-sized void space enhanced oxygen transport within the catalyst layer (CL). Also, the structure prevented dehydration of MEA, maintaining the ion conductivity of the membrane. Most importantly, the structure enhanced the chemical

stability of MEA by quenching the harmful radicals generated in the electrodes. The efficiency and chemical stability of the MEA was examined by various analysis, including the in-situ and ex-situ accelerated degradation test.

Secondly, a strategy of reducing expensive catalyst content at the electrode was introduced by fabricating the electrode without an ionomer-binder. To prepare the electrode, one-dimensional nanostructures were grown vertically and an ultra-low amount of catalyst was deposited uniformly. Applied as a cathode for anion exchange membrane fuel cells (AEMFCs), The electrode dramatically enhanced the mass transport of the reactants to the catalytic surface via its short diffusion pathway and ionomer-free nature. The electrochemical analysis was conducted between the ionomer-free electrode and a conventional electrode, which consisted of randomly dispersed carbon-supported nanoparticle catalysts and an ionomer. Also, water consumption and oxygen transport characteristics of AEMFC with the ionomer-free electrode at the cathode were intensively investigated by varying the electrode thickness and compositions. Moreover, through the durability test, it was found that the prepared ionomer-free catalyst layer was more stable than the conventional one.

Thirdly, the surface modification technique was introduced to fabricate a highly efficient MEA using a low-cost hydrocarbon-based membrane. Using a plasma etching process and polymeric stencil with regular opening, the membrane was chemically and mechanically modified. Various bonding strength tests were conducted between the hydrocarbon-based membrane and conventional perfluorosulfonic acid (PFSA) polymer, and it was confirmed that the oxygen functional group introduced on the surface of the membrane improved the bonding strength. To verify the commercial applicability of the hydrocarbon-based membrane and the surface modification method, MEA was prepared by the decal transfer method of the electrode. In the analysis applying a transmission line model, it was found that the thoroughly contacted interface not only reduces the resistance at the interface but also facilitates proton conduction in the catalyst layer. Furthermore, a detailed analysis of the limiting current density verified that the modified MEA had a lower oxygen transport resistance.

Keyword : Polymer electrolyte fuel cells, Interface Structures, Chemical durability, Cost reduction, Oxygen transport

Student Number : 2016-23467

Table of Contents

Abstract.....	i
Table of Contents.....	v
List of Tables	viii
List of Figures.....	ix
Nomenclature	xvii
 Chapter 1. Introduction	 1
1.1. Background.....	2
1.1.1. Polymer electrolyte fuel cells (PEFCs)	2
1.1.2. Membrane–electrode assembly (MEA)	4
1.1.3. Performance	7
1.1.4. Durability	8
1.2. Research objectives.....	13
1.3. References.....	16
 Chapter 2. Multi–Functional Dendritic Structures for Enhanced chemical Durability and Efficiency of PEMFCs.....	 28
2.1. Introduction	29
2.2. Experimental methods.....	33
2.2.1. Fabrication of the dendritic Nafion [®] /CeO ₂ structures	33
2.2.2. MEA and single–cell preparation.....	33
2.2.3. Characterization	34

2.3. Results and discussion	38
2.3.1. Dendritic structures via ESD process and the structure characterization	38
2.3.2. Analysis of single-cell performance	54
2.3.3. Evaluation of the chemical durability of the modified membrane	64
2.4. Conclusion	69
2.5. References.....	70

Chapter 3. 1-D Ionomer-free Electrode with Ultra-low Catalyst

Loading	79
3.1. Introduction	80
3.2. Experimental methods.....	85
3.2.1. Preparation of ionomer-free electrode with a catalyst coated 1-D nanostructures	85
3.2.2. MEA preparation.....	86
3.2.3. Characterization	87
3.3. Results and discussion	90
3.3.1. Fabrication and characterization of the nanostructured gas diffusion electrode	90
3.3.2. Fuel cell evaluation from mass transport and electrode durability perspective	95
3.3.3. Voltage drop due to the water shortage and optimization of electrode thickness	103
3.4. Conclusion	113
3.5. References.....	115

Chapter 4. Chemical and Mechanical Surface modification for Highly Efficient and Low-cost Hydrocarbon-based PEFCs 123

4.1. Introduction	124
4.2. Experimental methods.....	128
4.2.1. Preparation of the modified samples and MEAs	128
4.2.2. Electrochemical analysis.....	130
4.2.3. Physical and chemical characterization	132
4.3. Results and discussion	136
4.3.1. Chemical and mechanical modification and membrane characterization.....	136
4.3.2. Analysis of the improved interfacial adhesion	148
4.3.3. Evaluation of the electrochemical characteristics	154
4.4. Conclusion	166
4.5. References.....	167
 Chapter 5. Conclusion	 176
 Acknowledgments	 179
 초록 (Abstract in Korean)	 180

List of Tables

Table 2.1	Summary of the current–voltage (I–V) performance and the EIS fitted values.	61
Table 3.1.	Comparison of MEA compositions and key parameters between the previously reported AEMFCs and this study	99
Table 4.1.	Water uptake and swelling ratio of the membranes	147
Table 4.2.	Summary of Key parameters from Figure 4.9. (a–c) and Figure 4.11.....	165

List of Figures

Figure 1.1. The schematic illustration of MEA.....	11
Figure 1.2. Main losses of PEFCs	12
Figure 2.1. (a) Schematic of electrospray deposition (ESD)experimental set-up. The inset image illustrates the cone-jet mode at the nozzle tip. (b) Schematic diagram for ESD process, and (c) the 3-D image of the completed dendritic Nafion®/CeO ₂ structure. The surface morphological SEM images of the fabricated structure with 1.0 h deposition time with (d) low-magnification and (e) high-magnification. (f) The structural characteristics of inter-structure spacing and the height of the fabricated structures with regard to deposition time.....	44
Figure 2.2. TEM images of CeO ₂ nanoparticles under (a) low magnification and (b) high magnification.	45
Figure 2.3. A surface image of the Nafion®/CeO ₂ structure on the Nafion® 211 membrane by using a conventional air-spray method... 46	46
Figure 2.4. Cross-sectional SEM images of the Nafion®/CeO ₂ structures after deposition times of (a) 0.5 h, (b) 1.0 h and, (c) and 2.0 h.	47
Figure 2.5. Universal testing machine (UTM) based mechanical stability	

test results of the reference Nafion® 211 membrane with and without heat treatment and the modified Nafion® 211 membrane with NCS-1.0 (a) stress-strain curves, (b) cross-sectional SEM images and (c) summary of the UTM based mechanical test. 48

Figure 2.6. (a) The cross-sectional SEM image of Nafion®/CeO₂ structures and BSE mode SEM images of Nafion®/CeO₂ structures with (b) low-magnification and (c) high magnification. The surface images of the MEA after catalyst layer deposition onto the modified membrane with (d) low-magnification, (e) high-magnification and (f) FIB-assisted cross-sectional image. 49

Figure 2.7. (a) The cross-sectional SEM image of Nafion®/CeO₂ structures and its correspondent EDS mapping images of (b) sulfur and (c) cerium, respectively. 50

Figure 2.8. (a) The surface and (b) cross-sectional SEM images of the MEA with flat, pure Nafion® 211 membrane. 51

Figure 2.9. Schematic illustrations for multifunctional effects of the modified MEA with Nafion®/CeO₂ structure for efficient removal of generated water and radicals. 52

Figure 2.10. XPS spectra of ceria particles (< 25 nm, Sigma Aldrich) in this study; (a) high-resolution XPS spectra of Ce 3d and (b) XPS analysis of Ce ³⁺ and Ce ⁴⁺ ion concentration.	53
Figure 2.11. (a) Polarization curves at 70 ° C with flow rate (H ₂ /Air = 150/350 cc/min) and (b) corresponding EIS spectra at 0.6 V. (c) Polarization curves with low Rh conditions (30% and 60%) and (b) corresponding EIS spectra at 0.6V.	59
Figure 2.12. Equivalent circuit model for the cathodic reaction of the PEMFC (R ₁ = internal membrane resistance, R _{ct} = charge transfer resistance of the cathode, CPE = constant phase element of the cathode, and W ₁ = Warburg impedance).	60
Figure 2.13. (a) Current density–voltage (J–V) curves and the (b) EIS spectra for the prepared MEAs including the MEA with Nafion®/TiO ₂ structures with varying the RH condition. (c) Summary of I–V performance and EIS fitted values	62
Figure 2.14. Cyclic voltammetry (CV) measurements of the reference MEA and the MEA with NCS–1.0.	63
Figure 2.15. (a) The OCV decay spectra over 276h testing under accelerated condition and corresponding (b) hydrogen crossover current density from linear sweep voltammetry (LSV)	

measurements and (c) maximum power density with the prepared MEAs. (d) Fluorine ion emission rate (FER) from 72 h Fenton' s test with the prepared membranes.....	67
Figure 2.16. The OCV decay spectra from the OCV holding tests (over 100 h) with the prepared MEAs including the MEA with Nafion®/TiO ₂ structures.	68
Figure 3.1. (a) Schematic illustrations of the fabrication process of VGDE. (b) Surface morphological SEM images VGDE containing the silver catalyst layer (inset: high magnified images). (c) Schematic illustrations of the fabrication process of the conventional electrode. (d) Surface morphological SEM image of the conventional porous electrode containing Ag/C catalyst and ionomer	92
Figure 3.2. Surface morphological SEM images of (a) GDL and (b) hydrothermally synthesized ZnO on GDL (ZnO/GDL).	93
Figure 3.3. XPS spectra of (a) Zn 2p and (b) Ag 3d of GDL/ZnO and VGDE. (c) TEM and EDX mapping images	94
Figure 3.4. (a) Polarization curves of MEAs containing a CGDE (0.1 mg _{Ag} cm ⁻²) and VGDE (0.06 mg _{Ag} cm ⁻²). Both MEAs were sufficiently activated under constant voltage-operated	

conditions. (b)EIS spectra at 0.1 V and 0.1 A cm ⁻² correspond to MEAs containing CGDE and VGDE. (c) Schematic illustrations of the oxygen transport behaviors of CGDE VGDE.....	98
Figure 3.5. Linear sweep voltammograms of a CGDE and VGDE_12h (0.06 mg _{Ag} cm ⁻²)	100
Figure 3.6. Cyclic voltammograms of Ag CGDE (0.10 mg _{Ag} cm ⁻²) and Ag VGDE_12h (0.06 mg _{Ag} cm ⁻²)	101
Figure 3.7. Spectra of the voltage decay under an operating condition of 0.3 A cm ⁻² for MEAs containing CGDE and VGDE.....	102
Figure 3.8. Polarization curves of MEAs containing silver–deposited GDL (Ag/GDL) and MEA containing CGDE at the cathode.	109
Figure 3.9. (a) Cross–sectional SEM images of the ZnO nanorod on GDL, which was synthesized at 80 °C for 6, 12, 18, and 36 h, in regular order. (b) The measured length of the ZnO nanorods of different growth times. (c) AEMFC polarization curves of MEAs containing VGDEs with different ZnO growth times (0, 6, 12, 18, and 36 h)	110
Figure 3.10. Polarization curves of (a) MEAs containing VGDE_36h with different silver catalyst loadings and (b) MEAs containing	

VGDE_36h and platinum-coated VGDE_36h instead of the silver layer.....	111
Figure 3.11. AEMFC polarization curves of (a) MEAs containing VGDE_36h, ionomer-sprayed VGDEs, (b) 30 and 50 μ m MEAs containing VGDE_12h and VGDE_36h. (c) limiting current density concerning the electrode thickness shown in Figure 5 (c).	112
Figure 4.1. Schematic of chemical and mechanical modification process.....	140
Figure 4.2. Cross-sectional SEM images of MC-HC for (a) 60 min, (b) 90 min, and (c) 120 min.....	141
Figure 4.3. Cross-sectional SEM images of (a) the reference, (b) C-HC, and (c) MC-HC. (d) C1s XPS spectra for the samples of Figure 4.3. (a-c). measured proton conductivity at 80 $^{\circ}$ C	142
Figure 4.4. Chemical structure of BPSH-40.....	143
Figure 4.5. Water contact angle on the (a) reference, (b) C-HC, and (c) MC-HC	144
Figure 4.6. Stress-strain curves of the membrane and summary of the key parameters.....	145
Figure 4.7. (a) schematic illustration of 180 $^{\circ}$ peeling test and peel-off	

strength, (b) resultant adhesion strength, and (c) F1s XPS spectra at the surface of HC membrane surface after the test. (d) schematic illustration of shear testing (inset) and the resultant maximum shear stress. (e) Digital images of the reference, C-HC, and MC-HC after shear testing. (f) schematic illustration of the decal-transfer process and (g) catalyst transfer yield according to the pressure for the reference, C-HC, and MC-HC..... 146

Figure 4.8. Digital images of the HC membranes and decal film after the decal-transfer process 152

Figure 4.9. (a) Polarization curves and (b) EIS spectra at 0.6 V with hydrogen/air condition for the reference, C-HC, and MC-HC. (c) EIS spectra at 0.2 V with hydrogen/nitrogen condition. (d) Cross-sectional SEM images for MEAs after decal transfer process 153

Figure 4.10. LSV spectra for reference, C-HC, and MC-HC..... 160

Figure 4.11. CV spectra for reference, C-HC, and MC-HC..... 161

Figure 4.12. Limiting current density as a function of dry mole fraction of oxygen according to outlet pressure for (a) reference, (b) C-HC, and (c) MC-HC..... 162

Figure 4.13. (a) Total oxygen transport resistance as a function of outlet pressure, and (b) pressure-dependent and -independent oxygen transport resistance at 101kPa	163
Figure 4.14. Surface images of CL for MEAs of reference, C-HC, and MC-HC with low magnification (a, b, and c, respectively) and high magnification (d, e, and f, respectively)	164

Nomenclature

Alphabetical and Greek letters

E°	Standard electrode potential
q_{Pt}	The charge due to oxidation of a monolayer of adsorbed hydrogen on Pt
Γ	The charge required to reduce a monolayer of protons on Pt ($210 \mu C cm^{-2}$)
L	Pt loading at the cathodes
$R_{membrane}$	Ohmic resistance of the MEA
R_{LF-HF}	Diameter of the Nyquist semi-circle
C	Fluorine concentration
V	The volume of the solution
t	The test time
m	The membrane weight after drying
M_F	The molecular weight of fluorine
R_{ct}	The charge transfer resistance
mg_{Pt}	The weight of pt catalyst at the cathode
mg_{Ag}	The weight of Ag catalyst at the cathode
$mg_{ionomer}$	The weight of the ionomer at the cathode
σ	In-plane conductivity of the membrane

D	the distance between the electrodes of four-probed equipment
R	The resistance of the membrane
A	the cross-sectional area of the membrane
R₀	The the sum of the resistance of cell elements including the interface
R_{cl}	The ohmic resistance across the catalyst layer
R_t	The total oxygen transport resistance

Chapter 1. Introduction

1.1 Background

1.1.1 Polymer electrolyte fuel cells (PEFCs)

Since the Industrial Revolution in the late 18th century, the utilization of energy has been essential to all industrial areas, including transportation, and its importance has grown to this day. However, with industrial development and the growing need for fossil fuels, greenhouse gases such as CO₂ have caused global climate change, including waves, droughts, and floods, and threatened humanity. Therefore, research on eco-friendly renewable energy for both industrial development and environmental preservation has been conducted.¹ For sustainable energy production, renewable energy sources, such as solar and wind, have been proposed as alternatives, and the production of green energy fuels including hydrogen has been actively studied. And, in this regard, the development of fuel cells that can convert chemical energy into electrical energy without carbon emissions is emerging as an important task for the utilization of energy.²⁻³

Fuel cells are divided into five groups depending on the type of electrolyte used and the operating temperature, which are solid oxide fuel cells (SOFCs), molten carbonate fuel cells (MCFCs), phosphoric acid fuel cells (PAFCs), alkaline fuel cells (AFC), and polymer

electrolyte fuel cells (PEFCs).⁴ Among them, PEFCs are in the spotlight as the most promising fuel cells due to their low operating temperature (<100°C), high power efficiency, and fast start-up characteristics. Due to intensive research by industry and academia over the past few decades, PEFCs have already entered the commercialization stage in the fields of portable, fixed power generation systems, and transportation applications.⁵⁻⁷

For PEFCs to produce energy, like all other fuel cells, hydrogen and oxygen should be fed to anodes and cathodes, respectively. In these two electrodes, hydrogen oxidation reaction (HOR) and oxygen reduction reaction (ORR) occur, and the electrolyte membrane between the two electrodes transfers ions and prevents gas and electrons from cross-over. All of these reactions can take place in acid and alkali environments as shown in the following reaction formula, and the corresponding fuel cells are referred to as proton exchange membrane fuel cells (PEMFCs) and anion exchange membrane fuel cells (AEMFCs), respectively.⁸

1) PEMFCs

Anode reaction : $2H_2 \rightarrow 4H^+ + 4e^-$ ($E^0 = 0V$)

Cathode reaction : $O_2 + 4H^+ + 4e^- \rightarrow 2H_2O$ ($E^0 = 1.23V$)

Overall reaction : $2H_2 + O_2 \rightarrow 2H_2O$ ($E^0 = 1.23V$)

2) AEMFCs

Anode reaction : $2H_2 + 4OH^- \rightarrow 4H_2O + 4e^-$ ($E^0 = -0.83V$)

Cathode reaction : $O_2 + 2H_2O + 4e^- \rightarrow 4OH^-$ ($E^0 = 0.4V$)

Overall reaction : $2H_2 + O_2 \rightarrow 2H_2O$ ($E^0 = 1.23V$)

1.1.2 Membrane-electrode assembly (MEA)

The most important component of PEFC is the membrane-electrode assembly (MEA) in which an ion-conducting membrane, two catalytic layers (CL), and two gas diffusion layers (GDL) are combined. (**Figure 1.1**) Since the characteristics of MEA are greatly influenced by individual materials, extensive studies are being conducted to develop highly efficient and durable materials. Also, it is widely known that the MEA characteristics can be improved by proper design and fabrication methods.⁹ And, for successful commercialization, the reduction of the capital cost of PEFCs and MEA is another challenge to solve.¹⁰⁻¹¹

CL is the electrochemical reaction site where electrons, ions, and gases coexist. To effectively utilize catalysts and increase the triple-phase boundary (TPB), the conventional electrode has a porous structure with an ion conductive binder and carbon-supported catalysts.¹² The primary purpose of the research in electrode development is to realize highly efficient and durable

electrodes with affordable materials. So far, expensive platinum group metal (PGM) catalysts are commonly used because of the sluggish electrochemical reaction, especially ORR. And the simple use of non-precious metal catalysts or reduction in PGM catalyst loading led to increased kinetics and mass transport overpotential of the PEFC system. Therefore, intensive research has been conducted to develop novel non-precious catalysts to replace precious PGM catalysts or reduce PGM catalyst loading.¹³⁻¹⁵ Also, as various inexpensive materials such as silver can be used as a catalyst in an alkaline environment, AEMFCs are receiving a lot of attention as a promising PEFC system.¹⁶⁻¹⁷ Efforts have also been made to expand the interface between the membrane and the CL to increase the catalyst utilization and the electrochemical surface area (ECSA), as a structural approach.¹⁸⁻¹⁹

The ion conductive membrane is an essential element of MEA. The role of the polymer electrolyte membrane is electrical insulation, gas separation, and most importantly, an ion-conduction such as protons and anions. The membrane is generally composed of a hydrophobic main chain and side chains with ion-conducting sites, and the ions move through the ion clusters and water channels.²⁰⁻²¹ Therefore, the conductivity of the membrane is greatly affected by the hydration of the membrane.²²

For PEMFCs, the perfluorosulfonic acid (PFSA) polymer is the most widely used proton conductive polymer due to its high conductivity, chemical stability, and mechanical robustness. However, the fluorinating process for fabrication of the membrane causes environmental problems and a high material cost of \$500 m⁻² or more (for commercially available Nafion® membranes), and also high gas permeability of the membrane causes chemical degradation of MEA.^{9,23} In this regard, there have been great efforts to develop membranes that are cheaper and have superior membrane properties to commercial PFSA. Especially, non-fluorinated hydrocarbon-based polymer electrolyte membranes (HC-PEMs) have been widely studied.²⁴⁻²⁸ These HC-PEMs are promising electrolyte materials that have several advantages such as low gas permeability, excellent thermal stability, and physical properties.²⁹ Typically, HC-PEMs are based on readily available and inexpensive materials. Also, the eco-friendly synthesis process of HC-PEMs has an advantage over them in terms of reducing production costs by eliminating fluorinating steps. However, more research is needed to apply these promising alternatives to MEA yet because the performance and durability are deteriorated due to the interfacial issues between HC-PEMs and PFSA-CL.³⁰

For AEMFCs, various reports have been introduced to develop anion exchange polymers (AEPs) with high ionic conductivity and chemical–mechanical stability under AEMFC operating conditions. Thanks to these efforts, several PGM–based AEMFCs have been able to achieve promising power density and durability based on the novel AEPs,³¹ such as aryl–ether free polyaromatics,^{32–34} radiation–grafted polyethylene,³⁵ and polynorbornenes.^{36–37} In addition, several AEMFCs based on these novel AEPs exhibited remarkable performance even without the use of PGM–based ORR catalysts.^{38–39} However, the basic material for AEPs has not yet been established, and the commercially available AEPs like FAA–3 (FuMA–Tech) and AS–4 (Tokuyama) used in most AEMFC studies show much inferior properties to the newly developed AEPs.

1.1.3 Performance

PEFCs electrochemically convert chemical energy into electrical energy and efficiency can be defined as cell voltage divided by the reversible voltage. (i.e. the voltage efficiency) However, as the current density increases, voltage loss (i.e. overpotential) occurs, and cell voltage and efficiency decrease. As can be seen in **Figure 1.2**, there are three main voltage losses, which are activation loss, ohmic loss, and concentration loss.^{40–41} 1) The activation loss can be seen

in the low-current density region prominently and is caused by an electrochemical reaction, especially ORR. Therefore, the activation loss is strongly dependent on the catalyst materials and ECSA.⁴²⁻⁴³

2) The ohmic loss shows linear behavior and is caused by the transfer of the ion and electrons. As the ion conductivity is much lower than the electrical conductivity, the ohmic loss is largely dependent on the polymer electrolyte membrane and the humidity of the system.⁴⁴⁻⁴⁶ 3) The concentration loss arises in the high-current density region in which electrochemical reactions occur more actively. The ORR requires more oxygen, but the generated water fills the pores of CL and forms a film on the surface of the catalyst to block oxygen access to the catalyst, which is shown by an increase in concentration loss and a decrease in performance.⁴⁷⁻⁴⁹ In conclusion, to manufacture a high-efficient MEA, it is necessary to develop a material and an MEA structure to effectively reduce such losses.

1.1.4 Durability

The durability of PEFCs is an increasingly pressing priority, especially as fuel-cell vehicles become a feature of our daily lives. Although manufacturers of PEFCs are required to warrant long-term operation (> 5,000 h) with minimal performance loss, current PEFC

technologies still lag far behind the practical demands.^{50–51} Therefore, to expand the lifetime of PEFCs, it is necessary to understand the degradation mechanisms and solve them. Under dynamic operation conditions, MEA can be degraded due to various faulty conditions, which can be largely divided into two main categories depending on the degraded component: electrode and membrane.

At the electrode, the degradation may occur due to excessive water, insufficient reactants, and the inflow of impurities, which causes a decrease in catalytic active sites and a loss of carbon support.⁵² Also, in the case of AEMFC, the ionomer having the phenyl groups in their polymer backbone can strongly adsorb on the metal-based catalyst surface, resulting in deterioration of durability and performance of AEMFCs.^{53–54}

The degradation of the membrane can be induced by mechanical stress, during repeated drying and swelling operating conditions^{55–56}, and by chemical decomposition, due to oxidative hydroxyl (HO^*) and hydroperoxyl (HOO^*) radical attack.^{57–59} These free radicals, generated from the reaction between released cations (e.g. Fe^{2+}) and hydrogen peroxide (H_2O_2) during fuel cell operation, cause the decomposition of the main and side chains of the PFSA membranes resulting in membrane thinning and pinhole formation.^{59–60}

As can be seen above, PEFCs show potential for next generative energy utilization and have already been applied to various commercialization fields. However, there are still many challenges to solve in terms of efficiency, stability, and cost, ranging from material to MEA level. Therefore, research is needed from the development of basic materials to MEA design and manufacturing method, which can be applied to MEA, and this paper introduces an interfacial structure approach for the commercialization of PEFCs.

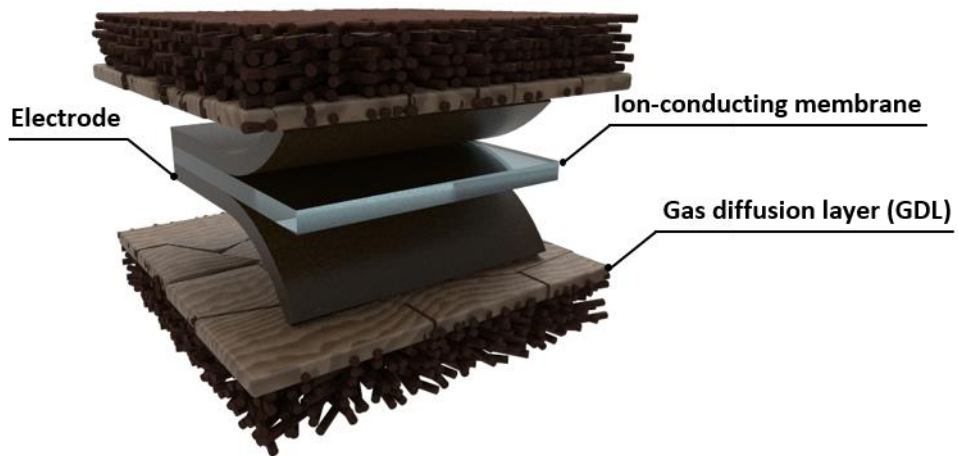


Figure 1.1. The schematic illustration of MEA

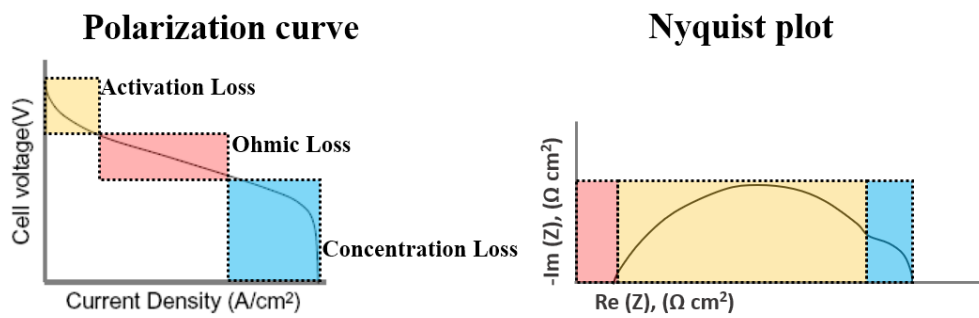


Figure 1.2. Main losses of PEMFCs

1.2. Research objectives

As mentioned above, for the successful commercialization of PEFCs, it is essential to develop technologies applicable to MEA. This thesis introduces novel strategies for forming a functional structure at the interface of the membrane and electrode or GDL. Through this, the challenges of low stability and high manufacturing prices were solved while improving the efficiency of the PEFCs.

In Chapter 2, multifunctional dendritic Nafion[®]/CeO₂ structures were introduced onto the cathode-side of the interface between a membrane and a catalyst layer through electrospray deposition. The dendritic structures enlarged the interfacial contact area between the membrane and the catalyst layer and formed microscale voids between the catalyst layer and gas diffusion medium. This improved the PEMFC performance through the effective utilization of the catalyst and enhanced mass transport of the reactant. In addition to the beneficial effects of the structures, the incorporation of the CeO₂, widely known as a radical scavenger, effectively mitigated the free-radical attack on the outer surface of the membrane, where chemical degradation is initiated by radicals formed during PEMFC operation. These multifunctional effects of the dendritic Nafion[®]/CeO₂ structures on PEMFC performance and durability were investigated

using various in-situ and ex-situ measurement techniques.

In Chapter 3, An ionomer-free electrode containing vertically aligned one-dimensional nanostructures was designed and fabricated for anion exchange membrane fuel cells (AEMFCs) by hydrothermal and vapor deposition processes. The silver-coated zinc oxide (ZnO) nanorod arrays (diameter = ca. 100 nm) were directly aligned with the gas diffusion layer (GDL), and these one-dimensional structures of the electrode enhanced the mass transport of the reactants to the catalytic surface via its short diffusion pathway and ionomer-free nature. Applied as a cathode, the membrane electrode assembly (MEA) containing the vertically aligned gas diffusion electrode showed about 80% increased maximum power density than that of MEA containing a conventional electrode, which consisted of randomly dispersed carbon-supported nanoparticle catalysts and an ionomer. Moreover, the durability test revealed that the prepared ionomer-free catalyst layer was a more stable electrode than the conventional one. Also, water consumption and oxygen transport characteristics of AEMFC with the ionomer-free electrode at the cathode were intensively investigated by varying the electrode thickness and compositions.

In Chapter 4, mechanical and chemical modification technique using

oxygen plasma etching was introduced for hydrocarbon-based membrane (HC membrane). Through the plasma etching process, the oxygen functional groups were introduced on the surface as well as micro-and nano-sized structures. As a result, the adhesive force between the HC membrane and the catalyst layer was improved, resulting in the reduction of the interface resistance in the membrane-electrode assembly (MEA). Along with the interfacial resistance reduction, the structures formed on the surface reduced mass transport resistance within the catalyst layer. For this analysis, MEAs were prepared by the commercial decal-transfer method, and PEMFC performance was analyzed by performing various diagnostic techniques in various environments including catalyst layer resistance analysis and limiting current density measurements.

1.3. References

- (1) Owusu, P. A.; Asumadu–Sarkodie, S. A Review of Renewable Energy Sources, Sustainability Issues and Climate Change Mitigation. *Cogent Engineering* **2016**, *3* (1), 1167990.
- (2) Yue, M.; Lambert, H.; Pahon, E.; Roche, R.; Jemei, S.; Hissel, D. Hydrogen Energy Systems: A Critical Review of Technologies, Applications, Trends and Challenges. *Renew. Sust. Energ. Rev.* **2021**, *146*, 111180.
- (3) Dutta, S. Review on Solar Hydrogen: Its Prospects and Limitations. *Energy and Fuels* **2021**, *35* (15), 11613–11639.
- (4) Steele, B. C. H.; Heinzel, A. Materials for Fuel–Cell Technologies. *Nature* **2001**, *414* (6861), 345–352.
- (5) Costamagna, P.; Srinivasan, S. Quantum Jumps in the Pemfc Science and Technology from the 1960s to the Year 2000: Part Ii. Engineering, Technology Development and Application Aspects. *Journal of power sources* **2001**, *102* (1–2), 253–269.
- (6) Moreno, N. G.; Molina, M. C.; Gervasio, D.; Robles, J. F. P. Approaches to Polymer Electrolyte Membrane Fuel Cells (Pemfcs) and Their Cost. *Renew. Sust. Energ. Rev.* **2015**, *52*, 897–906.
- (7) Cullen, D. A.; Neyerlin, K.; Ahluwalia, R. K.; Mukundan, R.; More, K. L.; Borup, R. L.; Weber, A. Z.; Myers, D. J.; Kusoglu,

- A. New Roads and Challenges for Fuel Cells in Heavy-Duty Transportation. *Nature energy* **2021**, *6* (5), 462–474.
- (8) Dekel, D. R. Review of Cell Performance in Anion Exchange Membrane Fuel Cells. *Journal of Power Sources* **2018**, *375*, 158–169.
- (9) Ahmad, S.; Nawaz, T.; Ali, A.; Orhan, M. F.; Samreen, A.; Kannan, A. M. An Overview of Proton Exchange Membranes for Fuel Cells: Materials and Manufacturing. *International Journal of Hydrogen Energy* **2022**.
- (10) Yee, R. S. L.; Rozendal, R. A.; Zhang, K.; Ladewig, B. P. Cost Effective Cation Exchange Membranes: A Review. *Chemical Engineering Research and Design* **2012**, *90* (7), 950–959.
- (11) Wang, L.; Wan, X.; Liu, S.; Xu, L.; Shui, J. Fe–N–C Catalysts for Pemfc: Progress Towards the Commercial Application under Doe Reference. *Journal of Energy Chemistry* **2019**, *39*, 77–87.
- (12) Wang, M.; Park, J. H.; Kabir, S.; Neyerlin, K. C.; Kariuki, N. N.; Lv, H.; Stamenkovic, V. R.; Myers, D. J.; Ulsh, M.; Mauger, S. A. Impact of Catalyst Ink Dispersing Methodology on Fuel Cell Performance Using in-Situ X-Ray Scattering. *ACS Applied Energy Materials* **2019**, *2* (9), 6417–6427.

- (13) Debe, M. K. Nanostructured Thin Film Electrocatalysts for Pem Fuel Cells—a Tutorial on the Fundamental Characteristics and Practical Properties of Nstf Catalysts. *ECS Trans.* **2012**, *45* (2), 47.
- (14) Ganesan, A.; Narayanasamy, M. Ultra–Low Loading of Platinum in Proton Exchange Membrane–Based Fuel Cells: A Brief Review. *Materials for Renewable and Sustainable Energy* **2019**, *8* (4).
- (15) Stacy, J.; Regmi, Y. N.; Leonard, B.; Fan, M. The Recent Progress and Future of Oxygen Reduction Reaction Catalysis: A Review. *Renewable & Sustainable Energy Reviews* **2017**, *69*, 401–414.
- (16) Dekel, D. R. Review of Cell Performance in Anion Exchange Membrane Fuel Cells. *J. Power Sources* **2018**, *375*, 158–169.
- (17) Gottesfeld, S.; Dekel, D. R.; Page, M.; Bae, C.; Yan, Y.; Zelenay, P.; Kim, Y. S. Anion Exchange Membrane Fuel Cells: Current Status and Remaining Challenges. *J. Power Sources* **2018**, *375*, 170–184.
- (18) Cho, H.; Kim, S. M.; Kang, Y. S.; Kim, J.; Jang, S.; Kim, M.; Park, H.; Bang, J. W.; Seo, S.; Suh, K.–Y.; Sung, Y.–E.; Choi, M. Multiplex Lithography for Multilevel Multiscale Architectures and Its Application to Polymer Electrolyte Membrane Fuel Cell. *Nat. Commun.* **2015**, *6* (8484), 1–8.

- (19) Jeon, Y.; Kim, D. J.; Koh, J. K.; Ji, Y.; Kim, J. H.; Shul, Y. G. Interface-Designed Membranes with Shape-Controlled Patterns for High-Performance Polymer Electrolyte Membrane Fuel Cells. *Sci. Rep.* **2015**, *5*, 16394.
- (20) Harun, N. A. M.; Shaari, N.; Nik Zaiman, N. F. H. A Review of Alternative Polymer Electrolyte Membrane for Fuel Cell Application Based on Sulfonated Poly (Ether Ether Ketone). *International Journal of Energy Research* **2021**, *45* (14), 19671–19708.
- (21) Peighambardoust, S. J.; Rowshanzamir, S.; Amjadi, M. Review of the Proton Exchange Membranes for Fuel Cell Applications. *Int. J. Hydrog. Energy* **2010**, *35* (17), 9349–9384.
- (22) Yan, Q.; Toghiani, H.; Wu, J. Investigation of Water Transport through Membrane in a Pem Fuel Cell by Water Balance Experiments. *Journal of Power Sources* **2006**, *158* (1), 316–325.
- (23) Rui, Z.; Liu, J. Understanding of Free Radical Scavengers Used in Highly Durable Proton Exchange Membranes. *Progress in Natural Science: Materials International* **2020**, *30* (6), 732–742.
- (24) Kim, K.; Heo, P.; Hwang, W.; Baik, J. H.; Sung, Y. E.; Lee, J. C. Cross-Linked Sulfonated Poly(Arylene Ether Sulfone) Containing a Flexible and Hydrophobic Bishydroxy Perfluoropolyether Cross-Linker for High-Performance Proton

- Exchange Membrane. *ACS Appl. Mater. Interfaces* **2018**, *10* (26), 21788–21793.
- (25) Kumar, A. G.; Singh, A.; Komber, H.; Voit, B.; Tiwari, B. R.; Noori, M. T.; Ghangrekar, M. M.; Banerjee, S. Novel Sulfonated Co–Poly(Ether Imide)S Containing Trifluoromethyl, Fluorenyl and Hydroxyl Groups for Enhanced Proton Exchange Membrane Properties: Application in Microbial Fuel Cell. *ACS Appl. Mater. Interfaces* **2018**, *10* (17), 14803–14817.
- (26) Wang, L.; Deng, N.; Wang, G.; Ju, J.; Cheng, B.; Kang, W. Constructing Amino–Functionalized Flower–Like Metal–Organic Framework Nanofibers in Sulfonated Poly(Ether Sulfone) Proton Exchange Membrane for Simultaneously Enhancing Interface Compatibility and Proton Conduction. *ACS Appl. Mater. Interfaces* **2019**, *11* (43), 39979–39990.
- (27) Parnian, M. J.; Rowshanzamir, S.; Prasad, A. K.; Advani, S. G. High Durability Sulfonated Poly (Ether Ether ketone)–Ceria Nanocomposite Membranes for Proton Exchange Membrane Fuel Cell Applications. *J. Membr. Sci.* **2018**, *556*, 12–22.
- (28) Date, B.; Han, J.; Park, S.; Park, E. J.; Shin, D.; Ryu, C. Y.; Bae, C. Synthesis and Morphology Study of Sebs Triblock Copolymers Functionalized with Sulfonate and Phosphonate

- Groups for Proton Exchange Membrane Fuel Cells. *Macromolecules* **2018**, *51* (3), 1020–1030.
- (29) Higashihara, T.; Matsumoto, K.; Ueda, M. Sulfonated Aromatic Hydrocarbon Polymers as Proton Exchange Membranes for Fuel Cells. *Polymer* **2009**, *50* (23), 5341–5357.
- (30) Pu, X.; Duan, Y.; Li, J.; Ru, C.; Zhao, C. Understanding of Hydrocarbon Ionomers in Catalyst Layers for Enhancing the Performance and Durability of Proton Exchange Membrane Fuel Cells. *J. Power Sources* **2021**, *493*.
- (31) Chen, N.; Lee, Y. M. Anion Exchange Polyelectrolytes for Membranes and Ionomers. *Progress in Polymer Science* **2021**, *113*, 101345.
- (32) Maurya, S.; Noh, S.; Matanovic, I.; Park, E. J.; Villarrubia, C. N.; Martinez, U.; Han, J.; Bae, C.; Kim, Y. S. Rational Design of Polyaromatic Ionomers for Alkaline Membrane Fuel Cells with $> 1 \text{ W cm}^{-2}$ Power Density. *Energy & Environmental Science* **2018**, *11* (11), 3283–3291.
- (33) Chen, N.; Wang, H. H.; Kim, S. P.; Kim, H. M.; Lee, W. H.; Hu, C.; Bae, J. Y.; Sim, E. S.; Chung, Y.-C.; Jang, J.-H. Poly (Fluorenyl Aryl Piperidinium) Membranes and Ionomers for Anion Exchange Membrane Fuel Cells. *Nature communications* **2021**, *12* (1), 1–12.

- (34) Chen, N.; Hu, C.; Wang, H. H.; Kim, S. P.; Kim, H. M.; Lee, W. H.; Bae, J. Y.; Park, J. H.; Lee, Y. M. Poly (Alkyl-Terphenyl Piperidinium) Ionomers and Membranes with an Outstanding Alkaline-Membrane Fuel-Cell Performance of 2.58 W cm^{-2} . *Angewandte Chemie International Edition* **2021**, *60* (14), 7710–7718.
- (35) Wang, L.; Bellini, M.; Miller, H. A.; Varcoe, J. R. A High Conductivity Ultrathin Anion-Exchange Membrane with 500+ H Alkali Stability for Use in Alkaline Membrane Fuel Cells That Can Achieve 2 W cm^{-2} at 80 C. *Journal of Materials Chemistry A* **2018**, *6* (31), 15404–15412.
- (36) Mandal, M.; Huang, G.; Hassan, N. U.; Mustain, W. E.; Kohl, P. A. Poly (Norbornene) Anion Conductive Membranes: Homopolymer, Block Copolymer and Random Copolymer Properties and Performance. *J. Mater. Chem. A* **2020**, *8* (34), 17568–17578.
- (37) Ul Hassan, N.; Mandal, M.; Huang, G.; Firouzjaie, H. A.; Kohl, P. A.; Mustain, W. E. Achieving High-Performance and 2000 H Stability in Anion Exchange Membrane Fuel Cells by Manipulating Ionomer Properties and Electrode Optimization. *Advanced Energy Materials* **2020**, *10* (40), 2001986.

- (38) Wang, J.; Zhao, Y.; Setzler, B. P.; Rojas–Carbonell, S.; Ben Yehuda, C.; Amel, A.; Page, M.; Wang, L.; Hu, K.; Shi, L. Poly (Aryl Piperidinium) Membranes and Ionomers for Hydroxide Exchange Membrane Fuel Cells. *Nature Energy* **2019**, *4* (5), 392–398.
- (39) Adabi, H.; Shakouri, A.; Ul Hassan, N.; Varcoe, J. R.; Zulevi, B.; Serov, A.; Regalbuto, J. R.; Mustain, W. E. High–Performing Commercial Fe–N–C Cathode Electrocatalyst for Anion–Exchange Membrane Fuel Cells. *Nature energy* **2021**, *6* (8), 834–843.
- (40) Wang, Y.; Pang, Y.; Xu, H.; Martinez, A.; Chen, K. S. Pem Fuel Cell and Electrolysis Cell Technologies and Hydrogen Infrastructure Development: A Review. *Energy & Environmental Science*, **2022**.
- (41) Husar, A.; Strahl, S.; Riera, J. Experimental Characterization Methodology for the Identification of Voltage Losses of Pemfc: Applied to an Open Cathode Stack. *Int. J. Hydrog. Energy* **2012**, *37* (8), 7309–7315.
- (42) Neyerlin, K.; Gu, W.; Jorne, J.; Gasteiger, H. A. Determination of Catalyst Unique Parameters for the Oxygen Reduction Reaction in a Pemfc. *J. Electrochem. Soc.* **2006**, *153* (10), A1955.

- (43) Gasteiger, H. A.; Kocha, S. S.; Sompalli, B.; Wagner, F. Activity Benchmarks and Requirements for Pt, Pt–Alloy, and Non–Pt Oxygen Reduction Catalysts for Pemfcs. *Appl. Catal. B Environ.* **2005**, *56* (1–2), 9–35.
- (44) Farrukh, A.; Ashraf, F.; Kaltbeitzel, A.; Ling, X.; Wagner, M.; Duran, H.; Ghaffar, A.; ur Rehman, H.; Parekh, S. H.; Domke, K. F. Polymer Brush Functionalized Sio₂ Nanoparticle Based Nafion Nanocomposites: A Novel Avenue to Low–Humidity Proton Conducting Membranes. *Polymer Chemistry* **2015**, *6* (31), 5782–5789.
- (45) Mennola, T.; Mikkola, M.; Noponen, M.; Hottinen, T.; Lund, P. Measurement of Ohmic Voltage Losses in Individual Cells of a Pemfc Stack. *J. Power Sources* **2002**, *112* (1), 261–272.
- (46) Haji, S. Analytical Modeling of Pem Fuel Cell I–V Curve. *Renewable Energy* **2011**, *36* (2), 451–458.
- (47) Ijaodola, O. S.; El–Hassan, Z.; Ogungbemi, E.; Khatib, F. N.; Wilberforce, T.; Thompson, J.; Olabi, A. G. Energy Efficiency Improvements by Investigating the Water Flooding Management on Proton Exchange Membrane Fuel Cell (Pemfc). *Energy* **2019**, *179*, 246–267.
- (48) Kaneko, T.; Yoshimoto, Y.; Hori, T.; Takagi, S.; Ooyama, J.; Terao, T.; Kinefuchi, I. Relation between Oxygen Gas

- Diffusivity and Porous Characteristics under Capillary Condensation of Water in Cathode Catalyst Layers of Polymer Electrolyte Membrane Fuel Cells. *International Journal of Heat Mass and Transfer* **2020**, *150*, 119277.
- (49) Kongkanand, A.; Mathias, M. F. The Priority and Challenge of High-Power Performance of Low-Platinum Proton-Exchange Membrane Fuel Cells. *The journal of physical chemistry letters* **2016**, *7* (7), 1127–1137.
- (50) Wu, J.; Yuan, X. Z.; Martin, J. J.; Wang, H.; Zhang, J.; Shen, J.; Wu, S.; Merida, W. A Review of Pem Fuel Cell Durability: Degradation Mechanisms and Mitigation Strategies. *J. Power Sources* **2008**, *184* (1), 104–119.
- (51) Yuan, X.-Z.; Li, H.; Zhang, S.; Martin, J.; Wang, H. A Review of Polymer Electrolyte Membrane Fuel Cell Durability Test Protocols. *J. Power Sources* **2011**, *196* (22), 9107–9116.
- (52) Nguyen, H. L.; Han, J.; Nguyen, X. L.; Yu, S.; Goo, Y.-M.; Le, D. D. Review of the Durability of Polymer Electrolyte Membrane Fuel Cell in Long-Term Operation: Main Influencing Parameters and Testing Protocols. *Energies* **2021**, *14* (13).
- (53) Matanovic, I.; Chung, H. T.; Kim, Y. S. Benzene Adsorption: A Significant Inhibitor for the Hydrogen Oxidation Reaction in

- Alkaline Conditions. *The journal of physical chemistry letters* **2017**, *8* (19), 4918–4924.
- (54) Mustain, W. E.; Chatenet, M.; Page, M.; Kim, Y. S. Durability Challenges of Anion Exchange Membrane Fuel Cells. *Energy & Environmental Science* **2020**, *13* (9), 2805–2838.
- (55) Stanic, V. Mechanism of Pinhole Formation in Membrane Electrode Assemblies for Pem Fuel Cells. *ECS Proceedings Volumes* **2004**, *2004-21* (1), 391–401.
- (56) Kusoglu, A.; Weber, A. Z. A Mechanistic Model for Pinhole Growth in Fuel-Cell Membranes During Cyclic Loads. *J. Electrochem. Soc.* **2014**, *161* (8), E3311–E3322.
- (57) Coms, F. D. The Chemistry of Fuel Cell Membrane Chemical Degradation. *ECS Trans.* **2008**, *16* (2), 235–255.
- (58) Curtin, D. E.; Lousenberg, R. D.; Henry, T. J.; Tangeman, P. C.; Tisack, M. E. Advanced Materials for Improved Pemfc Performance and Life. *J. Power Sources* **2004**, *131* (1–2), 41–48.
- (59) Zatoń, M.; Rozière, J.; Jones, D. J. Current Understanding of Chemical Degradation Mechanisms of Perfluorosulfonic Acid Membranes and Their Mitigation Strategies: A Review. *Sustain. Energ. Fuels* **2017**, *1* (3), 409–438.

- (60) Rodgers, M. P.; Bonville, L. J.; Kunz, H. R.; Slattery, D. K.; Fenton, J. M. Fuel Cell Perfluorinated Sulfonic Acid Membrane Degradation Correlating Accelerated Stress Testing and Lifetime. *Chem. Rev.* **2012**, *112* (11), 6075–6103.

Chapter 2. Fabrication of Multi-Functional Dendritic Structure for High-durable and High-Efficient PEMFCs

Note: This chapter is reproduced from the work I co-authored with Je Hyeon Yeon (co-first author), published in *ACS Applied Materials & Interfaces*, **2021**, 13, 1, 806–815.

2.1. Introduction

Proton-exchange membrane fuel cells (PEMFCs) have been extensively studied as promising sources of sustainable energy for automotive, stationary, and portable applications owing to their eco-friendly operation (zero emissions), low operating temperatures, and high energy efficiency¹⁻². The successful commercial adoption of PEMFCs without government incentives, however, is hampered by the high cost of materials and inadequate durability and performance³⁻⁴. To reduce costs, researchers have attempted to develop non-precious metal catalysts and reduce catalyst loading⁵⁻⁹. However, non-precious metal catalysts do not yet achieve the high catalytic activity of widely used platinum catalysts, while the drawbacks of a reduction in catalyst loading include increased kinetics and mass transport overpotential when incorporated into a membrane electrode assembly (MEA) for a PEMFC single cell^{1,10}. Recently, tailoring the membrane-electrode interface through modification of the MEA fabrication process¹¹ and introduction of micro-and-nano structures onto the membrane surface¹² has enhanced both catalytic utilization and mass transport while using the same materials and maintaining catalyst loading. This resulted from the enlarged interfacial area between the membrane and the catalyst layer as well as the modified electrode morphology.

The durability of PEMFCs is an increasingly pressing priority, especially as fuel-cell vehicles become a feature of our daily lives. Although manufacturers of PEMFCs are required to warrant long-term operation ($> 5,000$ h) with minimal performance loss, current PEMFC technologies still lag far behind the practical demands¹³⁻¹⁴. Degradation of the membrane, especially the commonly used perfluorosulfonic acid (PFSA) membrane (e.g. Nafion®), is one of the primary causes of low PEMFC durability and it can be induced by mechanical stress, during repeated drying and swelling operating conditions¹⁵⁻¹⁶, and by chemical decomposition, due to oxidative hydroxyl (HO^*) and hydroperoxyl (HOO^*) radical attack¹⁷⁻¹⁸. These free radicals, generated from the reaction between released cations (e.g. Fe^{2+}) and hydrogen peroxide (H_2O_2) during fuel cell operation, cause the decomposition of the main and side chains of the PFSA membranes resulting in membrane thinning and pinhole formation^{3,14,19}. To mitigate the radical attack and improve the chemical durability of the membrane, various approaches that incorporate inorganic radical scavengers, such as cerium (Ce) and manganese (Mn), into the membrane have been reported²⁰⁻²⁵. Although the composite membrane produced by mixing the PFSA ionomer and a radical scavenger (e.g. CeO_2) showed excellent chemical durability, the trade-off was lower proton conductivity caused by the

agglomeration of nano-sized CeO_2 inside the membrane and substitution of a proton with a $\text{Ce}^{3+/4+}$ ion at the sulfonic-acid group^{23,26}.

In this chapter, multifunctional dendritic Nafion[®]/ CeO_2 structures were introduced to simultaneously enhance the performance and durability of PEMFCs. To fabricate the dendritic structures, Nafion[®] ionomer resin and CeO_2 nanoparticles were applied to the membrane surface using electrospray deposition to adjust the electrostatic force and utilize the van der Waals force of the fine droplets. The three-dimensional (3-D) dendritic structures increased the membrane surface area, enlarging the interfacial contact area between the membrane and the catalyst layer where electrochemical reactions occur most effectively. The bumpy catalyst layer, resulting from the uniform deposition of the Pt/C catalyst onto the dendritic Nafion[®]/ CeO_2 structures, induced microscale voids between the catalyst layer and the gas diffusion layer (GDL). This enabled the easy removal of water generated by the oxygen reduction reactions (ORR). These structural properties enhanced catalyst utilization and mass transport, which are directly related to the performance of PEMFCs. Especially, under low humidity conditions, the hygroscopic effect of CeO_2 nanoparticles enhanced water retention at the cathode. Additionally, the incorporation of CeO_2 , not within the membrane but

at the outer surface of the membrane, where membrane chemical degradation is initiated by the radicals formed during PEMFC operation, effectively scavenged the free radicals and improved the PEMFC durability while minimizing the decrease in ionic conductivity of the membrane. These multifunctional effects of the dendritic Nafion[®]/CeO₂ structures on PEMFC performance were investigated using various techniques including an in-situ open-circuit voltage (OCV) hold test, electrochemical measurement, an ex-situ Fenton's test, and material characterization.

2.2. Experimental methods

2.2.1. Fabrication of the dendritic Nafion[®]/CeO₂ structures

First, CeO₂ nanoparticles (Sigma–Aldrich, United States, ~ 25 nm size) were mixed with a Nafion[®] ionomer solution (Sigma–Aldrich, United States, 5 wt.% in a mixture of lower aliphatic alcohols and water) in a weight ratio of 1:19. Using electrospray deposition (Nano NC Inc., Korea), the prepared solution was applied to a Nafion[®] 211 membrane (Dupont, United States, ~ 25 μ m thick) fixed with a metal mask (square opening area ~ 5 cm²) on a hot plate at a temperature of approximately 100 °C. The electrospray system consisted of a flow rate control pump, a microsyringe needle, and a high–voltage direct–current source. During the deposition, the flow rate was fixed at 0.3 mL h^{–1} and a high–voltage, of approximately 9 kV, was applied to generate a uniform cone–jet mode. After deposition, sintering was conducted at the glass transition temperature of Nafion[®] (~140 °C) under an air atmosphere, to enhance interface adhesion between the membrane and the dendritic structures.

2.2.2. MEA and single–cell preparation

Catalyst slurries were prepared by mixing a carbon–supported platinum catalyst (Johnson Matthey Co., United Kingdom, Pt: 40 wt.%), deionized water, 5 wt.% Nafion[®] ionomer solution, and 2–

propanol (Sigma–Aldrich, United States). The catalyst slurries were sprayed onto both the anode and cathode–side of the pure and modified Nafion® 211 membranes with a Pt loading of 0.2 mg cm^{-2} on each side. Pt loading was carefully confirmed before MEA fabrication from the weight difference of a PET (polyethylene terephthalate) film before and after the application of the Pt/C catalyst ink, because Nafion® membrane can easily absorb moisture in the atmospheric environment and errors may occur during the weighing process. The geometric active area of the MEA was 5 cm^2 . To evaluate the single–cell performance and durability, the catalyst–coated membrane (CCM) was placed at the center of a single cell with a bipolar plate with a serpentine type flow channel (width: $\sim 1 \text{ mm}$) and two GDLs (JNTG, Korea, JNT 30–A3, $\sim 300 \text{ }\mu\text{m}$ thick). Teflon gaskets (CNL Energy, Korea, $\sim 250 \text{ }\mu\text{m}$ thick) were inserted at both the anode and cathode sides to limit gas permeability and improve contact between the GDL and the MEA by compressing the GDL. Finally, the single cells were firmly assembled by fastening eight bolts with a torque of 108 N m .

2.2.3. Characterization

The assembled single cell was connected to a PEMFC test station (CNL Energy, Korea) and the cell temperature was maintained at

70 °C. In relative humidity (RH) 100%, 60 %, and 30% operation conditions, the water temperature was set to 70 °C, 58.8 °C, and 44.5 °C, respectively. To measure the polarization curves, the current sweep method with a sweep rate of 10 mA cm⁻² s⁻¹ was utilized while supplying humidified H₂ (150 mL min⁻¹) and air (350 mL min⁻¹) to the anode and cathode, respectively. The electrochemical impedance spectroscopy (EIS) spectra were obtained using an impedance analyzer (BioLogic, France, HCP-803) at 0.6 V with an amplitude of 10 mV and frequency ranging from 0.1 Hz to 70 kHz. The other experimental conditions, including temperature and flow rates, were consistent with the polarization tests. To quantitatively compare catalyst utilization, cyclic voltammetry (CV) was conducted with a scan rate of 50 mV s⁻¹ in the sweep range of 0.05 V to 1.2 V by supplying fully humidified H₂ (50 mL min⁻¹) and N₂ (200 mL min⁻¹) gas to the anode and cathode, respectively. To evaluate the durability of the pure and modified membranes, OCV hold and Fenton' s tests were conducted. For the OCV hold test, the cell temperature was maintained at 90 °C by supplying partially humidified H₂ (300 mL min⁻¹) and air (300 mL min⁻¹) with a relative humidity of 30 % and additional backpressure of 0.8 bar, which is a harsher condition than the department of energy (DOE) protocol²⁷ To measure the hydrogen crossover of the pristine

and the modified membrane, linear sweep voltammetry (LSV) was conducted with a scan rate of 2 mV s^{-1} in the sweep range of 0.05 V to 0.6 V by supplying fully humidified H_2 (200 mL min^{-1}) and N_2 (200 mL min^{-1}) gas to the anode and cathode, respectively. The crossover current densities were measured at 0.3 V potential point from LSV spectra for all samples. In the case of Fenton's test, the pure Nafion® 211 membrane and the Nafion® 211 membranes with the dendritic Nafion®/CeO₂ structures were immersed in a 200 ml Fenton solution (3 wt.% H₂O₂, 3 ppm Fe²⁺) at 80 ° C. The Fenton solution was replaced every 24 h and the concentration of the fluoride ion (F⁻) was measured using ion chromatography (Thermo Scientific, United States, Orion Star A214). The Ce³⁺/Ce⁴⁺ ratio of the CeO₂ nanoparticles was obtained using X-ray photoelectron spectroscopy (XPS, AXIS SUPRA, Kratos, UK)

Transmission electron microscopy (TEM) images of the CeO₂ particles were obtained (Thermo Fisher Scientific, USA, FEI TITAN 80–300). Field emission–scanning electron microscopy (FE–SEM) (Carl Zeiss, Germany) and both the secondary electron–mode (SE mode) and the backscattered electron–mode (BSE mode) were used to analyze the morphology and the phase distribution. Focused ion beam scanning electron microscopy (FIB–SEM) (Carl Zeiss, Germany) was used to obtain cross–section images of the prepared

MEA. Corresponding energy-dispersive X-ray spectroscopy (EDS) was conducted to analyze the CeO_2 distribution and content of the modified MEA with the dendritic Nafion[®]/ CeO_2 structures.

2.3. Results and discussion

2.3.1. Dendritic structures via ESD process and the structure characterization

Figure 2.1 a–c illustrates the electrospray deposition system and fabrication process of the dendritic Nafion[®]/CeO₂ structures. The system essentially consists of a capillary needle with high voltage, a substrate (SUS plate) with ground connection, and a mask with a square opening area ($\sim 5 \text{ cm}^2$) over the Nafion[®] 211 membrane (**Figure 2.1 a**). The operation proceeded as follows: (a) a syringe pump drove the Nafion[®]/CeO₂ ($\sim 25 \text{ nm}$ size, TEM images are shown in **Figure 2.2**) liquid solution through a capillary tube into the needle at a desired constant flow rate, (b) at the tip of the needle, a high electric potential was applied to the liquid to create a cloud of tiny charged droplets with a consistent size distribution due to the electric repulsion suppressing agglomeration of the droplets. To ensure a steady generation of monodisperse droplets, the electrospray was applied in the cone–jet mode with a Taylor cone²⁸ at the needle exit, (c) the charged droplets evaporated while approaching the membrane under electric force. Near the membrane surface, the approaching charged nanoparticles experienced random velocity due to the nano–scale droplets being influenced by Brownian motion and van der

Waals attraction forces from already deposited particles (**Figure 2.1 b**). As a result, the Nafion[®]/CeO₂ nanoparticles self-assembled to form highly branched 3-D porous dendritic structures^{29–30} (**Figure 2.1 c**). To confirm the effectiveness of the electrospray deposition method, the conventional air-spray deposition was conducted using the same Nafion[®]/CeO₂ solution (**Figure 2.3**). Unlike the dendritic structures produced under electrospray deposition, the air-spray deposited Nafion[®]/CeO₂ formed a thin flat film due to the absence of an electric field to induce the formation of nano-scale droplets of charged particles. The surface images (**Figure 2.1 d–e**) show the morphology of the fabricated dendritic structures with 1.0 h deposition time, possessing a high surface area and porosity due to extensive branching. To understand the effect of deposition time on structure formation, we repeated the electrospray deposition with varying deposition times from 0.5 h to 2 h, the other experimental conditions were unchanged. The inter-structure spacing and the height of the fabricated structures for deposition time are graphically represented in **Figure 2.1 f** and the corresponding SEM images are shown in **Figure 2.4**. Due to the self-assembling nature of the structures, their structural parameters vary, however, it is clear that the size and density of the structures increase as the deposition time increases. Additionally, by performing the mechanical test for the

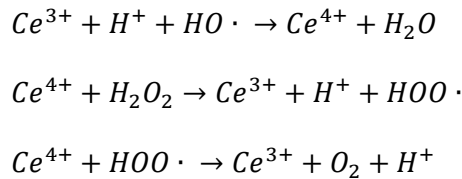
pristine and the modified membrane using the universal testing machine (UTM), we confirmed that introducing the structure with the electrospray deposition method did not significantly affect the mechanical properties of the membrane, but rather, the heat treatment process increased the modulus of the membrane (**Figure 2.5**).

Figure 2.6 a and **Figure 2.7 a–c** show the cross-sectional SEM image of the Nafion[®]/CeO₂ structures and its corresponding EDS mapping images of sulfur (S) and cerium (Ce), respectively. Since the membrane and the structures contain the sulfonic–acid group of Nafion[®], S elements were detected within the entire region³¹. In the case of Ce, it is only well–distributed within the structures. To confirm that CeO₂ nanoparticles were evenly distributed over the structures, BSE–mode SEM images of the Nafion[®]/CeO₂ structures were obtained. As shown in **Figure 2.6 b–c**, the CeO₂ nanoparticles, shown as a white dot, covered the whole surfaces of the Nafion[®] structures without large agglomeration. This suggests that the CeO₂ in the structures can effectively alleviate radical attack at the outer surface of the membrane and avoid the decrease in the conductivity experienced by mixed CeO₂/Nafion[®] composite membranes due to CeO₂ nanoparticle agglomeration during fabrication^{21,32}. After confirming the presence of Nafion[®]/CeO₂ structures on the membrane,

a catalyst layer was deposited onto the modified membrane for application in a PEMFC. **Figure 2.6 d–e** shows surface images of the MEA with the modified membrane and it is evident that the catalyst layer was uniformly deposited on the entire surface of the dendritic structures. The modified MEA has unique bumpy structures compared to the flat reference MEA surface (**Figure 2.8**). The magnified cross-sectional FIB image of the extruded bumpy electrode (**Figure 2.6 f**) further confirms that the catalyst layer completely coated the entire surface of the Nafion®/CeO₂ structures, enabling effective catalyst utilization due to the enlarged interfacial contact area between the membrane and the catalyst layer, where electrochemical reactions occur most effectively.

Additional multifunctional effects of these structures (i.e., efficient removal of generated water and radicals) are depicted in **Figure 2.9**. Generally, water is generated during ORRs in PEMFCs. If the water accumulates inside the porous catalyst layer, it hinders the mass transport of the reactant. Therefore, effective water management is imperative for achieving high-performance PEMFCs. The bumpy surface of the catalyst layer, resulting from the dendritic structures on the membrane, formed unique microscale voids between the catalyst layer and the GDL. The generated water inside the mesoporous catalyst electrode moves to the surface, pools in the

valleys of the bumpy structures, and then coalesces with the neighboring water droplets before finally ejecting into the GDL. Similar water behavior and water drainage effects of modified void-containing electrodes used in PEMFCs have been reported ^{33–35}. To explain the enhanced chemical durability, the radical scavenging effect of CeO₂ nanoparticles inside the Nafion®/CeO₂ structures is shown in the magnified schematic of **Figure 2.9**. The CeO₂ nanoparticle is a well-known free-radical scavenger, due to its ability to switch between the 3⁺ and 4⁺ valence states. The OH· radical, which causes chemical degradation of the membrane, can be removed through the following reaction ^{22,36}.



Generally, it is hypothesized that an increase in surface Ce³⁺ concentration will enhance surface oxygen vacancy concentration in the lattice, which in turn should enhance the free radical scavenging ability of ceria-based materials.²⁵ Therefore, analysis of the Ce³⁺/Ce⁴⁺ ratio is important in predicting the radical scavenging effect of CeO₂. To calculate the Ce³⁺/Ce⁴⁺ ratio, the deconvolution process for the XPS spectrum of the CeO₂ was conducted by using six peaks for Ce⁴⁺ spectrum and two peaks for Ce³⁺ spectrum,

respectively (**Figure 2.10**).³⁷ The $\text{Ce}^{3+}/\text{Ce}^{4+}$ ratio was calculated to be about 27% and this value is comparable with the previous papers using commercial CeO_2 particles similar to the particles used in this study.³⁸⁻³⁹

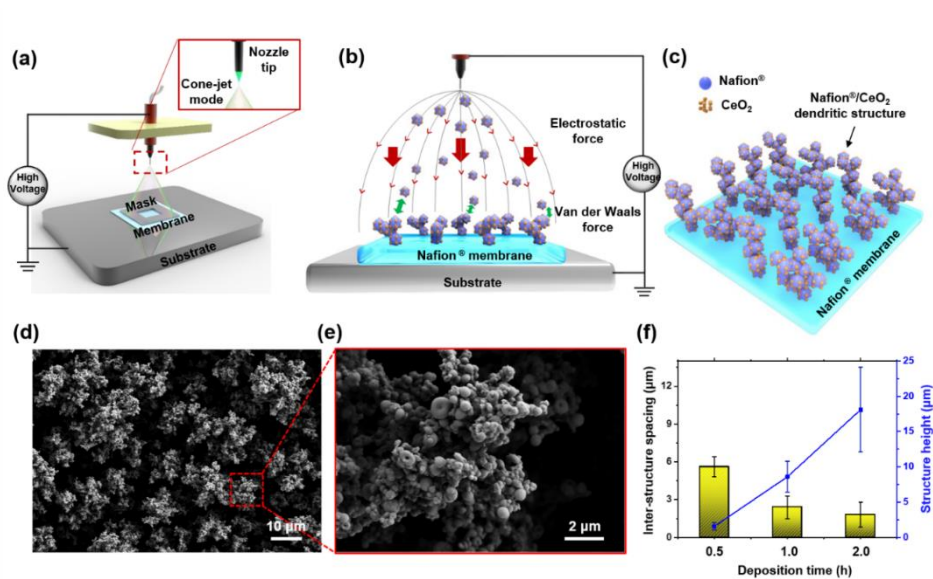


Figure 2.1. (a) Schematic of electrospray deposition (ESD) experimental set-up. The inset image illustrates the cone-jet mode at the nozzle tip. (b) Schematic diagram for ESD process, and (c) the 3-D image of the completed dendritic Nafion®/CeO₂ structure. The surface morphological SEM images of the fabricated structure with 1.0 h deposition time with (d) low-magnification and (e) high-magnification. (f) The structural characteristics of inter-structure spacing and the height of the fabricated structures with regard to deposition time

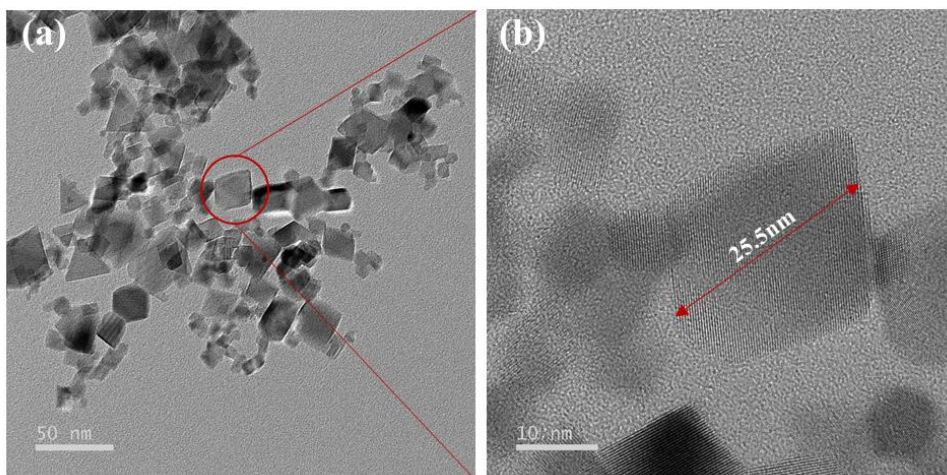


Figure 2.2. TEM images of CeO_2 nanoparticles under (a) low magnification and (b) high magnification.

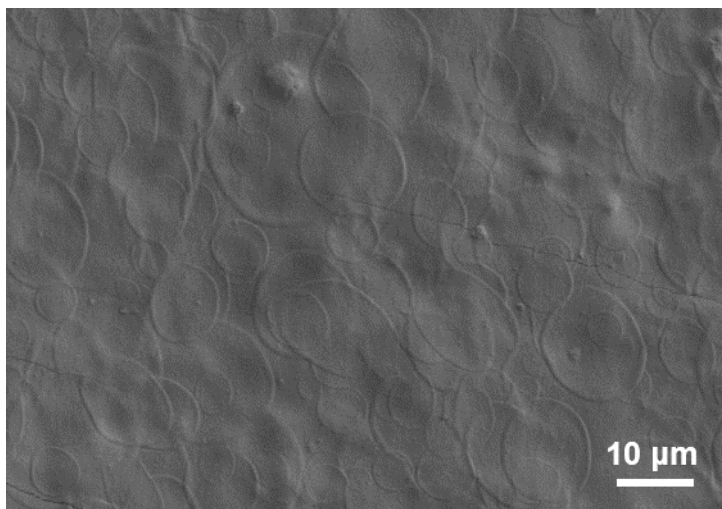


Figure 2.3. A surface image of the Nafion®/CeO₂ structure on the Nafion® 211 membrane by using a conventional air-spray method.

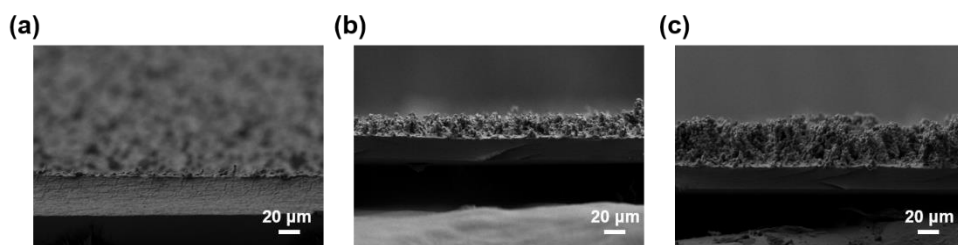


Figure 2.4. Cross-sectional SEM images of the Nafion[®]/CeO₂ structures after deposition times of (a) 0.5 h, (b) 1.0 h and, (c) and 2.0 h.

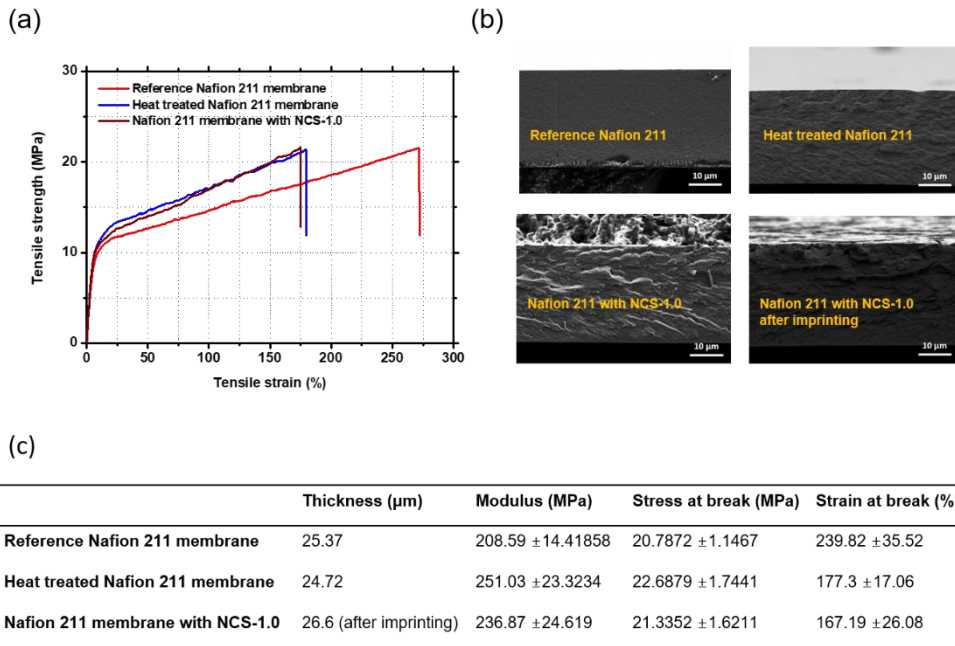


Figure 2.5. Universal testing machine (UTM) based mechanical stability test results of the reference Nafion[®] 211 membrane with and without heat treatment and the modified Nafion[®] 211 membrane with NCS–1.0 (a) stress–strain curves, (b) cross–sectional SEM images and (c) summary of the UTM based mechanical test.

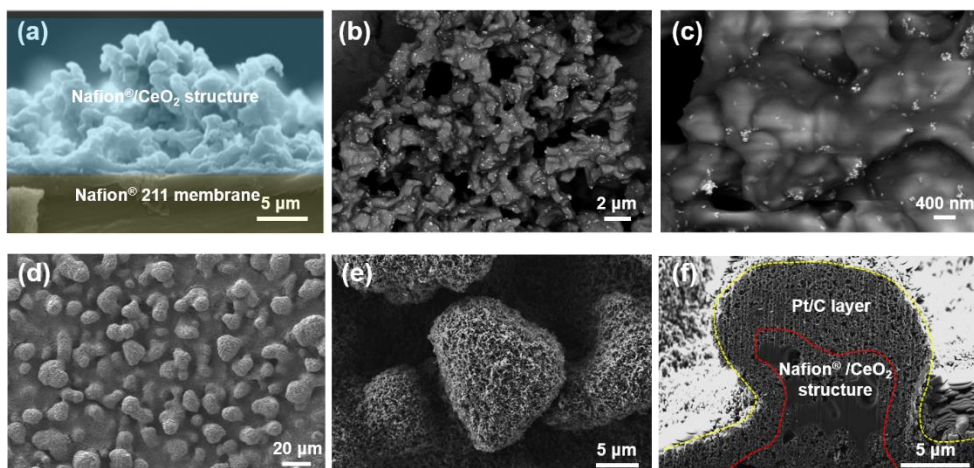


Figure 2.6. (a) The cross-sectional SEM image of Nafion®/CeO₂ structures and BSE mode SEM images of Nafion®/CeO₂ structures with (b) low-magnification and (c) high magnification. The surface images of the MEA after catalyst layer deposition onto the modified membrane with (d) low-magnification, (e) high-magnification and (f) FIB-assisted cross-sectional image.

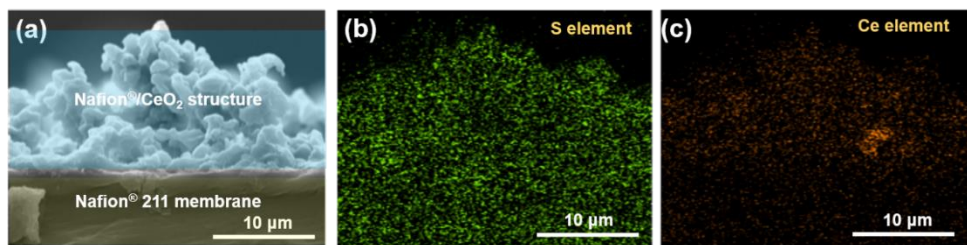


Figure 2.7. (a) The cross-sectional SEM image of Nafion®/CeO₂ structures and its correspondent EDS mapping images of (b) sulfur and (c) cerium, respectively.

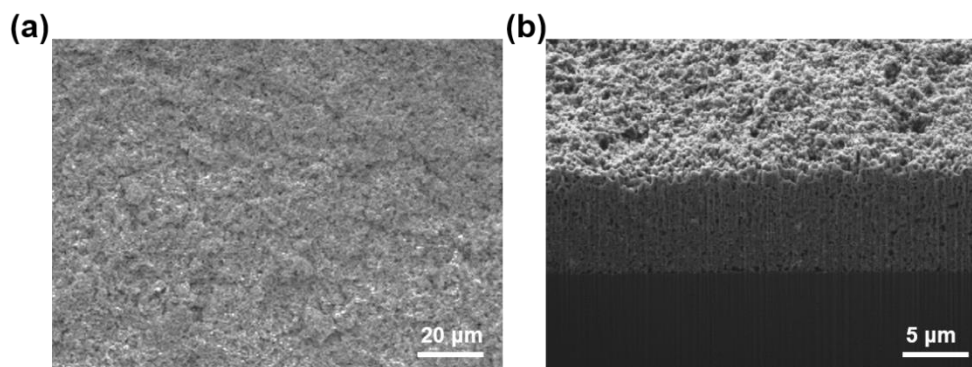


Figure 2.8. (a) The surface and (b) cross-sectional SEM images of the MEA with flat, pure Nafion[®] 211 membrane.

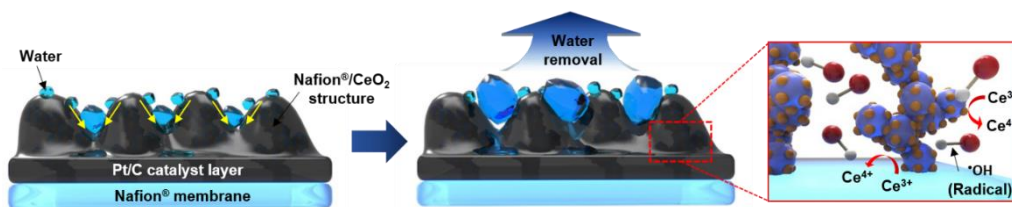


Figure 2.9. Schematic illustrations for multifunctional effects of the modified MEA with Nafion[®]/CeO₂ structure for efficient removal of generated water and radicals.

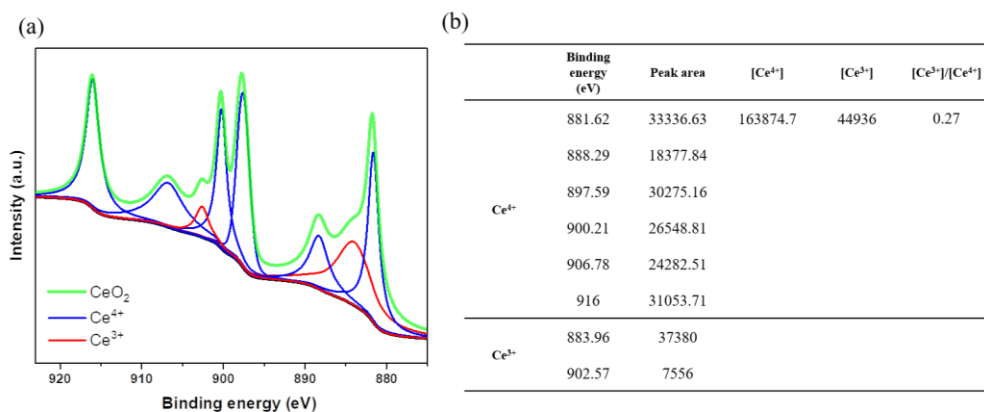


Figure 2.10. XPS spectra of ceria particles (< 25 nm, Sigma Aldrich) in this study; (a) high-resolution XPS spectra of Ce 3d and (b) XPS analysis of Ce³⁺ and Ce⁴⁺ ion concentration.

2.3.2. Analysis of single-cell performance

Next, to investigate the multifunctional effects of the Nafion[®]/CeO₂ structures on the performance and durability of a PEMFC, we fabricated single cells including a reference MEA with Nafion[®] 211 membrane and modified MEAs with Nafion[®] 211 membranes with Nafion[®]/CeO₂ structures fabricated during varying deposition times (0.5 h, 1.0 h, and 2.0 h). The structured side was used as the cathode because performance degradation primarily occurs at the cathode due to slow ORRs and water flooding during operation. The different fabricated Nafion/CeO₂ structures were denoted by NCS-*x*, where *x* is the deposition time. To determine the optimal deposition conditions, where the combined effects of enhanced catalyst utilization and mass transport exceed the ohmic resistance increase of the membrane, electrochemical single-cell tests were conducted on the reference and modified MEAs. **Figure 2.11 a** shows the polarization curves at 70 ° C with fully humidified H₂ (150 mL min⁻¹) and air (350 mL min⁻¹) supplied at the anode and cathode, respectively. Compared to the reference MEA, the maximum power density of the MEA with NCS-1.0 (~ 685 mW cm⁻²) was ~ 9.25 % higher; however, the MEAs with NCS-0.5 and NCS-2.0 showed reduced performance of ~ 5.58 % and ~ 7.50 %, respectively. This indicates that an optimum degree of Nafion[®]/CeO₂ structures deposition exists that maximizes PEMFC

performance. To better understand the effects of the Nafion[®]/CeO₂ structures on PEMFC operation, EIS measurements were conducted at 0.6 V. **Figure 2.11 b** shows the EIS spectra (marked points) of tested MEAs together with fitted curves (solid lines) based on the corresponding equivalent circuit (**Figure 2.12**); the EIS fitted values and the key parameters of the tested MEAs are summarized in **Table 2.1**. First, we confirmed the ohmic resistance of the MEAs. The deposition of Nafion[®]/CeO₂ structures onto the membrane is inevitably accompanied by increased resistance due to the non-proton-conducting nature of CeO₂ nanoparticles. As expected, as the deposition time increased (and the size of the structures and the amount of CeO₂ increased), the ohmic resistance of the MEA with NCS-0.5, with NCS-1.0, and with NCS-2.0 was higher at 0.0601 Ω cm², 0.0612 Ω cm², and 0.0618 Ω cm², respectively, than that of the reference MEA (0.0595 Ω cm²). However, the difference in the charge transfer resistance showed a different aspect. The charge transfer resistance (R_{LF-HF}) is calculated using the diameter of the semicircle at the middle- and low-frequency ranges, which are caused mainly by electrochemical resistance from the cathode reactions²⁰. Due to the influence of the catalyst utilization and mass transport, the MEA with NCS-1.0 shows the lowest charge transfer resistance of 0.193 Ω cm², ~ 14.3% less than that of the reference

MEA ($0.224 \ \Omega \text{ cm}^2$), which is significantly greater than the concomitant increase in ohmic resistance of $\sim 2.86\%$. This indicates that the bumpy surface of the catalyst layer and high incidence of microscale voids effectively removes the generated water which otherwise hinders the mass transport of the reactant as explained. However, in the case of the MEA with NCS-0.5, the mass transport effect is marginal compared to that of the reference MEA. This is because the small structures are easily filled by the catalyst layer (**Figure 2.1 d and 2.4**). Interestingly, although the MEA with NCS-2.0 has a lot of deep microscale voids (**Figure 2.4**), it shows increased charge transport resistance. This suggests that an optimum thickness of the structures exists to maximize mass transport. The height of the NCS-2.0 (average thickness of $17 \ \mu\text{m}$) is more than double the height of NCS-1.0 (average thickness of $8 \ \mu\text{m}$) which negatively affects the mass transport between the increased electrode-thickness and reactant pathway.

Figure 2.11 c-d shows the polarization curves and corresponding EIS spectra of the reference MEA and MEA with NCS-1.0 under low humidity conditions (RH 60% and RH 30%). For both RH 60% and 30% conditions, the MEA with NCS-1.0 showed significantly higher maximum power density than that of the reference MEA. In the condition of RH 60%, the MEA with NCS-1.0 showed $\sim 15.33\%$

increased maximum power density of $\sim 579 \text{ mW cm}^{-2}$ compared to the reference MEA of 502 mW cm^{-2} . As shown in **Figure 2.11 d**, the MEA with NCS-1.0 had lower charge transfer resistance of $0.2366 \Omega \text{ cm}^2$ compared to the reference MEA ($0.3015 \Omega \text{ cm}^2$). Interestingly, unlike the RH 100% condition, the MEA with NCS-1.0 showed lower ohmic resistance of $0.0721 \Omega \text{ cm}^2$ than that of the reference MEA ($0.0818 \Omega \text{ cm}^2$). In the case of the RH 30% condition, the MEA with NCS-1.0 had even $\sim 39.26\%$ higher maximum power density and lower ohmic and charge transfer resistance (**Table 2.1**). These results indicate that the water retention effect of the membrane was improved due to the hygroscopic property of CeO_2 nanoparticles, as well as catalyst utilization and the mass transport were enhanced by the structural characteristics of Nafion[®]/ CeO_2 structures.⁴⁰⁻⁴¹ As the RH decreases, the difference in the performance between the modified MEA and the reference MEA becomes even larger because of the increase in the water retention and mass transport effects. These structural and hygroscopic effects were also convinced by using hygroscopic TiO_2 nanoparticles ($\sim 21 \text{ nm}$) (e.g. MEA with NTS-1.0) instead of CeO_2 nanoparticles (**Figure 2.13**).

After confirming the effect of the NCS-1.0 structures on its mass transportability, we further investigated its effect on the catalytic

utilization in PEMFCs. **Figure 2.14** shows the CV curves of the reference MEA and the MEA with NCS-1.0 as a cathode in single cells. From the integration of the hydrogen charge density under the potential desorption peak, the electrochemically active surface areas (ECSAs) of each MEA were calculated by following equation ⁴²,

$$\text{ECSA } (m_{Pt}^2 g_{Pt}^{-1}) = \frac{q_{Pt}}{\Gamma L}$$

In the above equation, q_{Pt} is the charge density of hydrogen desorption obtained from the CV curves, Γ is the charge required to reduce a monolayer of protons on Pt surface, which is $210 \mu\text{C cm}^{-2}$, and L is the Pt loading at the cathodes, i.e., 0.2 mg cm^{-2} in this study. The ECSA for the MEA with NCS-1.0 was $51.1 \text{ m}^2 \text{ g}^{-1}$, which is 33.7% larger than that of the reference MEA ($38.2 \text{ m}^2 \text{ g}^{-1}$), indicating that the high surface area of the dendritic Nafion[®]/CeO₂ structures, achieved through electrospray deposition, enlarged the interfacial contact area between the membrane and the catalyst layer. This means that the triple-phase boundary, which acts as the active site for gaseous O₂ molecules, electrons, and protons, was much greater than that of the reference MEA, with its flat membrane, which improved catalyst utilization and PEMFC performance ^{12,34,43}.

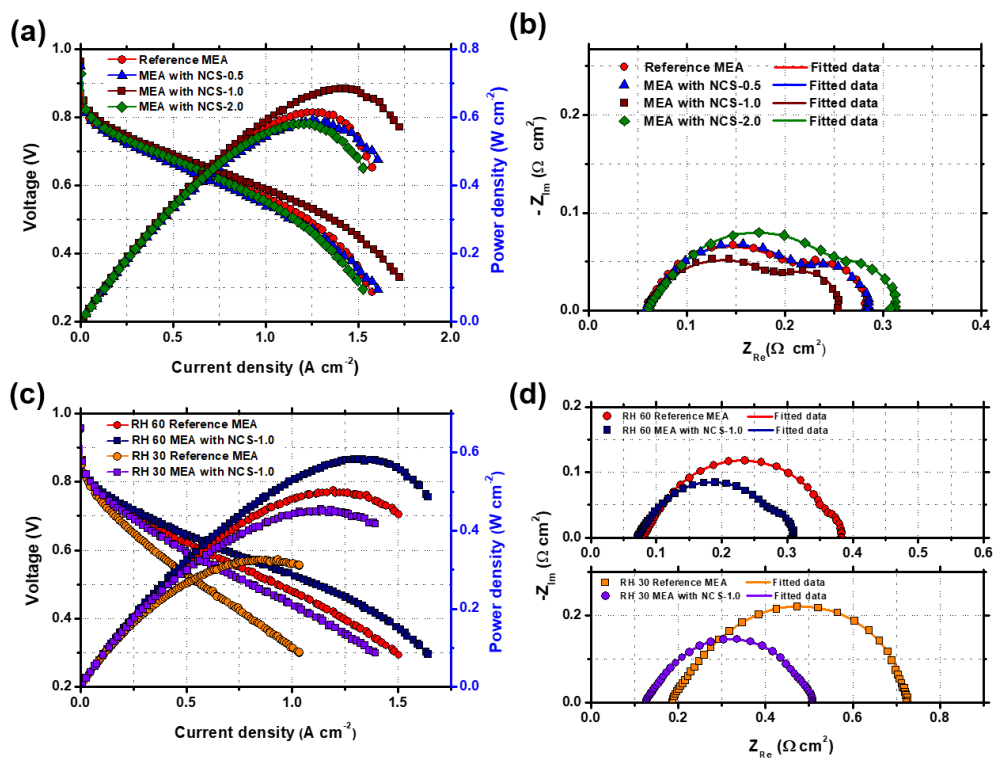


Figure 2.11. (a) Polarization curves at 70 ° C with flow rate (H_2 /Air = 150/350 cc/min) and (b) corresponding EIS spectra at 0.6 V. (c) Polarization curves with low Rh conditions (30% and 60%) and (b) corresponding EIS spectra at 0.6V.

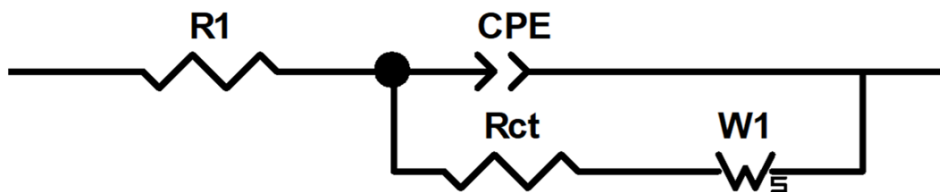


Figure 2.12. Equivalent circuit model for the cathodic reaction of the PEMFC (R_1 = internal membrane resistance, R_{ct} = charge transfer resistance of the cathode, CPE = constant phase element of the cathode, and W_1 = Warburg impedance).

MEAs	Maximum power density [W cm^{-2}]	Current density at 0.6 V [A cm^{-2}]	R_{membrane} [$\Omega \text{ cm}^2$]	$R_{\text{LF-HF}}$ [$\Omega \text{ cm}^2$]
Full RH condition				
Reference MEA	0.627	0.867	0.0595	0.224
MEA with NCS-0.5	0.592	0.776	0.0601	0.223
MEA with NCS-1.0	0.685	0.956	0.0612	0.193
MEA with NCS-2.0	0.58	0.836	0.0618	0.246
Low RH conditions				
RH60				
Reference MEA	0.502	0.576	0.081807	0.301505
MEA with NCS-1.0	0.579	0.676	0.072135	0.236638
RH 30				
Reference MEA	0.326	0.347	0.18434	0.5394
MEA with NCS-1.0	0.454	0.486	0.126403	0.381787

Table 2.1 Summary of the current–voltage (I–V) performance and the EIS fitted values.

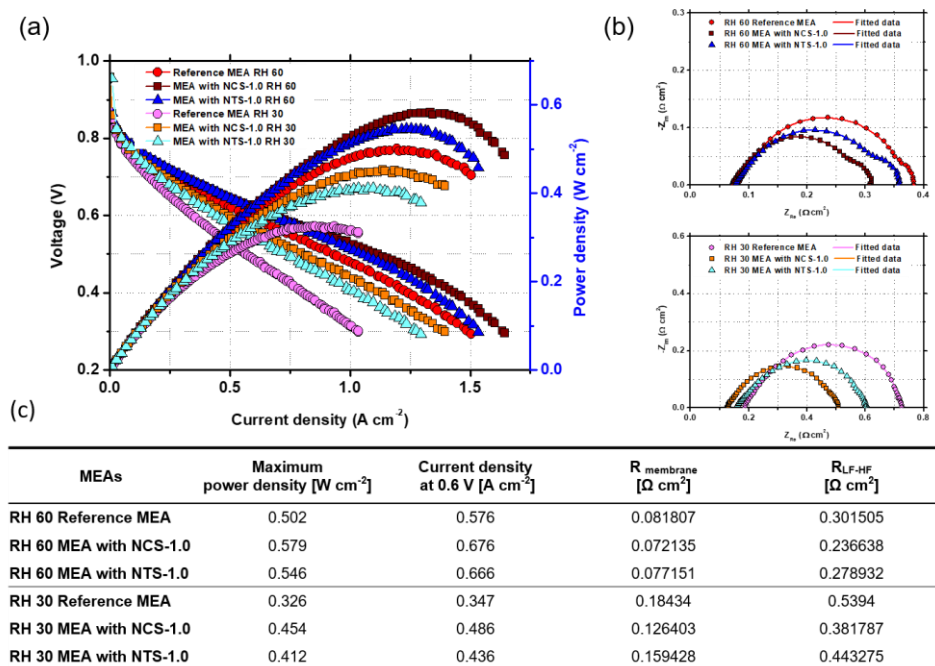


Figure 2.13. (a) Current density–voltage (J–V) curves and the (b) EIS spectra for the prepared MEAs including the MEA with Nafion®/TiO₂ structures with varying the RH condition. (c) Summary of I–V performance and EIS fitted values

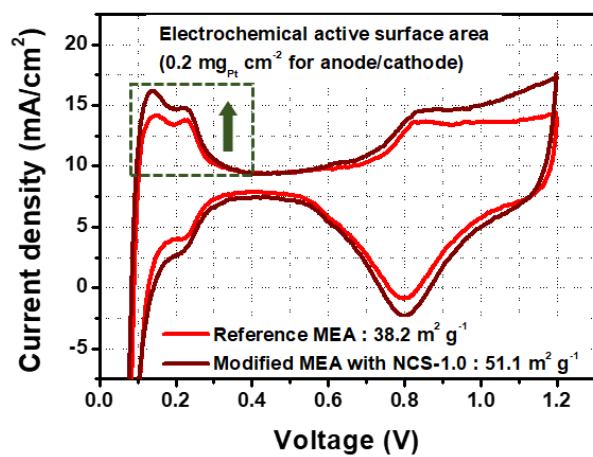
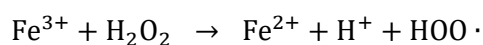
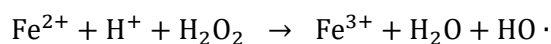


Figure 2.14. Cyclic voltammetry (CV) measurements of the reference MEA and the MEA with NCS-1.0.

2.3.3. Evaluation of chemical durability of the modified membrane

Next, to assess the effect of Nafion[®]/CeO₂ on the chemical durability of the PEMFC, the in-situ OCV holding test was conducted. **Figure 2.15 a** shows the OCV change of the MEAs over 276 h under accelerated environmental conditions. We selected the end-of-life (EOL) point when the OCV fell by more than ~ 20% of the initial OCV (DOE protocol). The LSV measurements were conducted in the middle (0 h, 100 h, and 200 h) and at the end of the test to evaluate hydrogen crossover. And the maximum power densities were measured during the test (0 h, 100 h, and 200 h) to figure out the decrease in the MEA performance. At the first 100 h, the degradation rates of the reference MEA and the MEA with NCS-1.0 were calculated about 1.28 mV h⁻¹ and 0.53 mV h⁻¹, respectively. Noticeably, the reference MEA showed an abrupt decrease of the OCV at around 270 h and showed the OCV of 0.7 V at 276 h. After the 276 h OCV holding test, the degradation rate of the MEA with NCS-1.0 (0.42 mV h⁻¹) was measured ~ 41% lower than that of the reference MEA (0.71 mV h⁻¹). In the case of reference MEA, the hydrogen crossover current density slightly increased during 200 h and largely increased over 25 mA cm⁻² at 276 h, while the MEA with NCS-1.0 showed stable maintenance during 200 h and 61% lower value of hydrogen crossover current density than that of the

reference MEA after 276 h. (**Figure 2.15 b**) Moreover, as shown in **Figure 2.15 c**, the cell performance of the reference MEA significantly decreased during the OCV holding test and consequently showed 41.6% lower performance compared to the initial one at 200 h. On the other hand, the MEA with NCS-1.0 showed only an 8.6% decrease in performance after 200 h. These results indicate that the introduced CeO₂ within the dendritic structures, located between the membrane and the electrode improves the chemical durability from the membrane degradations due to its radical scavenging ability. Also, we further confirmed the radical scavenging effect of the CeO₂ nanoparticles by performing the 100 h OCV holding test for the MEA with NTS-1.0 and it exhibited a much faster degradation rate than that of the MEA with NCS-1.0 (**Figure 2.16**). Besides, an ex-situ Fenton's test, which is an accelerated chemical degradation assessment, was performed with the pure Nafion® 211 membrane and membrane with NCS-1.0. The prepared membranes were soaked in an H₂O₂ solution containing Fe²⁺ ions, which continually generated free radicals through the following reaction⁴⁴,



In high radical concentrations, the chemical decomposition of the membranes is accelerated; the degradation rate can be quantified by measuring the amount of F^- ions originating from the decomposition of the main and side chains of the PFSA polymer (Nafion® membrane).

$$\text{The fluorine emission rate (FER) } (\mu\text{mol h}^{-1}\text{g}^{-1}) = \frac{C \times V}{t \times m \times M_F}$$

In the above equation, C is the F^- concentration (g cm^{-3}), V is the volume of the solution (cm^3), t is the test time (h), m is the membrane weight after drying (g), and M_F is the molecular weight of F (g mol^{-1}). **Figure 2.15 d** shows the FER of the reference membrane and the membrane with NCS-1.0. Measurement was carried out over 72 h and the Fenton's solution was replaced every 24 h. The greater the FER the faster the chemical degradation of the membranes. The membrane with NCS-1.0 showed a slower FER ($1.765 \mu\text{mol h}^{-1}\text{g}^{-1}$ at 72 h) than the reference membrane ($2.803 \mu\text{mol h}^{-1}\text{g}^{-1}$ at 72 h), and the difference in rates increases with time, i.e., from 24 h to 72 h. The results of the Fenton's tests confirm the effectiveness of the Nafion®/CeO₂ structures in achieving durable PEMFCs.

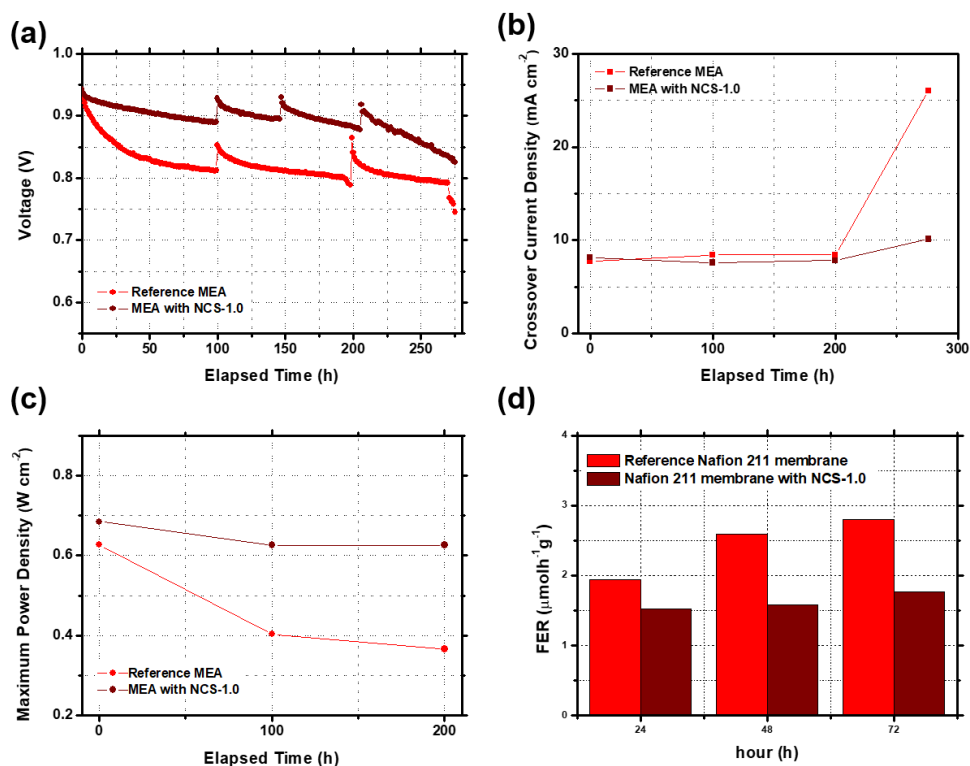


Figure 2.15. (a) The OCV decay spectra over 276h testing under accelerated condition and corresponding (b) hydrogen crossover current density from linear sweep voltammetry (LSV) measurements and (c) maximum power density with the prepared MEAs. (d) Fluorine ion emission rate (FER) from 72 h Fenton' s test with the prepared membranes.

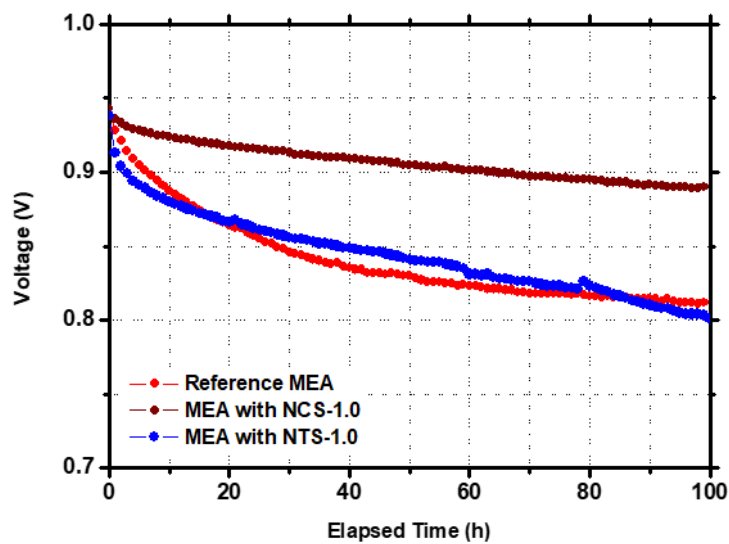


Figure 2.16. The OCV decay spectra from the OCV holding tests (over 100 h) with the prepared MEAs including the MEA with Nafion[®]/TiO₂ structures.

2.4. Conclusion

This study proposed a membrane modification method using multifunctional dendritic Nafion[®]/CeO₂ structures to improve both the durability and performance of PEMFCs. Using the electrospray deposition method, the dendritic structures were successfully introduced onto the cathode-side of the membrane; the degree of structural growth was carefully controlled as a function of deposition time. The high surface area and porosity of the optimum dendritic structures improved PEMFC performance due to the enlarged interfacial contact area between the membrane and the catalyst layer and the presence of microscale voids between the catalyst layer and the GDL. This improved catalyst utilization and mass transport of the reactant. Moreover, the Nafion[®]/CeO₂ structures improved the chemical durability of the PEMFC due to the excellent radical removal ability of the CeO₂ at the forefront of the membrane. This enhanced chemical durability was confirmed with an in-situ OCV holding test (over 100 h) and ex-situ Fenton's test (over 72 h).

2.5. References

- (1) Costamagna, P.; Srinivasan, S. Quantum Jumps in the Pemfc Science and Technology from the 1960s to the Year 2000: Part Ii. Engineering, Technology Development and Application Aspects. *J. Power Sources* **2001**, *102* (1–2), 253–269.
- (2) Guerrero Moreno, N.; Cisneros Molina, M.; Gervasio, D.; Pérez Robles, J. F. Approaches to Polymer Electrolyte Membrane Fuel Cells (Pemfcs) and Their Cost. *Renew. Sust. Energ. Rev.* **2015**, *52*, 897–906.
- (3) Zatoń, M.; Rozière, J.; Jones, D. J. Current Understanding of Chemical Degradation Mechanisms of Perfluorosulfonic Acid Membranes and Their Mitigation Strategies: A Review. *Sustain. Energ. Fuels* **2017**, *1* (3), 409–438.
- (4) Majlan, E. H.; Rohendi, D.; Daud, W. R. W.; Husaini, T.; Haque, M. A. Electrode for Proton Exchange Membrane Fuel Cells: A Review. *Renew. Sust. Energ. Rev.* **2018**, *89*, 117–134.
- (5) Tetteh, E. B.; Lee, H.–Y.; Shin, C.–H.; Kim, S.–h.; Ham, H. C.; Tran, T.–N.; Jang, J.–H.; Yoo, S. J.; Yu, J.–S. New Ptmg Alloy with Durable Electrocatalytic Performance for Oxygen Reduction Reaction in Proton Exchange Membrane Fuel Cell. *ACS Energy Lett.* **2020**, *5* (5), 1601–1609.

- (6) Brouzgou, A.; Song, S. Q.; Tsiakaras, P. Low and Non-Platinum Electrocatalysts for Pemfcs: Current Status, Challenges and Prospects. *Appl. Catal. B Environ.* **2012**, *127*, 371–388.
- (7) Serov, A.; Kwak, C. Review of Non-Platinum Anode Catalysts for Dmfc and Pemfc Application. *Appl. Catal. B Environ.* **2009**, *90* (3–4), 313–320.
- (8) Li, L.; Shen, S.; Wei, G.; Li, X.; Yang, K.; Feng, Q.; Zhang, J. A Comprehensive Investigation on Pyrolyzed Fe–N–C Composites as Highly Efficient Electrocatalyst toward the Oxygen Reduction Reaction of Pemfcs. *ACS Appl. Mater. Interfaces* **2019**, *11* (15), 14126–14135.
- (9) Yang, X.; Zhang, G.; Du, L.; Zhang, J.; Chiang, F. K.; Wen, Y.; Wang, X.; Wu, Y.; Chen, N.; Sun, S. Pgm-Free Fe/N/C and Ultralow Loading Pt/C Hybrid Cathode Catalysts with Enhanced Stability and Activity in Pem Fuel Cells. *ACS Appl. Mater. Interfaces* **2020**, *12* (12), 13739–13749.
- (10) Billy, E.; Maillard, F.; Morin, A.; Guetaz, L.; Emieux, F.; Thurier, C.; Doppelt, P.; Donet, S.; Mailley, S. Impact of Ultra-Low Pt Loadings on the Performance of Anode/Cathode in a Proton-Exchange Membrane Fuel Cell. *J. Power Sources* **2010**, *195* (9), 2737–2746.

- (11) Klingele, M.; Breitwieser, M.; Zengerle, R.; Thiele, S. Direct Deposition of Proton Exchange Membranes Enabling High Performance Hydrogen Fuel Cells. *J. Mater. Chem. A* **2015**, *3* (21), 11239–11245.
- (12) Cho, H.; Kim, S. M.; Kang, Y. S.; Kim, J.; Jang, S.; Kim, M.; Park, H.; Bang, J. W.; Seo, S.; Suh, K.-Y.; Sung, Y.-E.; Choi, M. Multiplex Lithography for Multilevel Multiscale Architectures and Its Application to Polymer Electrolyte Membrane Fuel Cell. *Nat. Commun.* **2015**, *6* (8484), 1–8.
- (13) Wu, J.; Yuan, X. Z.; Martin, J. J.; Wang, H.; Zhang, J.; Shen, J.; Wu, S.; Merida, W. A Review of Pem Fuel Cell Durability: Degradation Mechanisms and Mitigation Strategies. *J. Power Sources* **2008**, *184* (1), 104–119.
- (14) Yuan, X.-Z.; Li, H.; Zhang, S.; Martin, J.; Wang, H. A Review of Polymer Electrolyte Membrane Fuel Cell Durability Test Protocols. *J. Power Sources* **2011**, *196* (22), 9107–9116.
- (15) Stanic, V. Mechanism of Pinhole Formation in Membrane Electrode Assemblies for Pem Fuel Cells. *ECS Proceedings Volumes* **2004**, *2004-21* (1), 391–401.
- (16) Kusoglu, A.; Weber, A. Z. A Mechanistic Model for Pinhole Growth in Fuel-Cell Membranes During Cyclic Loads. *J. Electrochem. Soc.* **2014**, *161* (8), E3311–E3322.

- (17) Coms, F. D. The Chemistry of Fuel Cell Membrane Chemical Degradation. *ECS Trans.* **2008**, *16* (2), 235–255.
- (18) Curtin, D. E.; Lousenberg, R. D.; Henry, T. J.; Tangeman, P. C.; Tisack, M. E. Advanced Materials for Improved Pemfc Performance and Life. *J. Power Sources* **2004**, *131* (1–2), 41–48.
- (19) Rodgers, M. P.; Bonville, L. J.; Kunz, H. R.; Slattery, D. K.; Fenton, J. M. Fuel Cell Perfluorinated Sulfonic Acid Membrane Degradation Correlating Accelerated Stress Testing and Lifetime. *Chem. Rev.* **2012**, *112* (11), 6075–6103.
- (20) Breitwieser, M.; Klose, C.; Hartmann, A.; Büchler, A.; Klingele, M.; Vierrath, S.; Zengerle, R.; Thiele, S. Cerium Oxide Decorated Polymer Nanofibers as Effective Membrane Reinforcement for Durable, High-Performance Fuel Cells. *Adv. Energy Mater.* **2016**, *7* (6) 1602100.
- (21) Yoon, K. R.; Lee, K. A.; Jo, S.; Yook, S. H.; Lee, K. Y.; Kim, I.-D.; Kim, J. Y. Mussel-Inspired Polydopamine-Treated Reinforced Composite Membranes with Self-Supported Ceox Radical Scavengers for Highly Stable Pem Fuel Cells. *Adv. Funct. Mater.* **2019**, *29* (3) 1806929.
- (22) Trogadas, P.; Parrondo, J.; Ramani, V. Platinum Supported on Ceo₂ Effectively Scavenges Free Radicals within the Electrolyte

- of an Operating Fuel Cell. *Chem. Commun.* **2011**, 47 (41), 11549–11551.
- (23) Coms, F. D.; Liu, H.; Owejan, J. E. Mitigation of Perfluorosulfonic Acid Membrane Chemical Degradation Using Cerium and Manganese Ions. *ECS Trans.* **2008**, 16 (2), 1735–1747.
- (24) Vinothkannan, M.; Ramakrishnan, S.; Kim, A. R.; Lee, H. K.; Yoo, D. J. Ceria Stabilized by Titanium Carbide as a Sustainable Filler in the Nafion Matrix Improves the Mechanical Integrity, Electrochemical Durability, and Hydrogen Impermeability of Proton–Exchange Membrane Fuel Cells: Effects of the Filler Content. *ACS Appl. Mater. Interfaces* **2020**, 12 (5), 5704–5716.
- (25) Vinothkannan, M.; Hariprasad, R.; Ramakrishnan, S.; Kim, A. R.; Yoo, D. J. Potential Bifunctional Filler (CeO₂–Acnts) for Nafion Matrix toward Extended Electrochemical Power Density and Durability in Proton–Exchange Membrane Fuel Cells Operating at Reduced Relative Humidity. *ACS Sustainable Chemistry & Engineering* **2019**, 7 (15), 12847–12857.
- (26) Endoh, E. Development of Highly Durable Pfsa Membrane and Mea for Pemfc under High Temperature and Low Humidity Conditions. *ECS Trans.* **2008**, 16 (2), 1229–1240.

- (27) U.S. DOE Fuel Cell Technologies Office Multi-Year Research, Development, and Demonstration Plan. <https://www.energy.gov/eere/fuelcells/downloads/fuel-cell-technologies-office-multi-year-research-development-and-22> (accessed June, 2020).
- (28) Castillo, J. L.; Martin, S.; Rodriguez-Perez, D.; Higuera, F. J.; Garcia-Ybarra, P. L. Nanostructured Porous Coatings Via Electrospray Atomization and Deposition of Nanoparticle Suspensions. *J. Aerosol Sci.* **2018**, *125*, 148–163.
- (29) Tang, J.; Gomez, A. Controlled Mesoporous Film Formation from the Deposition of Electrosprayed Nanoparticles. *Aerosol Sci. Tech.* **2017**, *51* (6), 755–765.
- (30) Kulkarni, P.; Biswas, P. A Brownian Dynamics Simulation to Predict Morphology of Nanoparticle Deposits in the Presence of Interparticle Interactions. *Aerosol Sci. Tech.* **2004**, *38* (6), 541–554.
- (31) Wang, Z.; Tang, H.; Zhang, H.; Lei, M.; Chen, R.; Xiao, P.; Pan, M. Synthesis of Nafion/CeO₂ Hybrid for Chemically Durable Proton Exchange Membrane of Fuel Cell. *J. Membr. Sci.* **2012**, *421–422*, 201–210.
- (32) Pearman, B. P.; Mohajeri, N.; Brooker, R. P.; Rodgers, M. P.; Slattery, D. K.; Hampton, M. D.; Cullen, D. A.; Seal, S. The

- Degradation Mitigation Effect of Cerium Oxide in Polymer Electrolyte Membranes in Extended Fuel Cell Durability Tests. *J. Power Sources* **2013**, *225*, 75–83.
- (33) Lee, D. H.; Jo, W.; Yuk, S.; Choi, J.; Choi, S.; Doo, G.; Lee, D. W.; Kim, H. T. In-Plane Channel-Structured Catalyst Layer for Polymer Electrolyte Membrane Fuel Cells. *ACS Appl. Mater. Interfaces* **2018**, *10* (5), 4682–4688.
- (34) Jang, S.; Kim, M.; Kang, Y. S.; Choi, Y. W.; Kim, S. M.; Sung, Y. E.; Choi, M. Facile Multiscale Patterning by Creep-Assisted Sequential Imprinting and Fuel Cell Application. *ACS Appl. Mater. Interfaces* **2016**, *8* (18), 11459–11465.
- (35) Ahn, C.-Y.; Jang, S.; Cho, Y.-H.; Choi, J.; Kim, S.; Kim, S. M.; Sung, Y.-E.; Choi, M. Guided Cracking of Electrodes by Stretching Prism-Patterned Membrane Electrode Assemblies for High-Performance Fuel Cells. *Sci. Rep.* **2018**, *8* (1), 1257.
- (36) Schlick, S.; Danilczuk, M.; Drews, A. R.; Kukreja, R. S. Scavenging of Hydroxyl Radicals by Ceria Nanoparticles: Effect of Particle Size and Concentration. *J. Phys. Chem. C* **2016**, *120* (12), 6885–6890.
- (37) Sudarsanam, P.; Hillary, B.; Malleshram, B.; Rao, B. G.; Amin, M. H.; Nafady, A.; Alsalmeh, A. M.; Reddy, B. M.; Bhargava, S. K. Designing Cu₂O Nanoparticle-Decorated CeO₂

- Nanocubes for Catalytic Soot Oxidation: Role of the Nanointerface in the Catalytic Performance of Heterostructured Nanomaterials. *Langmuir* **2016**, *32* (9), 2208–2215.
- (38) Dunnick, K. M.; Pillai, R.; Pisane, K. L.; Stefaniak, A. B.; Sabolsky, E. M.; Leonard, S. S. The Effect of Cerium Oxide Nanoparticle Valence State on Reactive Oxygen Species and Toxicity. *Biol Trace Elem Res* **2015**, *166* (1), 96–107.
- (39) Khawaji, M.; Chadwick, D. Au – Pd Nps Immobilised on Nanostructured Ceria and Titania: Impact of Support Morphology on the Catalytic Activity for Selective Oxidation. *Catalysis Science & Technology* **2018**, *8* (10), 2529–2539.
- (40) Ketpang, K.; Lee, K.; Shanmugam, S. Facile Synthesis of Porous Metal Oxide Nanotubes and Modified Nafion Composite Membranes for Polymer Electrolyte Fuel Cells Operated under Low Relative Humidity. *ACS Appl. Mater. Interfaces* **2014**, *6* (19), 16734–16744.
- (41) Velayutham, P.; Sahu, A.; Parthasarathy, S. A Nafion–Ceria Composite Membrane Electrolyte for Reduced Methanol Crossover in Direct Methanol Fuel Cells. *Energies* **2017**, *10* (2) 259.
- (42) Torija, S.; Prieto–Sanchez, L.; Ashton, S. J. In–Situ Electrochemically Active Surface Area Evaluation of an Open–

- Cathode Polymer Electrolyte Membrane Fuel Cell Stack. *J. Power Sources* **2016**, *327*, 543–547.
- (43) Jeon, Y.; Kim, D. J.; Koh, J. K.; Ji, Y.; Kim, J. H.; Shul, Y. G. Interface–Designed Membranes with Shape–Controlled Patterns for High–Performance Polymer Electrolyte Membrane Fuel Cells. *Sci. Rep.* **2015**, *5*, 16394.
- (44) Gubler, L.; Dockheer, S. M.; Koppenol, W. H. Radical ($\text{HO}\cdot$, $\text{H}\cdot$, and $\text{HOO}\cdot$) Formation and Ionomer Degradation in Polymer Electrolyte Fuel Cells. *J. Electrochem. Soc.* **2011**, *158* (7) B755–B769.

Chapter 3. 1-D Ionomer-free Electrode with Ultra-low Catalyst Loading

Note: This chapter is reproduced from the work I co-authored with Sungjun Kim (co-first author), published in *Journal of the Electrochemical Society*, **2021**, 168, 114505.

3.1. Introduction

Owing to increasing interest in eco-friendly hydrogen energy, proton exchange membrane fuel cells (PEMFCs) have been studied widely because of their high efficiency and zero-emission operation.¹ However, the commercial use of PEMFCs is still limited by their high cost primarily due to platinum group metal (PGM) catalysts, especially for sluggish oxygen reduction reaction (ORR) in acidic media. As an attractive low-cost alternative, anion exchange membrane fuel cells (AEMFCs) are emerging because they can utilize less expensive materials for catalysts in a less-corrosive alkaline environment.²⁻⁴ Intensive studies have been conducted to develop anion exchange polymers (AEPs) with high ionic conductivity and chemical-mechanical stability under AEMFC operating conditions. Thanks to these efforts, several PGM-based AEMFCs have been able to achieve promising power density and durability based on the novel AEPs,⁵ such as aryl-ether free polyaromatics,⁶⁻⁹ radiation-grafted polyethylene,^{10, 11} and polynorbornenes.^{12, 13} In addition, several AEMFCs based on these novel AEPs exhibited remarkable performance even without the use of PGM-based ORR catalysts.¹⁴⁻¹⁶ However, the basic material for AEPs has not yet been established, and the commercially available AEPs like FAA-3 (FuMA-Tech) and AS-4 (Tokuyama) used in

most AEMFC studies show much inferior properties to the newly developed AEPs. Moreover, the phenyl groups in their polymer backbone interacting strongly with the metal-based catalyst surface adversely affect the performance and durability of the AEMFC when the AEPs are used as ionomer.^{17, 18}

Typically, a fuel cell electrode is composed of carbon-supported nano-catalysts concealed by a thin-film ionomer.¹⁹ However, this conventional electrode structure has been found to suffer from significant mass transport resistance, especially under high-current load. This is because the ionomer thin film on the catalyst surface significantly limits the gas permeation flux to the active sites.²⁰ As mentioned above, the phenyl groups in the anion exchange ionomer interact strongly with the metal-based catalyst surface. The densification of ionomer near the catalyst surface due to the ionomer-catalyst interaction can exacerbate this transport-related problem.²¹ Moreover, the phenyl groups strongly adsorbed on the metal-based catalyst surface adversely affect the durability of AEMFC cathode. The fuel cell cathode is exposed to a relatively high potential during AEMFC operation. Under such a condition, the ionomer's phenyl groups, which are adsorbed on the cathode catalyst, tend to be easily oxidized, thus forming phenolic compounds. This acidic phenol produced by oxidizing the ionomer exerts detrimental

effects on the cathode by neutralizing the basic hydroxide ions or adsorbing onto the surface of the catalyst.²² Therefore, the introduction of an ionomer-free nature to AEMFC cathode can alleviate the gas transport related problem and improve their durability.

Since there is no hydrophilic material that aids in the transport of water and ions in the ionomer-free electrode, it is essential for the development of electrode design that considers the efficient ion and water transport within the electrode. In particular, the balancing water behavior in AEMFCs is more challenging than that in PEMFCs, so it is highly desirable to develop a novel electrode design to achieve improved mass transfer.^{23–25} Considering this, 1-D electrodes are the most promising structure because of their simple pathways for water and ion transport, and it is no coincidence that the successful application of ionomer-free 1-D electrodes, such as nanostructured thin film (NSTF), to the PEMFC system.^{26–28} However, only a few reports have been reported on the design of an AEMFC electrode attempted to replace the current electrode or solve the mass transport-related problem.^{29, 30}

In this chapter, an ionomer-free electrode with vertically aligned 1-D structures for AEMFCs was introduced for the first time. By

employing a facile hydrothermal synthesis procedure, the length-controlled nanoarrays were grown on the microporous layer (MPL) side of the gas diffusion layer (GDL), which could be employed as a gas diffusion electrode (GDE), via the successive deposition of the catalyst materials. The characteristics of the silver-deposited nanorods were evaluated by different measurement techniques, including field emission scanning electron microscopy (FE-SEM), transmission electron microscopy (TEM), and the corresponding energy-dispersive X-ray (EDX) analysis, and X-ray photoelectron spectroscopy (XPS). A vertically aligned GDE (VGDE) was prepared and applied to the cathode of the membrane electrode assembly (MEA) to analyze the characteristics and effectiveness of the ionomer-free electrode under alkaline conditions. To focus on the effectiveness of the VGDE in AEMFC by excluding the impact of high-efficiency membranes and functional catalysts, the commercially available AEM and silver catalysts were employed. The electrochemical characteristics of the prepared electrodes were evaluated by their polarization curves, electrochemical impedance spectroscopy (EIS) spectra, and linear sweep voltammograms. The stability of the ionomer-free electrode was further investigated. Additionally, we analyzed the mass transport phenomenon and AEMFC operational characteristics depending on the electrode

thickness and composition of the ionomer-free electrode.

3.2. Experimental methods

3.2.1. Preparation of ionomer-free electrode with catalyst coated 1-D nanostructures

GDL (JNT-30-A3) was cut to an area of $25 \times 25 \text{ mm}^2$. Next, the ZnO nanoparticles (diameter, 50 nm) were dispersed in ethanol (1 wt.%) and spin-coated on GDL for 60 s at 3000 rpm to introduce the seed layer of ZnO to the polytetrafluoroethylene (PTFE) side of GDL. Afterward, the solvent was removed by drying GDL at 80°C for 5 min. For the hydrothermal synthesis, a solution containing zinc nitrate hexahydrate (0.025 M), HMTA (0.0125 M), and a certain amount of ammonium hydroxide solution was prepared to grow the ZnO nanoarrays.^{31, 32} Further, a 100 ml Teflon-lined stainless-steel autoclave was filled with the prepared solution up to 80% of the volume, and the prepared GDL was floated on the solution. Owing to the hydrophobic character of the PTFE-coated mesoporous layer, GDL was floating during the reaction, and ZnO only grew on the PTFE side of GDL. The hydrothermal growth proceeded at 80°C for 6 – 36h. Thereafter, GDL was removed, rinsed with deionized (DI) water, and dried by blowing nitrogen gas. To coat the catalyst onto the ZnO nanorods, silver was deposited by vacuum thermal evaporation.

3.2.2. MEA Preparation

A single-cell test was conducted to evaluate the performance of VGDE. The catalyst-coated membrane (CCM) method was employed to fabricate the anode catalyst layer. Briefly, PtRu/C (60 wt.%, Johnson Matthey Co.) was employed as the catalyst for the hydrogen oxidation reaction (HOR), and a catalyst ink was prepared by ultrasonically dispersing the HOR catalyst with an appropriate amount of an FAA-3-SOLUTE-10 ionomer solution (FuMA-Tech Co., ionomer to carbon weight ratio was 0.5) in an aqueous solution of ethanol and isopropyl alcohol. The prepared catalyst ink was directly sprayed onto the FAA-3-50 membrane (50 μm , FuMA-Tech Co.), and the metal loading on the anode catalyst layer was fixed at 0.4 mg cm^{-2} . Subsequently, the anode-coated membrane was dried for >12 h to evaporate the residual solvent in the catalyst layer. Before fabricating MEA, the prepared anode-coated membrane and silver-coated VGDE were immersed in a 1.0 M KOH (aq) solution for 1 h, after which they were washed with distilled water to remove all the excess KOH ions. Thereafter, the anode-coated membrane was sandwiched in anode GDL (JNT-30-A3, JNTG) and the prepared VGDE without the hot-pressing process. The active area of MEA was restricted to 5 cm^2 by Teflon gaskets. For comparison, a conventional electrode containing a carbon-

supported silver nanoparticle catalyst (60 wt.% Ag/C, Premetek) and the FAA-3-SOLUTE-10 ionomer (ionomer to carbon weight ratio was 0.5) were fabricated. The conventional electrode was prepared by directly coating the Ag/C catalyst ink onto GDL (JNT-30-A3, JNTG) via the above-mentioned spray-coating process. The Ag loading of the Ag/C electrode was fixed at 0.1 mg cm^{-2} , which was somewhat higher than that of Ag-coated VGDE ($\sim 0.06 \text{ mg cm}^{-2}$).

3.2.3. Characterization.

FE-SEM (Carl Zeiss) was employed to obtain the surface and cross-sectional images of VGDE. The chemical states of ZnO and silver were measured by XPS (AXIS-HSi, Kratos) utilizing an Al K α source. TEM (JEM-F200, JEOL) and EDX were employed to analyze the elemental distribution of the Ag/ZnO nanorods. To prepare the TEM sample, the Ag/ZnO layer on the PTFE side of GDL was exfoliated from GDL and sufficiently dispersed in isopropanol (IPA) by ultrasonication in a 1:1000 wt. ratio. Afterward, the dispersion was drop-casted on the TEM grids.

A half-cell experiment was conducted with a three-electrode system to compare the oxygen reduction kinetics of Ag-coated VGDE with Ag/C electrode in a 0.1 M KOH (aq) electrolyte. A Pt mesh and a Hg/HgO electrode (-0.85 V vs. RHE) were utilized as

the counter and reference electrodes, respectively. The active area of the working electrodes was fixed at 1.0 cm^2 . The I–V polarization curves of ORR were obtained at a scan rate of 5 mVs^{-1} in an oxygen-saturated 0.1 KOH (aq) electrolyte. Thereafter, the resistance of the solution was measured by EIS utilizing FRA32 (Metrohm Autolab) to compensate for the loss of the iR voltage.

To evaluate the single-cell performance, the prepared MEA was sandwiched in two graphite plates with a one-channel serpentine-type flow field. The single-cell was assembled by applying torque ($\sim 9.0\text{ N m}$) to each screw of the single-cell and connecting to a single-cell test station (CNL Energy). Humidified hydrogen and oxygen were fed into the anode and cathode at constant flow rates of 0.8 and 1.0 L min^{-1} , respectively, without any backpressure, and the relative humidities of the hydrogen and oxygen gases were $\sim 80\%$ and 90% , respectively. The temperature of the operating cell was fixed at $60\text{ }^{\circ}\text{C}$. The I–V polarization curves were obtained at a scan rate of 10 mA cm^{-2} after stabilizing the performance under the above conditions. Further, EIS was performed in the galvanostatic mode at 0.1 A cm^{-2} with an amplitude of 0.01 A cm^{-2} and 0.4 V with an amplitude of 5 mV in the frequency range of 100 kHz – 100 mHz . Cyclic voltammetry (CV) experiments were conducted to compare the electrochemically active surface area of the Ag cathode catalyst

layer. Fully humidified hydrogen and nitrogen were fed to the anode and the cathode at 0.2 L min^{-1} , respectively. The cyclic voltammetry was conducted at a cell temperature of 60° C , and the voltage sweep range was $0.05\text{--}1.20 \text{ V}$ (vs. anode) at a scan rate of 0.02 V s^{-1} using the Ag cathode as the working electrode and the PtRu anode as the counter electrode. The durability test was performed at a constant current density of 0.3 A cm^{-2} .

3.3. Results and discussion

3.3.1. Fabrication and characterization of the nanostructured gas diffusion electrode

Figure 3.1 a and c illustrate the fabrication processes of the ionomer-free electrode with vertically aligned 1-D nanostructures and conventional porous electrodes. Unlike the conventional electrode, which is prepared with ionomer and catalyst powder, the ionomer-free electrode is fabricated by growing ZnO 1-D nanorod and deposition of the catalyst layer. The fabrication proceeded as follows: (i) a 50 nm ZnO nanoparticle solution was spin-coated onto the PTFE side of GDL to introduce the seed layer there. Owing to the hydrophobic character of PTFE, the nanoparticles were exclusively deposited on the surface of GDL. (ii) The spin-coated GDL was transferred into the hydrothermal autoclave containing the prepared solution comprising zinc nitrate hexahydrate, HMTA, and an ammonium hydroxide solution.³³ The nanorods grew on the surface of GDL outwardly because GDL floated during the hydrothermal reaction. (**Figure 3.2**, GDL with a synthesized ZnO denoted as ZnO/GDL) The temperature was fixed at 80 ° C, and the length of the nanorods was controlled by varying the growth time. (iii) After removing the residual solvent by washing and blowing with DI water

and nitrogen gas, respectively, the silver catalyst layer ($\sim 0.06 \text{ mg cm}^{-2}$) was deposited by a vacuum thermal evaporator. **Figure 3.1 b** and **d** show the top-view of the scanning electron microscopy (SEM) images of VGDE and conventional electrode. Compared to **Figure 3.2 b**, as shown in **Figure 3.1 b**, the silver layer was ultra-thin and uniformly deposited, so it did not exhibit any distinct change compared to ZnO/GDL. In addition, compared to **Figure 3.1 d**, VGDE had a vertical gas pathway between the nanorods instead of having a tiny, randomized pore. For an in-depth analysis of the composition of the silver-deposited nanorods, the XPS measurements were conducted before and after the silver deposition of VGDE. **Figures 3.3 a** and **b** show the XPS spectra of Zn 2p and Ag 3d, respectively. In **Figure 3.3 a**, the peak values of ZnO/GDL were obtained at 1022 and 1045 eV, which indicated the bonding of the O ions to the Zn ones of the Zn $2p_{3/2}$ and $2p_{1/2}$ states, respectively.³⁴ However, regarding VGDE, the Zn $2p_{3/2}$ and $2p_{1/2}$ peaks almost disappeared, which implied that the surface of ZnO was uniformly covered by silver. **Figure 3.3 b** shows the Ag $3d_{5/2}$ and Ag $3d_{3/2}$ peaks of VGDE at 368.1 and 374.1 eV, respectively.³⁵ To further investigate the distribution of the elements at VGDE, EDX coupled with TEM was conducted. The mapping images of the Ag/ZnO nanorods indicated that the ZnO nanorods were uniformly covered by a silver layer with $\sim 30 \text{ nm}$ thick.

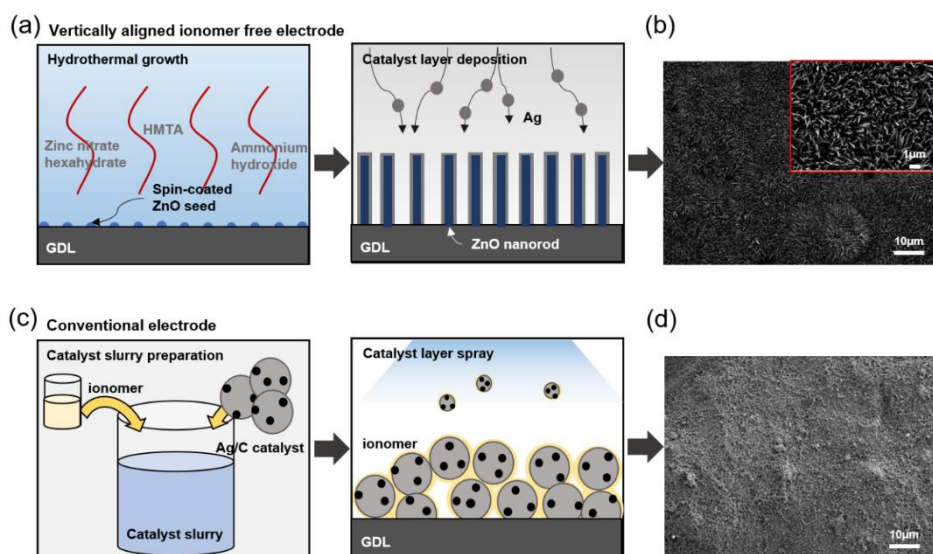


Figure 3.1. (a) Schematic illustrations of the fabrication process of VGDE. (b) Surface morphological SEM images VGDE containing the silver catalyst layer (inset: high magnified images). (c) Schematic illustrations of the fabrication process of the conventional electrode. (d) Surface morphological SEM image of the conventional porous electrode containing Ag/C catalyst and ionomer

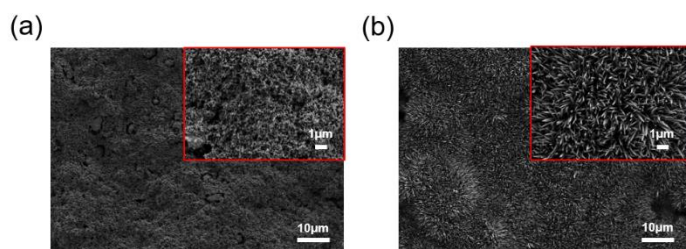


Figure 3.2. Surface morphological SEM images of (a) GDL and (b) hydrothermally synthesized ZnO on GDL (ZnO/GDL).

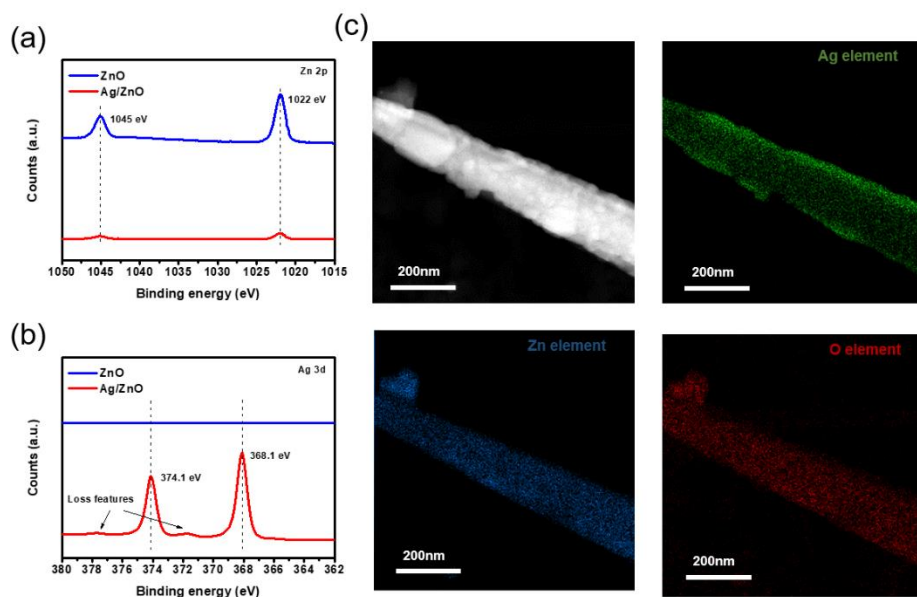


Figure 3.3. XPS spectra of (a) Zn 2p and (b) Ag 3d of GDL/ZnO and VGDE. (c) TEM and EDX mapping images

3.3.2. Fuel cell evaluation from mass transport and electrode durability perspective

To apply the VGDE and compare it to the conventional electrode, single cells possessing a conventional GDE and VGDE at the cathode were fabricated. The VGDE was fabricated from 12-hour growth of ZnO and the thermal deposition of the silver layer with the loading of $0.06 \text{ mg}_{\text{Ag}} \text{ cm}^{-2}$, while the conventional electrode was prepared by spraying the prepared catalysts ink with the loading of $0.1 \text{ mg}_{\text{Ag}} \text{ cm}^{-2}$ (denoted as CGDE). The AEMFC performances of MEA with VGDE and MEA with CGDE are shown in **Figure 3.4 a**. The MEA containing VGDE exhibited ~80% increased performance (0.215 W cm^{-2}) compared with MEA containing CGDE (0.120 W cm^{-2}) despite the higher loss of activation, which was observed in the low-current-density region. In particular, The MEA with VGDE showed a significantly reduced voltage loss in the high current region compared to the MEA with CGDE, resulting in more than twice the limiting current density (0.87 A cm^{-2} and 0.42 A cm^{-2} , respectively). These results suggested that VGDE maximized oxygen transport due to the ionomer-free 1-D nanostructure. Compared with other previously reported papers, these results are sufficiently comparable even use of the commercial membrane and extremely low catalyst loading (**Table 3.1**).^{15, 29, 36-43} To clarify the effects of the VGDE on the

enhanced AEMFC performance, EIS analysis was conducted for two different regions (0.1 A cm^{-2} and 0.4 V) (**Figure 3.4 b**). In the kinetic region (0.1 A cm^{-2}), the charge-transfer resistance (R_{ct}) of MEA containing VGDE was much higher than that of MEA containing CGDE, which was consistent with the half-cell ORR test of the GDEs (**Figure 3.5**). The insufficient kinetic activity of VGDE was due to the lower dispersion of the catalytic material (Ag) of the $\sim 30 \text{ nm}$ thick Ag layer on the ZnO nanoarrays in Ag VGDE compared to several-nm sized Ag nanoparticles of in Ag CGDE. To substantiate this, cyclic voltammograms of the two Ag cathodes were obtained using the PtRu anode as a counter electrode (**Figure 3.6**). The ECSAs of the Ag electrodes were determined from the charge corresponding to the Ag oxide reduction peak based on the charge density of $420 \text{ } \mu\text{C cm}^{-2}$ for the reduction of the Ag oxide to metallic Ag.⁴⁴⁻⁴⁶ As a result, the ECSA of the Ag VGDE was $18.1 \text{ m}^2 \text{ g}_{\text{Ag}}^{-1}$ which is more than 3 times lower than that of the Ag CGDE ($62.4 \text{ m}^2 \text{ g}_{\text{Ag}}^{-1}$).

On the other hand, at 0.4 V , the R_{ct} of MEA containing VGDE was lower than that of MEA containing CGDE. Notably, the tail of the arc in the low-frequency region of MEA containing CGDE, which was related to the mass transport of the fuel cells, was much larger than that of MEA containing VGDE. This result demonstrated that the improved mass transport and performance of MEA containing VGDE

were mainly due to the structural characteristics of the vertically aligned 1-D structures. As shown in **Figure 3.4 c**, the ion- and mass-transfer pathways in VGDE possess a much lower tortuosity compared with the conventional electrode, which consisted of a randomly arranged carbon-supported catalyst and ionomer. Owing to the geometrical advantages of the vertically aligned 1-D structure, VGDE exhibited high performance without an ionomer. Additionally, the ionomer-free nature of VGDE offers an advantage regarding the local oxygen transport resistance since the ionomer layer on the catalytic surface substantially hindered oxygen diffusion into the active site. Hence, VGDE exhibited a higher performance compared with CGDE, especially in the high-current region, which is closely related to the mass transport in the electrode. Furthermore, the VGDE offered an additional advantage regarding the durability of AEMFC. To compare the durability of the two cathodes, MEAs containing VGDE and CGDE were operated at 0.3 A cm^{-2} for the stability test after evaluating the performance of the single cell (**Figure 3.7**). As shown in **Figure 3.7**, MEA containing VGDE was more durable compared with MEA containing CGDE.

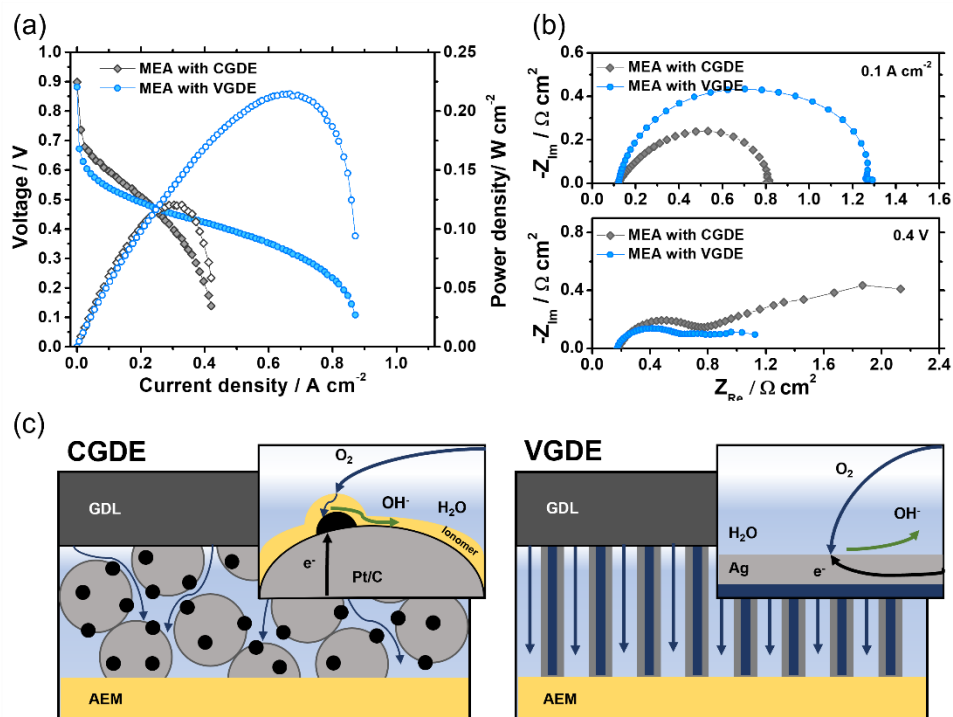


Figure 3.4. (a) Polarization curves of MEAs containing a CGDE ($0.1 \text{ mg}_{\text{Ag}} \text{ cm}^{-2}$) and VGDE ($0.06 \text{ mg}_{\text{Ag}} \text{ cm}^{-2}$). Both MEAs were sufficiently activated under constant voltage-operated conditions. (b) EIS spectra at 0.1 V and 0.1 A cm^{-2} correspond to MEAs containing CGDE and VGDE. (c) Schematic illustrations of the oxygen transport behaviors of CGDE VGDE

Membrane, thickness	Anode	Cathode	Condition (H ₂ /O ₂ flow rate, back pressure)	P _{max} [mW/cm ²]
Commercially available AEP				
FAA ^a , 50µm (this work)	PtRu/C, 0.4 mg/cm ²	Ag, 0.06 mg/cm ² (ionomer free)	0.8 / 1.0 lpm, -	215
FAA ^a , 70µm (1)	Pt black, 0.5mg _{pl} /cm ²	Ag NP, 0.5mg/cm ²	0.2 / 0.2 lpm, 250kPa	208
A201 ^b , 28µm (2)	Pt/C, 0.2mg _{pl} /cm ²	Ag/C, 1.0mg/cm ²	0.2 / 0.2 lpm, ~206.8kPa	190
A901 ^b , 10µm (3)	Pt/C, 0.5mg _{pl} /cm ²	1.Ag NW, 1.05mg/cm ² 2.Ag/GNS, 1.05mg/cm ²	0.5 / 0.5 lpm, ~206.8 kPa	1. 164.4 2. 287.8
aQAPS-S8 ^c , 30~40µm (4)	Pt/C, 0.8	Ag/C, 1.0mg/cm ²	1.0 / 0.5 slpm, -	200
Advanced AEP				
ETFE-AEM ^d , 71µm (5)	Pt/C, 0.5mg _{pl} /cm ²	Ag/C, 0.5mg/cm ²	2 / 2 lpm, -	19
Nafion-QAPS BPM ^d , ~57µm (6)	Pt/C, 0.5mg _{pl} /cm ²	Ag/C, 1.0mg/cm ²	0.08 / 0.15 lpm, -	~ 27
ETFE-AEM ^d , 21µm (7)	PtRu/C, 0.4mg _{pl} /cm ²	Ag/C, 1.0mg/cm ²	1lpm/1lpm, -	1110
Nafion-QAPS BPM ^d , ~57µm (8)	Pt/C, 0.4mg _{pl} /cm ²	Ag/C, 1.0mg/cm ²	0.05 / 0.08lpm, -	19.3
,30 µm (9)	RuPdIr/C, 0.2mg/cm ²	AgPd, 1.0mg/cm ²	0.15 / 1 slpm, ~100 / ~300 kPa	950
(LDPE-g)-poly(VBTMA+Cl-) ^d , (10)	PtRu/C, 0.06 mg _{pl} /cm ²	FAA-3@Ag, 4.5 mg/cm ²	-	~ 200

^a Fuma-tech, ^b Tokuyama, ^c Hephias Energy Co., ^d lab made

Table 3.1. Comparison of MEA compositions and key parameters between the previously reported AEMFCs and this study.

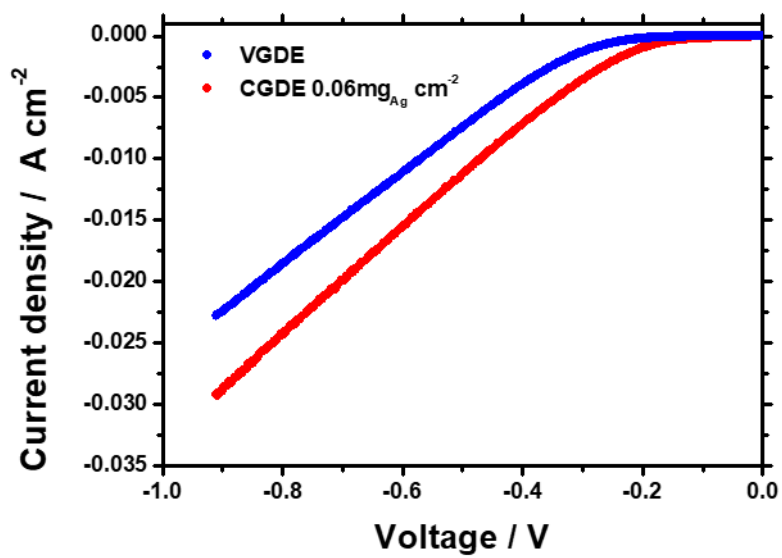


Figure 3.5. Linear sweep voltammograms of a CGDE and VGDE_{12h} (0.06 mg_{Ag} cm⁻²)

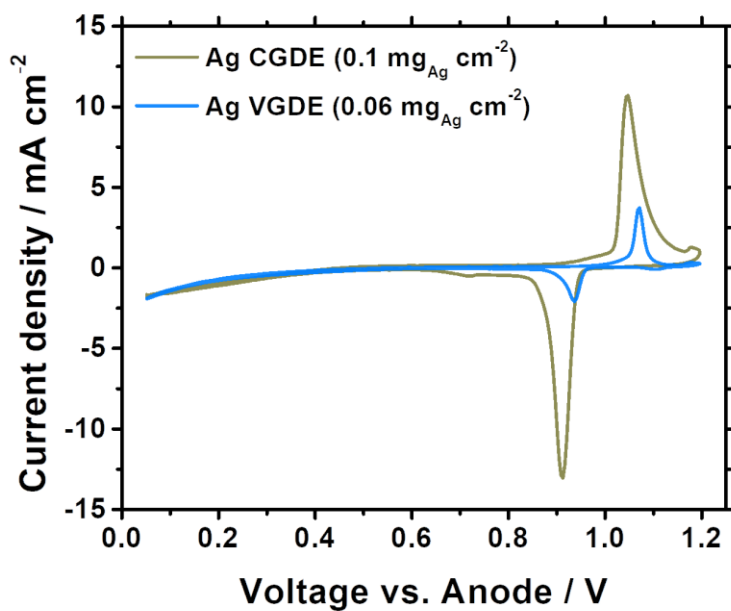


Figure 3.6. Cyclic voltammograms of Ag CGDE (0.10 mg_{Ag} cm⁻²) and Ag VGDE_{12h} (0.06 mg_{Ag} cm⁻²)

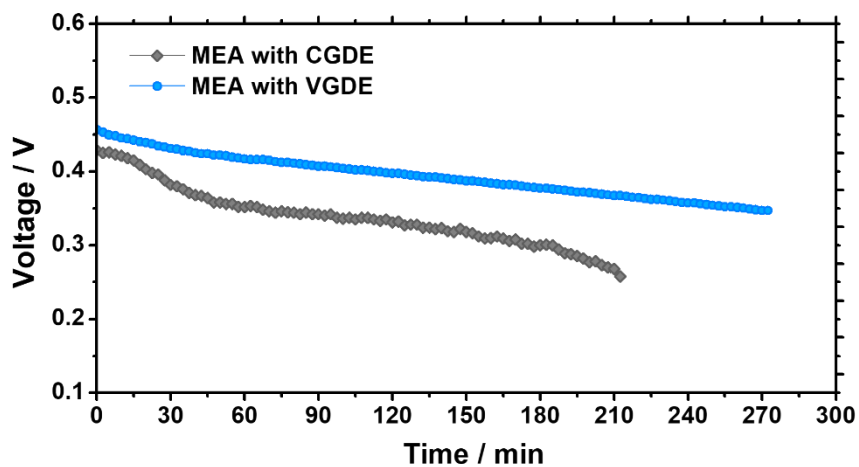


Figure 3.7. Spectra of the voltage decay under an operating condition of 0.3 A cm^{-2} for MEAs containing CGDE and VGDE.

3.3.3. Voltage drop due to the water shortage and optimization of electrode thickness

After analyzing the voltage loss at the high current region and electrode stability of VGDE compared to the CGDE, operational characteristics of the AEMFC with VGDE at the cathode were carefully investigated based on the water consumption and oxygen transport characteristic by varying the electrode thickness, electrode compositions, and membrane thickness. First of all, a silver thin film electrode (without the ZnO rods) on GDL (Ag/GDL) was prepared to identify the behavior of the ionomer-free electrode without the 1-D structure. As shown in **Figure 3.8**, The Ag/GDL electrode exhibited a much lower cell performance than the conventional Ag/C electrode did. This inferior performance of the Ag/GDL electrode might be due to the lower dispersion of the catalytic material (silver) in Ag/GDL compared with that of the Ag/C electrode. Moreover, the limiting current densities of the Ag/GDL electrodes were lower than the conventional Ag/C electrode and decreased with an increasing amount of the coated silver. These results implied that the thin electrodes without ZnO rods could not have a good path for the oxygen supply, which got worse as the silver layer blocked the pores of MPL.

To determine the correlation between the length and growth time of the ZnO nanorods, they were grown for 6, 12, 18, and 36 h. **Figure 3.9 a** shows cross-sectional SEM images of the VGDE with increasing growth time. The length of the ZnO nanorods increased as the growth time increased until 18 h, after which it exhibited a moderate growth rate at 18–36 h (**Figure 3.9 b**, ~ 1.9 , ~ 2.8 , ~ 3.7 , and $\sim 4.3 \mu\text{m}$ at 6, 12, 18, and 36 h, respectively), maintaining the diameter of the structure. To find out the effect of the electrode thickness on AEM operation in ionomer-free electrode, the MEAs, which utilized silver-coated VGDE with different ZnO rod growth times (denoted as VGDE_x, where x is the growth time) as the cathode, were prepared; the silver loading amounts of all the electrodes were fixed at $0.06 \text{ mg}_{\text{Ag}} \text{ cm}^{-2}$. As shown in **Figure 3.9 c**, all VGDEs containing the 1-D nanorods exhibited higher cell performances and limiting current densities than the Ag/GDL electrode. Notably, as the growth time of ZnO increased from 6 to 18 h, i.e., as the length of the ZnO rod grew from ~ 1.9 to $\sim 3.7 \mu\text{m}$, the limiting current densities also increased from 0.22 to 1.07 A cm^{-2} . As previously analyzed, this indicated that the 1-D nanostructures increased mass transport by providing oxygen path and reducing the amount of silver in pores of MPL, which suggested expanded electrode area and enhanced catalyst utilization. However, as the

growth time was increased to 36 h ($\sim 4.3 \mu\text{m}$), the cell voltage suddenly dropped at $\sim 0.3 \text{ A cm}^{-2}$, and the current density was limited to 0.612 A cm^{-2} . This sudden deterioration in the polarization curve was frequent with VGDE_36h even after increasing the amount of the deposited catalytic material (from 0.06 to $0.12 \text{ mg}_{\text{Ag}} \text{ cm}^{-2}$, **Figure 3.10 a**) or changing the catalytic material (from silver to platinum, **Figure 3.10 b**). Notably, when 0.05 mg cm^{-2} platinum, instead of silver, was deposited on VGDE_36h (Pt/VGDE_36h), its kinetic overpotential was significantly reduced, although the breakage occurred at $\sim 0.3 \text{ A cm}^{-2}$, similar to the case of coating 0.06 mg cm^{-2} Ag on VGDE_36h. These results showed that fuel cell operations are limited in high current due to factors other than oxygen, which is ion and water. Since the water is consumed at the cathode in alkaline conditions, water is essential for ORR. Moreover, there was no ionomer for transferring ions in VGDEs, so the ions were only transported through the connection of the accumulated water over the surface of the electrode. In this case, ion transport in the electrode could be dramatically inhibited because of the breakage of the water connection via its consumption during the cathodic reaction in the operation of AEMFC. These caused a rapid decrease in the performance of AEMFC. Thus, the longer the electrode length, the greater the likelihood of water limiting. Therefore, dissimilar to

relatively thin VGDE_12h, the thicker electrodes exhibited concave (VGDE_18h at around 0.38 A cm^{-2}) or discontinuous polarization curves (VGDE_36h at around 0.3 A cm^{-2}).

Next, to figure out the effect of ionomer on alleviating water limitation of the thick electrode (e.g. VGDE_36h), commercial AEI (FAA-3-SOLUTE-10, FuMA-Tech) was coated on VGDE_36h with loadings of 0.04 and $0.08 \text{ mg}_{\text{ionomer}} \text{ cm}^{-2}$. As shown in **Figure 3.11 a**, the excessive ionomer coating ($0.08 \text{ mg}_{\text{ionomer}} \text{ cm}^{-2}$) significantly reduced performance because the coated ionomer layer interfered with the transport of oxygen to the catalytic surface. However, the sudden decrease in the performance of VGDE_36h was not observed with a small amount of the ionomer ($0.04 \text{ mg}_{\text{ionomer}} \text{ cm}^{-2}$), even it showed slightly increased overpotential at the low-current density region. Thus, ionomers can fill the space within the electrode created by the prolonged ZnO to prevent the breakage of water connections and help with ion transport. However, as mentioned earlier, the use of ionomers interferes with oxygen transport and causes electrode degradation. Thus, it is possible to increase the water supply in the cathode to maintain the water connection according to the longer electrode thickness.

Finally, to check the membrane thickness effect on the mass

transport of the AEMFC with VGDE, FAA-3 membranes with different thicknesses of 30 and 50 μm were prepared. **Figure 3.11 b** shows the polarization curves of MEAs employing FAA-3 membranes with different thicknesses. It was observed that the sudden voltage drops of MEA containing VGDE_36h were eliminated as the membrane thickness decreased from 50 to 30 μm . This is because the improved water management in AEMFC due to an increased back diffusion by introducing a thinner membrane (a shortened diffusion pathway) mitigated the water depletion challenge at the cathode. Also, VGDE_12h with a 30 μm thick membrane showed an increase in the limiting current density as well as a decrease in ohmic loss, compared with that of a 50 μm membrane.

To straightforwardly summarize the water consumption and oxygen transport characteristics of AMEFC with the ionomer-free electrode at the cathode, limiting current density according to the electrode thickness was shown in **Figure 3.11 c** based on the results of **Figure 3.9 c**. It seems that a higher electrode led to enhancing oxygen transport in the ionomer-free electrode. However, too thick electrode thickness caused water shortage by water consumption of the ORR in the alkaline medium, which led to ion-conducting inhibition. Therefore, in the design of an ionomer-free electrode, the optimal thickness should be considered for oxygen transport and

water consumption, and, additionally, a thin electrolyte membrane can improve water back diffusion to ease water shortage.

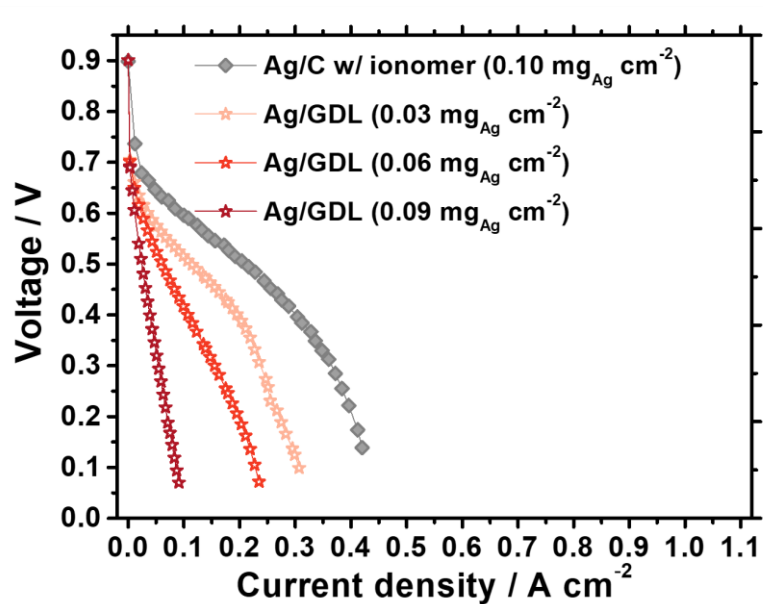


Figure 3.8. Polarization curves of MEAs containing silver-deposited GDL (Ag/GDL) and MEA containing CGDE at the cathode.

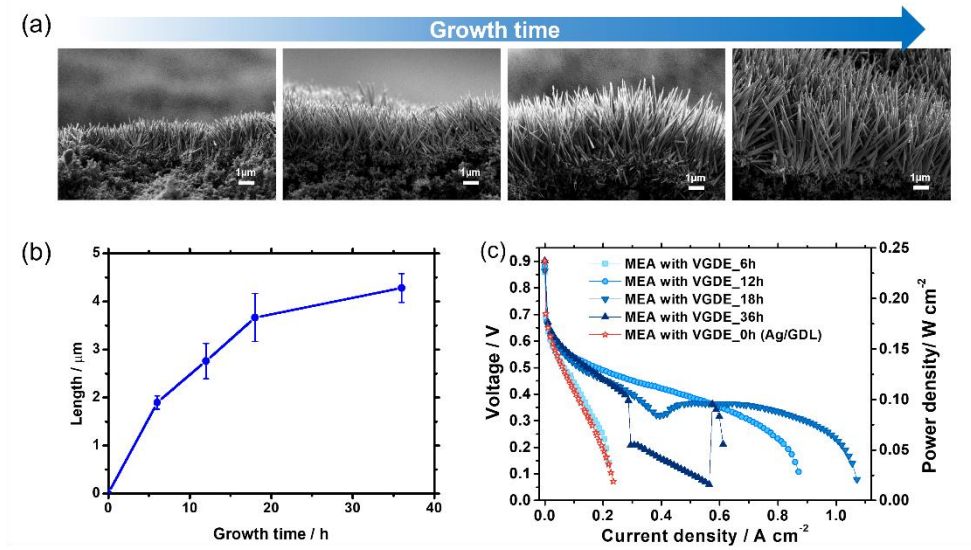


Figure 3.9. (a) Cross-sectional SEM images of the ZnO nanorod on GDL, which was synthesized at 80 °C for 6, 12, 18, and 36 h, in regular order. (b) The measured length of the ZnO nanorods of different growth times. (c) AEMFC polarization curves of MEAs containing VGDEs with different ZnO growth times (0, 6, 12, 18, and 36 h)

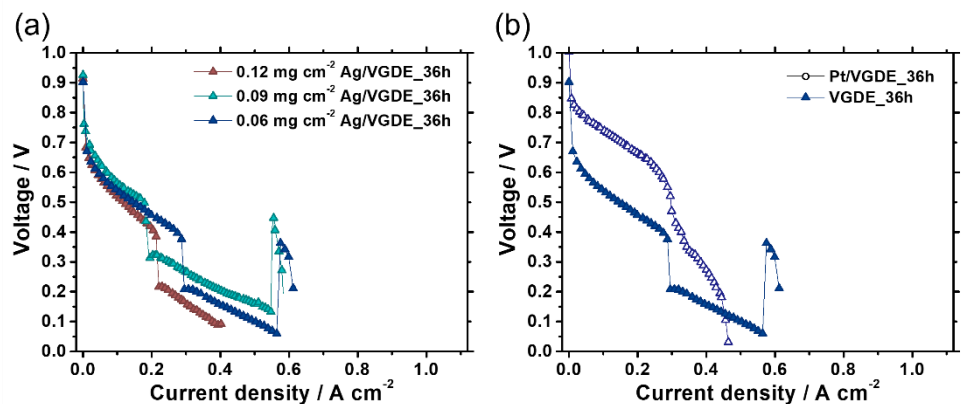


Figure 3.10. Polarization curves of (a) MEAs containing VGDE_36h with different silver catalyst loadings and (b) MEAs containing VGDE_36h and platinum-coated VGDE_36h instead of the silver layer.

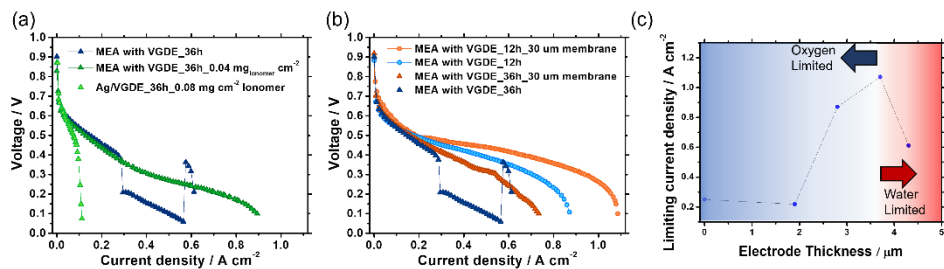


Figure 3.11. AEMFC polarization curves of (a) MEAs containing VGDE_36h, ionomer-sprayed VGDEs, (b) 30 and 50 μ m MEAs containing VGDE_12h and VGDE_36h. (c) limiting current density concerning the electrode thickness.

3.4. Conclusion

This study presented a novel ionomer-free electrode comprising a vertically aligned 1-D structure for an AEMFC cathode. Based on a facile synthetic process, we successfully fabricated the vertically aligned nanorods on GDL. The vertically aligned 1-D structure in the electrode afforded the effective utilization of the active sites, and most significantly, it enhanced the mass transport of the reactants within the electrode. Additionally, the ionomer-free nature of the electrode improved the oxygen transport on the catalyst surface and stability of AEMFC by mitigating the adsorption due to the phenyl group of the ionomers.

3.5. References

- (1) Wang, Y.; Chen, K. S.; Mishler, J.; Cho, S. C.; Adroher, X. C. A review of polymer electrolyte membrane fuel cells: Technology, applications, and needs on fundamental research. *Applied Energy*. **2011**, 88(4), 981–1007.
- (2) Firouzaie, H. A.; Mustain, W. E. Catalytic Advantages, Challenges, and Priorities in Alkaline Membrane Fuel Cells. *Acs Catal*. **2020**, 10(1), 225–34.
- (3) Ramaswamy, N.; Mukerjee, S. Alkaline Anion–Exchange Membrane Fuel Cells: Challenges in Electrocatalysis and Interfacial Charge Transfer. *Chem Rev*. **2019**, 119(23), 11945–11979.
- (4) He, Y.; Liu, S.; Priest, C.; Shi, Q.; Wu, G. Atomically dispersed metal–nitrogen–carbon catalysts for fuel cells: advances in catalyst design, electrode performance, and durability improvement. *Chem Soc Rev*. **2020**, 49(11), 3484–3524.
- (5) Chen, N.; Lee, Y. M. Anion exchange polyelectrolytes for membranes and ionomers. *Progress in Polymer Science*. **2021**, 113.
- (6) Maurya, S.; Noh, S.; Matanovic, I.; Park, E. J.; Villarrubia, C. N.; Martinez, U.; Han, J.; Bae, C.; Kim Y. S. Rational design of polyaromatic ionomers for alkaline membrane fuel cells with > 1

- W cm^{-2} power density. *Energy & Environmental Science*. **2018**, 11(11), 3283–3291.
- (7) Cha, M. S.; Park, J. E.; Kim, S.; Han, S. H.; Shin, S. H.; Yang, S. H.; Kim, T.-H.; Yu, D. M.; So, S.; Hong, Y. T.; Yoon, S. J.; Oh, S.-G.; Kang, S. Y.; Kim, O.-H.; Park, H. S.; Bae B.; Sung, Y.-E.; Cho, Y.-H.; Lee, J. Y. Poly(carbazole)-based anion-conducting materials with high performance and durability for energy conversion devices. *Energy & Environmental Science*. **2020**, 13(10), 3633–3645.
- (8) Chen, N.; Wang, H. H.; Kim, S. P.; Kim, H. M.; Lee, W. H.; Hu, C.; Bae, J. Y.; Sim, E. S.; Chung, Y.-C.; Jang, J.-H.; Yoo, S. J.; Zhuang, Y.; Lee, Y. M. Poly(fluorenyl aryl piperidinium) membranes and ionomers for anion exchange membrane fuel cells. *Nat Commun*. **2021**, 12(1), 2367.
- (9) Chen, N.; Hu, C.; Wang, H. H.; Kim, S. P.; Kim, H. M.; Lee, W. H.; Bae, J. Y.; Park, J. H.; Lee, Y. M. Poly(Alkyl-Terphenyl Piperidinium) Ionomers and Membranes with an Outstanding Alkaline-Membrane Fuel-Cell Performance of 2.58 W cm^{-2} . *Angew Chem Int Ed Engl*. **2021**, 60(14), 7710–7718.
- (10) Wang, L.; Bellini, M.; Miller, H. A.; Varcoe, J. R. A high conductivity ultrathin anion-exchange membrane with 500+ h alkali stability for use in alkaline membrane fuel cells that can

- achieve 2 W cm⁻² at 80 ° C. *Journal of Materials Chemistry A*. **2018**, 6(31), 15404–15412.
- (11) Wang, L. Q.; Peng, X.; Mustain, W. E.; Varcoe, J. R. Radiation-grafted anion-exchange membranes: the switch from low- to high-density polyethylene leads to remarkably enhanced fuel cell performance. *Energy & Environmental Science*. **2019**, 12(5), 1575–1579.
- (12) Mandal, M.; Huang, G.; Hassan, N. U.; Mustain, W. E.; Kohl, P. A. Poly(norbornene) anion conductive membranes: homopolymer, block copolymer and random copolymer properties and performance. *Journal of Materials Chemistry A*. **2020**, 8(34), 17568–17578.
- (13) Ul Hassan, N.; Mandal, M.; Huang, G.; Firouzjaie, H. A.; Kohl, P. A.; Mustain, W. E. Achieving High-Performance and 2000 h Stability in Anion Exchange Membrane Fuel Cells by Manipulating Ionomer Properties and Electrode Optimization. *Advanced Energy Materials*. **2020**, 10(40).
- (14) Wang, J.; Zhao, Y.; Setzler, B. P.; Rojas-Carbonell, S.; Ben, Y. C.; Amel, A.; Page, M.; Wang, L.; Hu, K.; Shi, L.; Gottesfeld, S.; Xu, B.; Yan, Y. Poly(aryl piperidinium) membranes and ionomers for hydroxide exchange membrane fuel cells. *Nature Energy*. **2019**, 4(5), 392–398.

- (15) Wang, L.; Brink, J. J.; Varcoe, J. R. The first anion-exchange membrane fuel cell to exceed 1 W cm^{-2} at 70 degrees C with a non-Pt-group (O2) cathode. *Chem Commun (Camb)*. **2017**, 53(86), 11771–11773.
- (16) Adabi, H.; Shakouri, A.; Ul Hassan, N.; Varcoe, J. R.; Zulevi, B.; Serov, A.; Regalbuto, J. R.; Mustain, W. E. High-performing commercial Fe-N-C cathode electrocatalyst for anion-exchange membrane fuel cells. *Nature Energy*. **2021**, 6, 834–843
- (17) Matanovic, I.; Chung, H. T.; Kim, Y. S. Benzene Adsorption: A Significant Inhibitor for the Hydrogen Oxidation Reaction in Alkaline Conditions. *J Phys Chem Lett*. **2017**, 8(19), 4918–4924.
- (18) Mustain, W. E.; Chatenet, M.; Page, M.; Kim, Y. S. Durability challenges of anion exchange membrane fuel cells. *Energy & Environmental Science*. **2020**, 13(9), 2805–2838.
- (19) Wang, G. L.; Zou, L. L.; Huang, Q. H.; Zou, Z. Q.; Yang, H. Multidimensional nanostructured membrane electrode assemblies for proton exchange membrane fuel cell applications. *Journal of Materials Chemistry A*. **2019**, 7(16), 9447–9477.
- (20) Kongkanand, A.; Mathias, M. F. The Priority and Challenge of High-Power Performance of Low-Platinum Proton-Exchange Membrane Fuel Cells. *J Phys Chem Lett*. **2016**, 7(7), 1127–1137.

- (21) Jinnouchi, R.; Kudo, K.; Kitano, N.; Morimoto, Y. Molecular dynamics simulations on O₂ permeation through nafion ionomer on platinum surface (vol 188, pg 767, 2016). *Electrochim Acta*. **2018**, 287, 160–.
- (22) Maurya, S.; Lee, A. S.; Li, D. G.; Park, E. J.; Leonard, D. P., Noh, S.; Bae, C.; Kim, Y. S. On the origin of permanent performance loss of anion exchange membrane fuel cells: Electrochemical oxidation of phenyl group. *Journal of Power Sources*. **2019**, 436(1), 226866
- (23) Omasta, T. J.; Park, A. M.; LaManna, J. M.; Zhang, Y.; Peng, X.; Wang, L.; Jacobson, D. L.; Varcoe, J. R. Hussey, D. S.; Pivovar, B. S.; Mustain, W. E. Beyond catalysis and membranes: visualizing and solving the challenge of electrode water accumulation and flooding in AEMFCs. *Energy & Environmental Science*. **2018**, 11(3), 551–558.
- (24) Jang, S.; Her, M.; Kim, S.; Jang, J.-H.; Chae, J. E.; Choi, J.; Choi, M.; Kim, S. M.; Cho, Y.-H.; Sung, Y.-E.; Yoo, S. J. Membrane/Electrode Interface Design for Effective Water Management in Alkaline Membrane Fuel Cells. *ACS Appl Mater Interfaces*. **2019**, 11(38), 34805–34811.
- (25) Omasta, T. J.; Wang, L.; Peng, X.; Lewis, C. A.; Varcoe, J. R.; Mustain, W. E. Importance of balancing membrane and electrode

- water in anion exchange membrane fuel cells. *Journal of Power Sources*. **2018**, 375, 205–213.
- (26) Debe, M. K. Tutorial on the Fundamental Characteristics and Practical Properties of Nanostructured Thin Film (NSTF) Catalysts. *J Electrochem Soc*. **2013**, 160(6), F522–F534.
- (27) Ganesan, A.; Narayanasamy, M. Ultra–low loading of platinum in proton exchange membrane–based fuel cells: a brief review. *Mater Renew Sustain*. **2019**, 8(4).
- (28) Mardle, P.; Thirunavukkarasu, G.; Guan, S.; Chiu, Y. L.; Du, S. Comparative Study of PtNi Nanowire Array Electrodes toward Oxygen Reduction Reaction by Half–Cell Measurement and PEMFC Test. *ACS Appl Mater Interfaces*. **2020**, 12(38), 42832–42841.
- (29) Zeng, L.; Zhao, T. S.; An L. A high–performance supportless silver nanowire catalyst for anion exchange membrane fuel cells. *Journal of Materials Chemistry A*. **2015**, 3(4), 1410–1416.
- (30) Qin, B.; Yu, H.; Gao X.; Yao, D.; Sun, X.; Song, W.; Yi, B.; Shao, Z. Ultrathin IrRu nanowire networks with high performance and durability for the hydrogen oxidation reaction in alkaline anion exchange membrane fuel cells. *Journal of Materials Chemistry A*. **2018**, 6(41), 20374–20382.

- (31) Hu, J.; Sun, Y.; Zhang, W.; Gao, F.; Li, P.; Jiang, D. Chen, Y. Fabrication of hierarchical structures with ZnO nanowires on micropillars by UV soft imprinting and hydrothermal growth for a controlled morphology and wettability. *Appl Surf Sci.* **2014**, 317, 545–551.
- (32) Hong, S.-H.; Kim, M.-H.; Yun, H.-W.; Paik, T.; Lee, H. Solution-processed fabrication of superhydrophobic hierarchical zinc oxide nanostructures via nanotransfer printing and hydrothermal growth. *Surf Coat Tech.* **2017**, 331, 189–195.
- (33) Tian, J.-H.; Hu, J.; Li, S.-S.; Zhang, F.; Liu J.; Shi J.; Li, X.; Tian, Z.-Q.; Chen, Y. Improved seedless hydrothermal synthesis of dense and ultralong ZnO nanowires. *Nanotechnology.* **2011**, 22(24), 245601.
- (34) Li, S.-S.; Su Y.-K.; Improvement of the performance in Cr-doped ZnO memory devices via control of oxygen defects. *Rsc Adv.* **2019**, 9(6, 2941–2947.
- (35) Ferrara, A. M.; Carapeto, A. P.; do Rego, A. M. B. X-ray photoelectron spectroscopy: Silver salts revisited. *Vacuum.* **2012**, 86(12), 1988–1991.
- (36) Gu, S.; Sheng, W.; Cai, R.; Alia S. M.; Song, S.; Jensen, K. O.; Yan, Y. An efficient Ag-ionomer interface for hydroxide

- exchange membrane fuel cells. *Chem Commun (Camb)*. **2013**, 49(2), 131–133.
- (37) Xin, L.; Zhang, Z.; Wang, Z.; Qi, J.; Li, W. Carbon supported Ag nanoparticles as high-performance cathode catalyst for H₂/O₂ anion exchange membrane fuel cell. *Front Chem*. **2013**, 1, 16.
- (38) Truong, V. M.; Yang, M.-K.; Yang, H. Functionalized Carbon Black Supported Silver (Ag/C) Catalysts in Cathode Electrode for Alkaline Anion Exchange Membrane Fuel Cells. *International Journal of Precision Engineering and Manufacturing-Green Technology*. **2019**, 6(4), 711–721.
- (39) Poynton, S. D.; Kizewski, J. P.; Slade, R. C. T.; Varcoe, J. R. Novel electrolyte membranes and non-Pt catalysts for low temperature fuel cells. *Solid State Ionics*. **2010**, 181(3–4), 219–222.
- (40) Peng, S.; Xu, X.; Lu, S.; Sui, P.-C.; Djilali, N.; Xiang, Y. A self-humidifying acidic-alkaline bipolar membrane fuel cell. *Journal of Power Sources*. **2015**, 299, 273–279.
- (41) Xu, X.; Peng, S.; Lu, S.; Gong, J.; Zhang, J.; Huang, W.; Xiang, Y. Modulation of the microstructure of the Ag/C-based alkaline cathode via the ionomer content for a bipolar membrane fuel cell. *Journal of Power Sources*. **2017**, 354, 92–99.

- (42) Tatus–Portnoy, Z.; Kitayev, A.; Vineesh, T. V.; Tal–Gutelmacher, E.; Page, M.; Zitoun, D. A low–loading Ru–rich anode catalyst for high–power anion exchange membrane fuel cells. *Chem Commun (Camb)*. **2020**, 56(42), 5669–5672.
- (43) Ralbag, N.; Mann–Lahav, M.; Davydova, E. S.; Ash, U.; Galed, R.; Handl, M.; Hiesgen, R.; Magliocca, E.; Mustain, W.; He, J.; Cong, P.; Beale, A. M.; Grader, G. S.; Avnir, D.; Dekel, D. R. Composite Materials with Combined Electronic and Ionic Properties. *Matter*. **2019**, 1(4), 959–975.
- (44) Wiberg, G.; Mayrhofer, K.; Arenz, M. Investigation of the Oxygen Reduction Activity of non–Platinum Catalysts – a RDE Methodology. *ECS Transaction*. **2009**, 19, 37–46.
- (45) Lu, Y.; Chen, W. Size effect of silver nanoclusters on their catalytic activity for oxygen electro–reduction. *Journal of Power Sources*. **2012**, 197, 107–110.
- (46) Fazil, A.; Chetty, R. Synthesis and Evaluation of Carbon Nanotubes Supported Silver Catalyst for Alkaline Fuel Cell. *Electroanalysis*. **2014**, 26(11), 2380–2387.

Chapter 4. Chemical and Mechanical Surface Modification for Highly Efficient and Low-cost Hydrocarbon-based PEFCs

Note: This chapter is reproduced from the work I co-authored with Donsu Kim (co-first author, Department of Mechanical Engineering, Kookmin National University), and Ji Eon Chae (co-first author, Hydrogen Energy Technology Laboratory, Korea Institute of Energy Technology), which hasn't been published yet.

4.1. Introduction

PEMFCs have been in the spotlight as next-generation energy sources due to their high energy conversion efficiency and zero-emission operation. Over the past few decades, intensive research has been conducted to fabricate a highly efficient MEA, and as a result, the technical maturity has reached the commercialization stage. However, there are still many challenges to be solved for successful commercialization, which are the long-term stability and system cost of PEMFC.¹⁻⁴ In particular, since expensive catalysts and membranes are essential for manufacturing MEA, the capital cost of PEMFCs is not yet competitive in the market and is far below DOE's system cost target of \$30 kW⁻¹.⁵ Among the expensive materials for MEA, the perfluorosulfonic acid (PFSA) polymer is the most widely used proton conductive polymer due to its high conductivity, chemical stability, and mechanical robustness. However, the fluorinating process for fabrication of the membrane causes environmental problems and a high material cost of \$500 m⁻² or more (for commercially available Nafion® membranes), and also high gas permeability of the membrane causes chemical degradation of MEA.⁶⁻⁷

In this regard, there have been great efforts to develop membranes

that are cheaper and have superior membrane properties to commercial PFSA. Especially, non-fluorinated hydrocarbon-based polymer electrolyte membranes (HC-PEMs) have been widely studied.⁸⁻¹² These HC-PEMs are promising electrolyte materials that have several advantages such as low gas permeability, excellent thermal stability, and physical properties.¹³ Typically, HC-PEMs are based on readily available and inexpensive materials. Also, the eco-friendly synthesis process HC-PEMs have an advantage over them in terms of reducing production costs by eliminating fluorinating steps. Therefore, HC-PEM is noteworthy as the cost-effective cation exchange membranes to replace high-cost PFSA-PEM such as Nafion®, Flemion®, and Aciplex®.^{1,14} For application to PEMFCs, HC-PEM is incorporated into MEA with PFSA ionomer-containing catalyst layers (CLs). However, it causes interfacial issues between them due to poor compatibility and adhesion from the different chemical properties of HC and PFSA polymers, which eventually deteriorates the performance and durability.¹⁵

To address this issue, several efforts have been conducted to improve the compatibility between the HC-PEM and PFSA-CL chemically or mechanically. For example, chemical modification approaches such as synthesizing partially fluorinated HC-PEM¹⁶⁻¹⁸, employing HC-ionomer in CL^{15,19-20}, and introducing an interfacial

adhesion layer based on PFSA-ionomer²¹⁻²² were reported. And, Jeong et al. further developed the interface adhesion layer approach by forming the layer to have mixed HC and PFSA ionomers with gradient composition, which mixed layer brought improved interfacial bonding strength and stability between HC-PEM and PFSA-CL.²¹ When it comes to the mechanical modification approach, introducing micro-/nano-structures or roughness at the interface has been reported to achieve a mechanical fastener effect from interlocked geometry²³⁻²⁵. Recently, Oh et al. introduced solvent vapor, which partially dissolves the HC membrane, induced interface modifying method by impregnating the membrane into cathode CL. The impregnated membrane into CL enlarged the electrochemical surface area and reduced interfacial resistance.²³ However, most approaches required newly synthesized materials or complicated processes with the use of high-boiling point solvent that are not easily applicable to membrane dual-side modifying approach and need to be the post-treatment process to remove residual solvent. Therefore, a novel strategy that is easily applicable to commercially available MEA fabrication process (e.g. decal transfer method) while exhibiting their unique features that improve interface adhesion and systemic performance without the need for new substances or complicated process is highly required.

In this chapter, a mechanical and chemical combined strategy for enhancing the HC–PEM/CL interface of PEMFC was introduced using a spatially controlled oxygen plasma irradiation method. Through an oxygen plasma etching process with a polymer stencil having regular openings, micro–sized holes and oxygen functional groups were successfully introduced onto the surface of the HC membrane. The modified membrane was easily incorporated with oxygen plasma–treated electrodes by low–temperature and low–pressure decal transfer method due to enhanced interface adhesion force. By mechanical bonding and shear force measurements, it was confirmed that the micro–sized structures and the chemical functional group on the surface improved the bonding strength between HC–PEM and PFSA–CL. Also, the modified MEA showed significantly improved power density with decreased ohmic and mass transport resistances. From the analysis by applying a transmission line model, it was found that the improved bonding strength prevented exfoliation of the electrode from the membrane, and brought a reduction of ohmic and proton transport resistance at the interface. Furthermore, a detailed analysis of the limiting current density verified that the modified MEA showed remarkably reduced oxygen transport resistance within the electrode due to the micro–pillar structure induced highly porous electrode array region, which acts as an oxygen transport highway.

4.2 Experimental methods

4.2.1. Preparation of the modified samples and MEAs

Sulfonated poly(arylene ether sulfone) with 40% disulfonation (BPSH-40) (AquaforceTM, YANJIN Technology, China) was prepared for 10 wt% polymer solution in dimethylacetamide. The polymer solution was filtered with a 0.45 μm -Teflon syringe filter. The solution was cast on a glass plate and dried in a vacuum oven to remove the solvent.

The fabrication process of a polymeric stencil has been described in detail in a previous paper²⁶ and is briefly summarized here. First, to prepare a PDMS mold with micro-sized pillar arrays (diameter 20 μm), a curing agent and base (Sylgard 184 kit, Dow Corning, United States) are mixed in a weight ratio of 1:10 and poured onto the prepared silicon master with micro-sized holes (diameter 20 μm) to be cured at 80°C for 1 h. A flat PDMS mold was prepared in the same way on the flat silicon master. Next, 100 μl of UV-curable polyurethane acrylate (PUA 311RM) resin (Changsung sheet, Korea) was applied between the patterned PDMS and the flat PDMS, and the assembly was gently pressed. Then, the assembly was cured using a UV cure system (Minuta technology, Korea) for a short time of ~ 1 min with an intensity of 15 W cm^{-2} . Due to oxygen permeation

through gas permeable PDMS molds which inhibits free-radical polymerization by scavenging initiator radicals at the interface between flat and pillared structures, a thin polymeric film with a uniform 20 μm -sized aperture array was fabricated. After, the polymeric stencil was further cured for 1 h for fully curing.

To form a conformal contact with the membrane, the prepared stencil was thermally laminated on the HC membrane at a pressure of 5 Mpa at 80 $^{\circ}\text{C}$. To selectively etch the membrane, the assembly was kept in the vacuum plasma chamber (Femto Science, Korea). During the process, the pressure was kept at $\sim 4.5 \times 10^{-1}$ torr working pressure, and the oxygen flow rate of 20 sccm, frequency of 50 kHz, and power of 100 W was applied. In this study, the etching rate was carefully controlled to be 0.068~0.075 $\mu\text{m min}^{-1}$. Due to the polymeric stencil with regular openings, only the uncovered surface was etched to form a 20 μm -sized regular structure. Finally, the stencil was exfoliated, resulting in a chemically and mechanically modified hydrocarbon-based membrane (denoted as MC-HC). To prepare a chemically modified membrane (denoted as C-HC) or additionally introduce oxygen functional groups on the electrode and MC-HC, the plasma process was performed for 1 min under conditions of the working pressure of $\sim 3.2 \times 10^{-1}$, oxygen flow rate of 10 sccm, frequency of 100 kHz, and power of 100 W.

The prepared membrane (35 ± 2 μm thick) was treated with 1M sulfuric acid (H_2SO_4) solution at 80 $^\circ\text{C}$ for 2 h, washed with distilled (DI) water for 1 h, and then completely dried. For the preparation of CL, the Pt/C (46.9 wt.%, Tanaka) powder was dispersed in Nafion[®] ionomer solution (5 wt.%), isopropyl alcohol (IPA), DI water, and dipropylene glycol (DPG) with ionomer to carbon ratio of 0.8. After sufficiently dispersed by sonication, the slurry was bar-coated onto the PI film, and the catalyst loading of the anode and cathode was fixed to 0.2 mg cm^{-2} . The decal films were hot-pressed on both sides of the HC membrane at 140 $^\circ\text{C}$ for 5 min at a given pressure with an active area of 5 cm^2 . In the case of C-HC and MC-HC, the plasma treatment process was conducted on the surfaces of the electrodes and membranes before lamination. Finally, the PI film was detached from the MEA. For analysis of the decal transfer yield, the digitized image was examined using ImageJ based on the residual electrode area ratio because the weight difference in film before and after decal transfer was not large enough to quantitatively measure. After transfer, the area fraction of the electrodes that remained in the upper and lower films were examined, and their average values were given.

4.2.2. Electrochemical analysis

The prepared MEAs were sandwiched with two GDLs (Sigracet 39BB, SGL Carbon, Germany), two Teflon gaskets (CNL Energy, Korea), and two graphite plates with a serpentine-type flow field. The single-cell was assembled by fastening screws with a torque of ~ 9 N m. To evaluate the single-cell performance, a PEMFC test station (CNL Energy) and a potentiostat (BioLogic) were used. To measure polarization curves and electrochemical impedance spectroscopy (EIS) spectra, the cell temperature was set to 80 °C and fully humidified hydrogen (150 sccm) and air (800 sccm) were supplied to the anode and cathode, respectively. The polarization curves were obtained using the current sweep method with a scan rate of 50 mA cm⁻². The EIS was conducted at 0.6 V with an AC amplitude of 10 mV and a frequency range of 100 mHz to 15 kHz. To analyze catalyst utilization of MEA, cyclic voltammetry (CV) was conducted with a sweeping range of 0.05 – 1.2 V and a scan rate of 50 mV by supplying fully humidified hydrogen (50 sccm) and nitrogen (200 sccm) to the anode and cathode, respectively. The hydrogen crossover current density was measured by linear sweep voltammetry (LSV) with a sweeping range of 0.1 – 0.6 V under the condition of fully humidified hydrogen (anode, 200 sccm) and nitrogen (cathode, sccm) at anode and cathode, respectively. Under the same environment, H₂/N₂ EIS was conducted to analyze the CL

resistance of MEAs at 0.2 V with an AC amplitude of 5 mV and a frequency range of 70 mHz to 100 kHz. The limiting current measurements were performed according to the variance of oxygen concentration and gas pressure to analyze oxygen-transport resistance. The MEA fabrication procedures were consistent with the single-cell test. The high flow rate of hydrogen (1000 sccm) and nitrogen-diluted oxygen (2000 sccm) was supplied to the anode and cathode, respectively. To avoid CL flooding, the relative humidity was controlled at 69%. The current density was recorded as cell potential was decreasing from 0.4 V to 0.1 V with a 0.03 V interval and the limiting current was chosen the current density at 0.13 V. The oxygen mole concentration of 0.5, 1, 1.5, and 2 % were used, and the absolute pressure was set to 101, 151, 201, 251, and 301 kPa.

4.2.3. Physical and chemical characterization

Field emission-scanning electron microscopy (FE-SEM) (Carl Zeiss, Germany) was used to obtain the surface and cross-sectional images of the membranes and MEAs. A contact angle analyzer (KRUSS, Germany) was used to measure the static water contact angle on the membranes. To prevent swelling of the membrane, all the tested samples were hot-pressed on the flat glass substrate. A

universal testing machine (Instron, United States) was utilized to quantitatively compare the mechanical stability of the membranes and adhesion force between hydrocarbon-based membranes and PFSA membranes or CL. The stress-strain curves were measured for the Reference, C-HC, and MC-HC membranes of $1 \times 4 \text{ cm}^2$. The peel-off strength was obtained for laminates of Reference/Nafion[®] membrane, C-HC/Nafion[®] membrane, and MC-HC/Nafion[®] membrane. The prepared membranes (Reference, C-HC, and MC-HC) were laminated with Nafion[®] 212 ($\sim 50 \text{ }\mu\text{m}$, Dupont, United States) membrane at 10 MPa at $140 \text{ }^\circ\text{C}$ for 10 min, and the laminated area was controlled to $2 \times 2 \text{ cm}^2$. The shear stress strength was obtained for laminates of Reference/CL/Nafion[®] membrane, C-HC/CL/Nafion[®] membrane, and MC-HC/CL/Nafion[®] membrane. The catalyst slurry was prepared by mixing Pt/C catalyst powder, Nafion[®] ionomer, and IPA, which was sprayed onto the surface of the Nafion[®] membrane. Finally, the prepared CL/Nafion[®] membrane was laminated with the prepared HC membrane under the same conditions as the peel-off test. When preparing the adhesion tests samples, both the Nafion[®] membrane and CL/Nafion[®] membrane being attached to the plasma-treated C-HC and MC-HC PEMs were subjected to short-plasma treatment before bonding. The water uptake and swelling ratio were determined in acid forms. All membranes were dried and then the

weight (W_{dry}), length (l_{dry}), and thickness (t_{dry}) of the dry membrane were measured. The membranes were immersed in deionized water for two days at 30 and 80 ° C. After water immersion, the membranes were removed and wiped lightly. The weight (W_{wet}), length (l_{dry}), and thickness (t_{dry}) of the swollen membrane were also recorded. The water uptake and swelling ratio were calculated as follows:

$$\text{Water uptake (\%)} = \frac{(W_{wet} - W_{dry})}{W_{dry}} \times 100$$

$$\text{Swelling ratio, } \Delta l = \frac{l_{wet} - l_{dry}}{l_{dry}} \times 100$$

$$\text{Swelling ratio, } \Delta t = \frac{t_{wet} - t_{dry}}{t_{dry}} \times 100$$

The proton conductivity of the membrane was measured using the four-probe EIS. The membrane was prepared in size of 1×4 cm², and then inserted into the conductivity cell with four Pt wire electrodes at a distance of 1 cm for each electrode. EIS measurement was conducted under the constant current of 0.1 mA with an amplitude of 0.01 mA over the frequency ranges from 1 MHz to 1 Hz by supplying fully humidified nitrogen gas at 70 °C. In-plane conductivities of membranes were calculated from the measured EIS resistance and the following equation.

$$\sigma = \frac{L}{RA}$$

In the above formula, L (cm), R (Ω), and A (cm²) represent the distance between the electrodes, the resistance of the membrane, and the cross-sectional area of the membrane, respectively. The chemical states of the membranes were examined by X-ray photoelectron spectroscopy (XPS) (Kratos, United Kingdom).

4.3. Results and discussion

4.3.1. Chemical and mechanical modification and membrane characterization

Figure 4.1 a illustrates the fabrication process of a selectively plasma-etched membrane and MEA using a decal transfer method. First, a thin polymeric stencil with 20 μm -sized holes was prepared using PDMS with micro-pillar arrays, flat PDMS, and UV-curable polymer resin (fabrication details are explained in the Experimental methods and **Figure 4.2**). Then, the two polymeric stencils were attached to both sides of the HC-PEM and the oxygen plasma etching process was conducted. The etching was conducted only on the exposed surface of the HC-PEM, resulting in micro-sized holes and nano-sized roughness. The depth of the etched hole was carefully controlled by adjusting the etching time, and the linear relation between the etching time and etched depth profile was shown in **Figure 4.3**. In this study, the optimized etching depth was selected as $\sim 4.5 \mu\text{m}$ by considering the transferred electrode thickness. This plasma etching process was sequentially performed on each side surface, and then, the polymeric stencils were delaminated. After geometric modification, a short time ($\sim 1 \text{ min}$) plasma treatment was further conducted on the entire surface of the modified membrane to

introduce the oxygen functional groups on the surface of the HC-PEM including the intact surface. This process lets the membrane have high surface energy and create binding sites. Next, to fabricate MEAs with improved interface adhesion between the modified HC-PEM and the CL, a decal transfer process was conducted by locating the modified HC-PEM between the short-time plasma-treated two CL/PI films under 140 °C at a given pressure. After, the PI films were carefully detached from the membrane and, finally, the MEA with modified HC-PEM was prepared. (**Figure 4.1 b**)

To analyze the oxygen plasma effects mechanically and chemically on the HC-PEM surface, the pristine HC-PEM and the modified HC-PEMs with plasma treatment with/without etching were prepared. **Figure 4.4 a-c** shows cross-sectional SEM images of the reference PEM (BPSH-40, the chemical structure is described in **Figure 4.5**), chemically modified HC (C-HC) PEM by short-time plasma treatment, and mechanically and chemically modified HC (MC-HC) PEM with etching thickness of $\sim 4.5 \mu\text{m}$ with pattern diameter of $20 \mu\text{m}$. While the reference and plasma-treated membrane show a flat surface without geometrical modification, the plasma-etched membrane shows micro-sized holes with nano-sized roughness in the etched region. To confirm the change of chemical states on the surface of the HC-PEMs by introducing an oxygen functional group

(eg. hydroxyl, carbonyl, carboxyl, etc.), XPS spectra were obtained. **Figure 4.4 d** shows wide-scan XPS spectra of reference, plasma-treated without etching, and plasma etched HC-PEMs. Compared to the reference, the plasma-treated HC-PEMs showed an increase in the atomic ratio of oxygen (26.19 and 33.99 at.%, for without etching and with etching, respectively), suggesting that oxygen functional groups were introduced on the membrane surface through oxygen plasma treatment, and etching process can be helpful to introduce further oxygen functional group by enlarging surface area due to increased micro-/nano-roughness. For the deeper analysis, the C1s spectra were deconvoluted for the reference, and the modified HC-PEMs. As shown in **Figure 4.4 e**, the modified membranes with plasma showed a distinct increase in carboxyl (–COOH) and hydroxyl (–OH) signals.^{27–29} These results show that oxygen functional groups containing hydroxyl and carboxyl groups were introduced to the membrane surface and the membrane surface was chemically activated with high surface energy via plasma treatment, which was consistent with the dramatic decrement of contact angle values of 79.5 °, 17.8 °, and 4.9 ° for the reference, C-HC, and MC-HC PEMs, respectively (**Figure 4.6**). Before analyzing the effect of plasma treatment on the adhesive property and single-cell performance of the MEAs, membrane basic properties of pristine and

modified HC-PEMS were investigated through performing proton conductivity measurement and mechanical tensile test. **Figure 4.4 f** shows the comparison of proton conductivity and **Table 4.1** summarized the values of water uptake and swelling ratio (i.e. dimensional stability) for the reference, C-HC, and MC-HC PEMs, respectively.

Overall, samples prepared by the plasma process (C-HC and MC-HC) showed an increase in the water uptake and dimensional swelling in the through-plane direction, and a little decrease in dimensional swelling in the in-plane direction. Also, from the comparable proton conductivities of the pristine and the modified HC-PEMs, we can see that the surface modification with plasma process to the HC-PEMs does not significantly affect the ion transporting properties of the membrane. In addition, from the measured mechanical properties of the membrane as shown in **Figure 4.7**, the reference and C-HC PEMS show almost similar ultimate tensile strength, Young' s modulus, and elongation at break. On the other hand, MC-HC PEM showed a slight increase in Young' s modulus and a decrease in elongation at break, which may be due to polymer hardening by plasma treatment and stress concentration at the edges of the micro-sized structures.

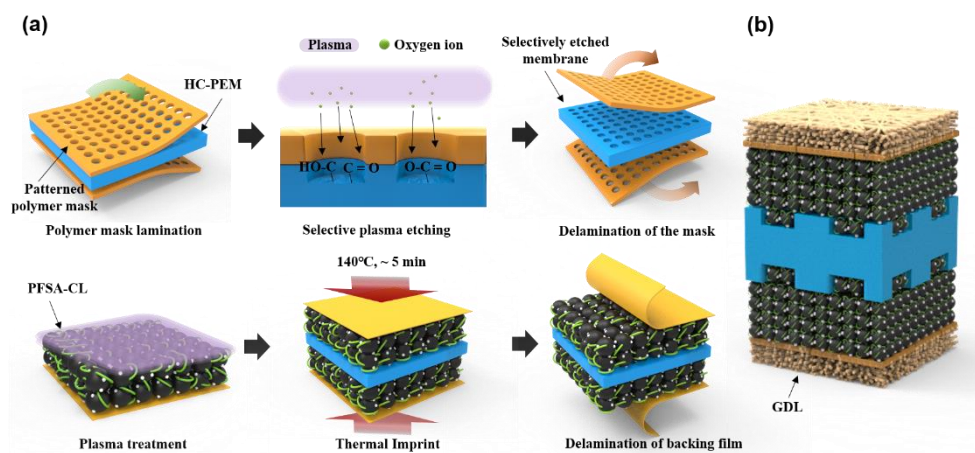


Figure 4.1. (a) Schematic diagram of spatially controlled oxygen plasma irradiation process of HC-PEM and decal transfer process. (b) Schematic of MEA with the modified HC-PEM

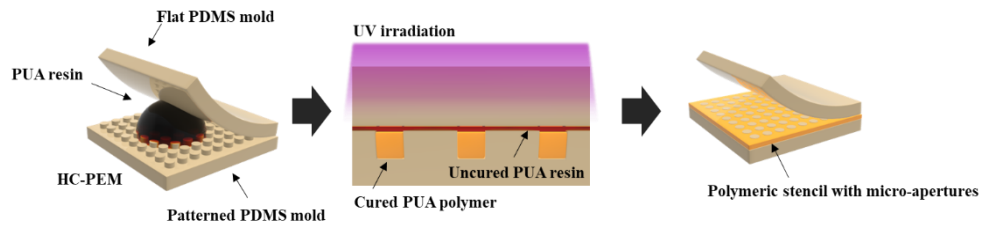


Figure 4.2. Schematic diagram of fabrication process of polymeric stencil with micro-apertures

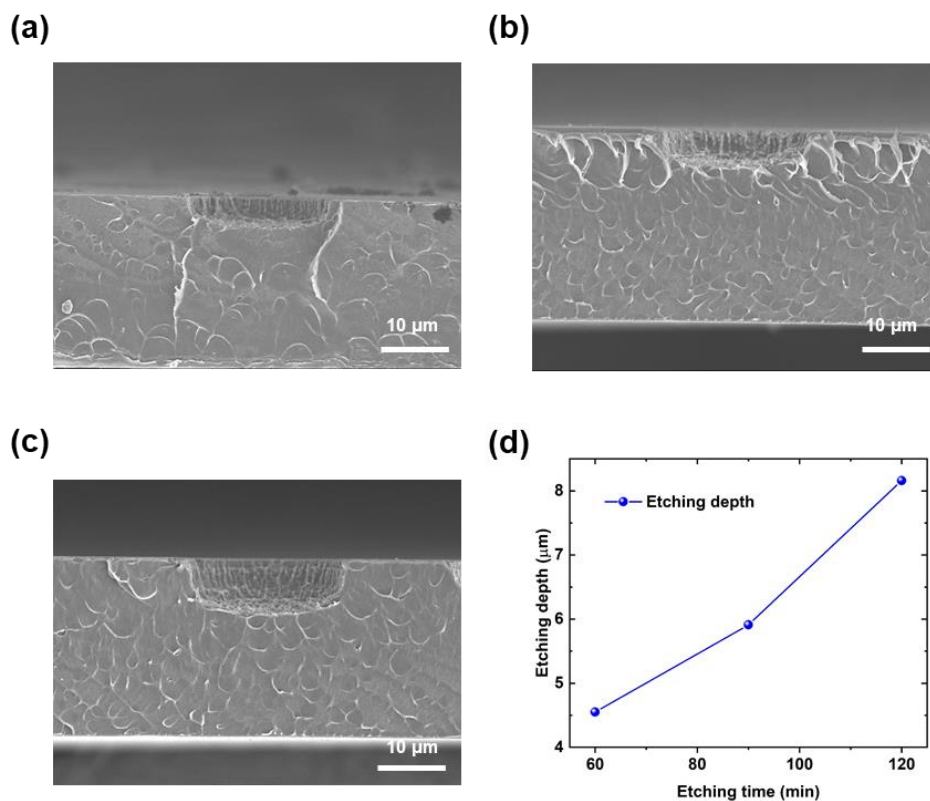


Figure 4.3. (a–c) SEM images of plasma etched BPSH–40 membrane for (a) 60 min, (b) 90 min, (c) 120 min, and (d) the etching depth of BPSH–40 according to the etching time.

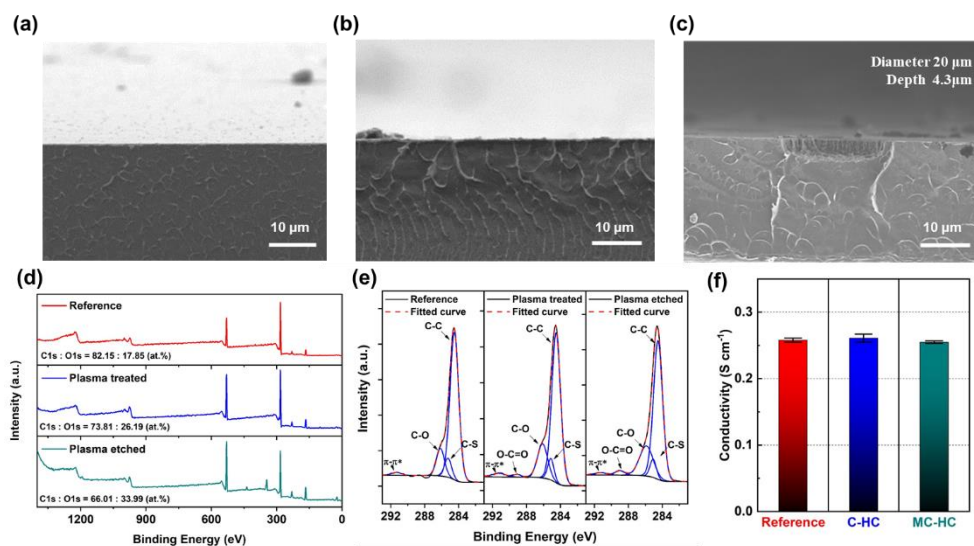


Figure 4.4. Cross-sectional SEM images of (a) Reference, (b) C-HC, and (c) MC-HC. (d) Wide-scan XPS spectra and C1s spectra of reference, plasma-treated HC-PEM, and plasma-etched HC-PEM. (f) Proton conductivity of reference, C-HC, and MC-HC.

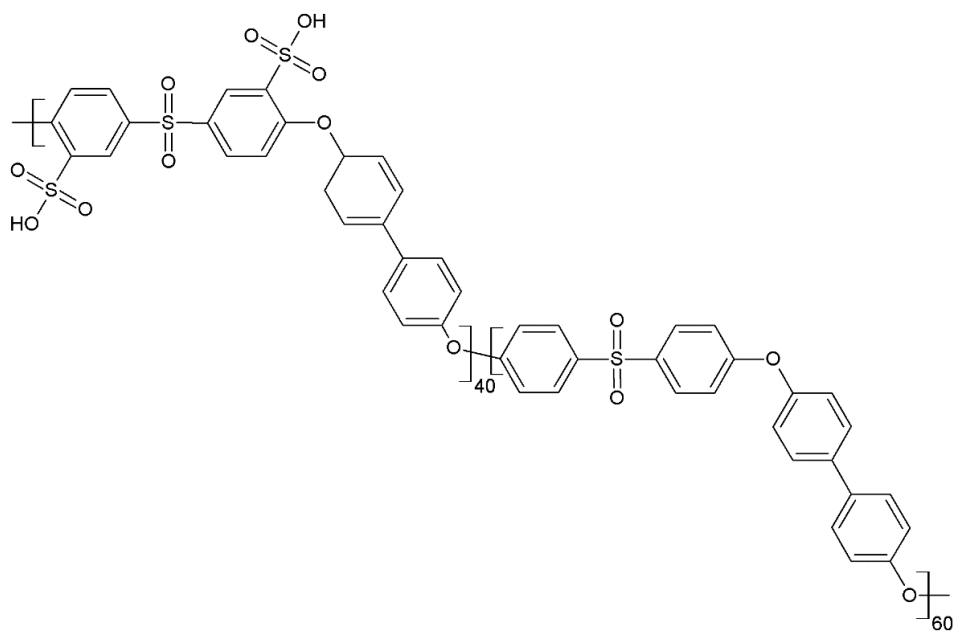


Figure 4.5. Chemical structure of BPSH-40.

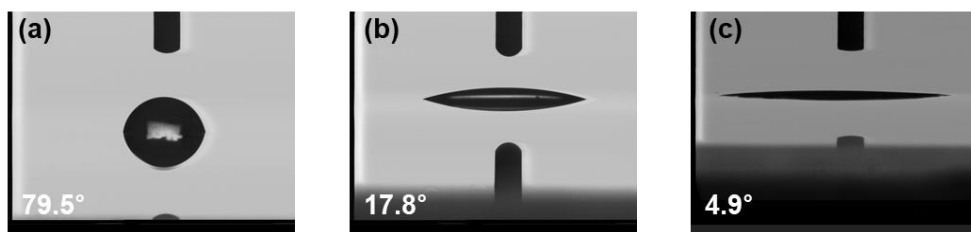
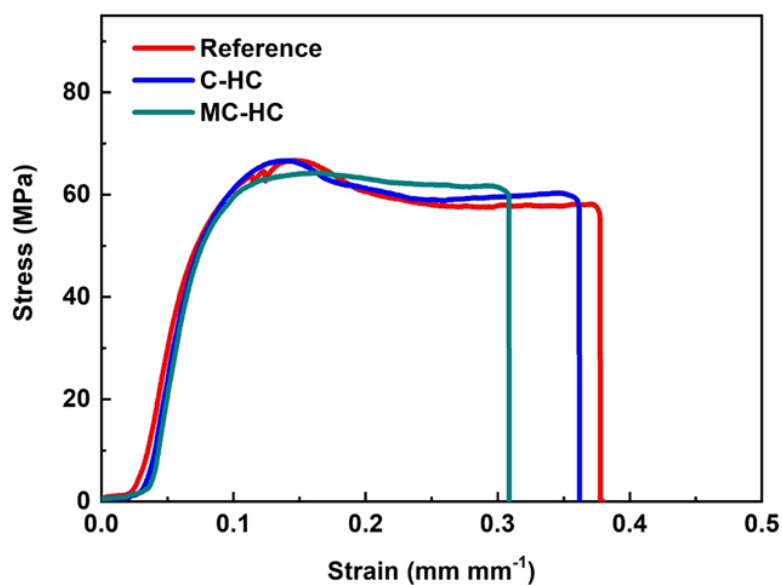


Figure 4.6. Water contact angle on the (a) reference, (b) C-HC, and (c) MC-HC PEM.



Samples	Ultimate tensile strength (MPa)	Young's modulus(GPa)	Elongation at break (%)
Reference	66.77	1.41	37.7
C-HC	66.68	1.45	36.1
MC-HC	65.70	1.483	30.8

Figure 4.7. Stress–strain curves of the reference, C–HC, and MC–HC PEM.

Samples	Water Uptake		Swelling Ratio (%)			
	(weight%)		Δl		Δt	
	30 °C	80 °C	30 °C	80 °C	30 °C	80 °C
Reference	38.1 \pm 1	45.1 \pm 1.6	17.1 \pm 1.4	21.7 \pm 2.5	19.1 \pm 2.1	22.7 \pm 0.8
C-HC	44.5 \pm 1.9	54.5 \pm 2.2	16.7 \pm 2.2	22 \pm 1.2	21 \pm 2.2	25.3 \pm 3.3
MC-HC	44.9 \pm 3.5	55.2 \pm 2.1	16.7 \pm 2.3	20.2 \pm 1.7	21.4 \pm 2.2	26.3 \pm 2.9

Table 4.1. Water uptake and swelling ratio of reference, C–HC, and MC–HC PEM.

4.3.2. Analysis of the improved interfacial adhesion

Next, to quantitatively compare the adhesion enhancement of the plasma modified-HC with PFSA ionomer, two experiments; 1) T-peel test for laminates of Reference/Nafion[®], C-HC/Nafion[®], and MCHM/Nafion[®]; 2) Shear stress measurement for laminates of reference/ CL, C-HC/CL, and MC-HC/CL were conducted. As shown in **Figure 4.8 a**, the T-peel test was performed by pulling the two membranes of HC membrane and commercial PFSA membrane (Nafion[®] 212) in the opposite direction perpendicular to the laminates like a T-shape. The strength was defined as the measured force normalized by the width of the laminates and displayed in **Figure 4.8 b**. Except for a sudden increase at the beginning and the end of the test, the differences in average peel-off strength were notably observed among the samples. While the Reference/Nafion[®] showed a peeling strength of 5.5 mN mm^{-1} , C-HC/Nafion[®] and MC-HC/Nafion[®] showed increased strength of 16.95 mN mm^{-1} (~308% of the reference) and 32.53 mN mm^{-1} (~591% of the reference), respectively. The higher adhesion strength of the laminates with C-HC/Nafion[®] than the reference/Nafion[®] can be inferred from the strong adhesion bonding at the interface due to oxygen functional group (e.g. $-\text{COOH}$, $-\text{OH}$) induced hydrogen bonding and/or chemical bonding with condensation reaction.^{27,30-31} Furthermore, it

was confirmed that the laminates of MC–HC/Nafion[®] can have further enhanced adhesion properties due to both the chemical effect of generating more oxygen functional groups and the mechanical fastener effect from micro–hole array patterned geometry. Interestingly, by performing XPS measurements with the pristine and modified HC membranes from the samples after T–peel tests, it was found that a strong F peak appeared on the surface of the MC–HC as shown in **Figure 4.8 c**. This cohesion failure was caused at the interface between MC–HC and Nafion[®] membrane (containing F component), which signifies that strong bonding adhesion between the MC–HC and the Nafion[®] was formed. To evaluate the interface bonding strength in the case of porous CL, as illustrated in **Figure 4.8 d**, the shear stress was measured by holding the two membranes (HC membrane and CL coated Nafion[®] membrane) on different sides and pulling them in the opposite direction. **Figure 4.8 e** shows the maximum shear stress of the prepared laminates. While the reference/CL showed maximum shear stress of ~0.1 MPa, C–HC/CL (0.144 MPa), and MC–HC/CL (0.174 MPa) showed ~43% and ~74% increased shear stress, respectively. In addition, as shown by the digital camera image after shear stress measurements (**Figure 4.8 f**), unlike the reference where the interface between HC membrane and CL was neatly peeled off after the test, residual CLs attached to the

C-HC and MC-HC surface were clearly observed. This result is similar to the previously observed T-peel test, which means that the plasma-modified HC-PEM can improve adhesion between not only the PFSA membrane but also the porous CL containing PFSA. And this can bring important meanings when applying the decal transfer method and analyzing the resistances within the MEAs. When it comes to the decal transfer method with HC-PEMs, it requires a much higher temperature and/or pressure compared to that of the PFSA-based PEM due to its high glass transition temperature (PFSA $\sim 120\text{ }^{\circ}\text{C}$ and HC $> 200\text{ }^{\circ}\text{C}$)³²⁻³⁴, high rigidity, and low compatibility with CL containing PFSA ionomer. Therefore, performing the decal transfer method at low pressure and temperature by employing enhanced interfacial bonding properties can be helpful to archives advantages in the MEA manufacturing process as well as high-performance PEMFC with low-cost HC-PEM.

Figure 4.9 a shows catalyst transfer yield according to the variance of lamination pressures for the reference, C-HC, and MC-HC PEMs, and its corresponding digital images of the resulting MEAs and PI films after delamination were displayed in **Figure 4.9 b**. The reference, which had the weakest bonding adhesion force between the membrane and the electrode among the samples, exhibited a lower transfer rate of 83.6% at 10 MPa, 91.1% at 20 MPa, and completely

transferred at 30 MPa. On the other hand, the C-HC showed a transfer rate of 93.7% at 10 MPa and was completely transferred at 20 MPa. In the case of the MC-HC was completely transferred even at 10 MPa due to the strongest bonding adhesion strength through the plasma etching process, which induced chemically activated high-energy surface and micro-hole array geometry.

For evaluating the electrochemical performances of the reference, C-HC, and MC-HC PEMs, the MEAs were fabricated under each optimized decal transfer condition where the constant temperature of 140 °C with different applying pressures of 30 MPa, 20 MPa, and 10 MPa for reference, C-HC, and MC-HC, respectively.

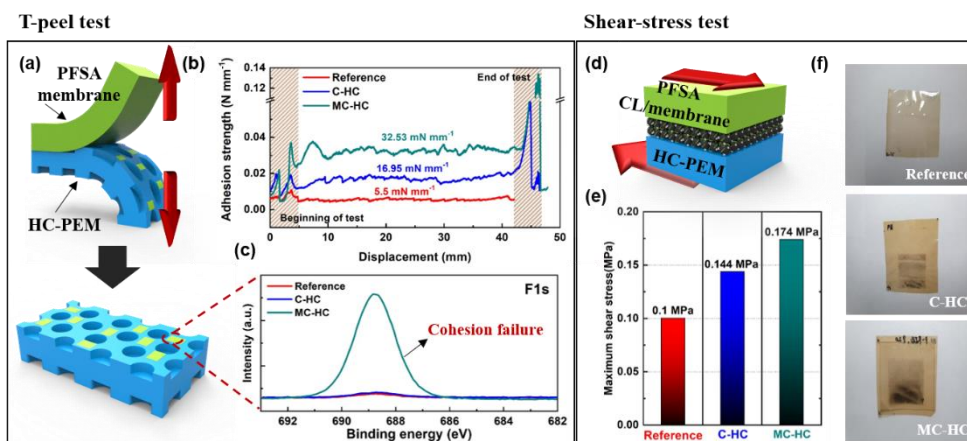


Figure 4.8. (a) Schematic of T-peel test, (b) Peel-off strength between the PFSA membrane (Nafion) and the HC-PEMs, and (c) F1s spectra on the delaminated surface for reference, C-HC, and MC-HC. (d) Schematic of the shear-stress test, (e) Maximum shear stress between the PFSA electrode and the HC-PEM, and (f) Digital images of the HC-PEM after testing.

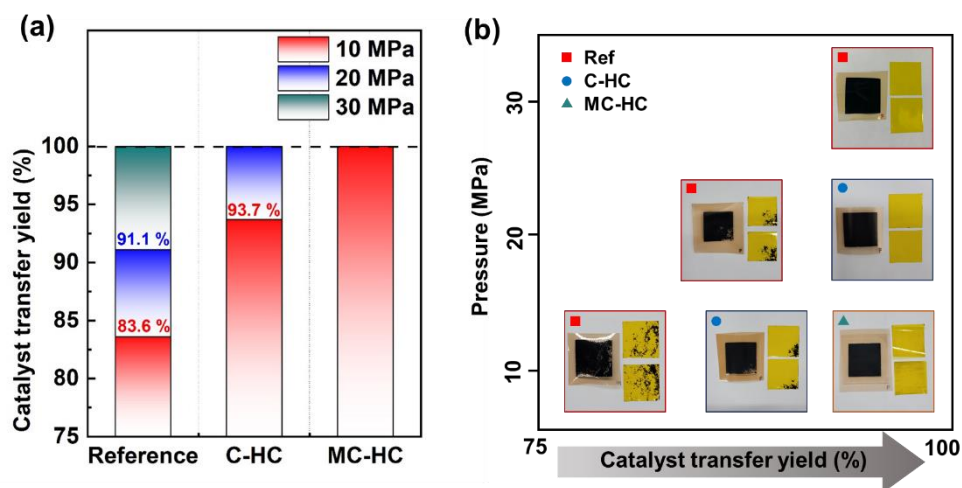


Figure 4.9. (a) Catalyst transfer yield according to the decal pressure for reference, C-HC, and MC-HC. (b) Digital images of the fabricated MEA and residue decal films.

4.3.3. Evaluation of the electrochemical characterization

Figure 4.10 a shows the polarization curves at 80 °C under the fully humidified condition with supplying H₂(150 sccm)/Air (800 sccm), respectively. Compared to the peak power density (PPD) of the reference MEA (450 mW cm⁻²), the modified MEAs with C-HC and MC-HC PEMs exhibited much higher PPDs of 504 mW cm⁻² and 606 mW cm⁻², which values were increased by 12.0% and 34.7%, respectively. And from the EIS spectra under the same operating condition at 0.6V as shown in **Figure 4.10 b**, the smallest R_{LF-HF}, which can be calculated from the semi-circle radius and signifies the combined contribution of the charge-transfer resistance and mass-transport resistance at a high current density region, was observed for the MEA with MC-HC (0.399 Ω cm²) compared to that of the MEAs with reference (0.902 Ω cm²) and C-HC (0.552 Ω cm²). By considering the fact that all MEAs used the same electrode and there is no difference between catalyst and ionomer, this difference can be ascribed to the plasma-induced improved interfacial properties at the membrane/electrode interface as well as modified electrode structure due to micro-hole patterns and different applying pressure during decal process. For a more detailed analysis, EIS spectra were measured under H₂/N₂ atmosphere and a transmission line model was applied to interpret the results.^{24,35-37} From the response of

impedance, an ohmic resistance from the cell elements (R_0) and a protonic resistance across the catalyst layer (R_{CL}) can be defined. Since there is a deviation between the ideal model and the actual spectra, the value of R_0 is defined as the intercept value of the spectrum and the x-axis in this study. As shown in **Figure 4.10 c**, the values of R_0 and R_{cl} decrease in the order of the MEAs with reference, C-HC, and MC-HC. Compared to the MEA with reference ($0.0598 \Omega \text{ cm}^2$), MEAs with C-HC ($0.0573 \Omega \text{ cm}^2$) and MC-HC ($0.0547 \Omega \text{ cm}^2$) showed $\sim 4.2 \%$ and $\sim 8.5 \%$ decreased R_0 . Since reference and C-HC had the same membrane thickness, it can be inferred that the decrease in R_0 was due to a decrease in interface resistance between the membrane and the CL. Additionally, the etching process-induced locally thinned membrane thickness of the MC-HC further reduced R_0 . In the case of the MEA with MC-HC having a locally shortened path region, slightly increased hydrogen crossover density was observed as exhibited in **Figure 4.11**, however, this value is still much smaller than that of a thick Nafion[®] 212 membrane (e.g. $50 \mu\text{m}$ thickness). Notably, from the cross-sectional SEM images for the prepared MEAs, different morphological features of the membrane, the CL, and their interface are clearly observed (**Figure 4.10 d**). When it comes to the MEA with reference PEM, severe delamination problem at the interface between the membrane and the CL and

noticeable PFSA–ionomer (Nafion®) skin layer on the outer surface of the CL were observed. Therefore, it is clear that the delamination, due to low adhesion strength at the interface, results in an increase in R_0 . Moreover, the MEA with reference ($0.0822 \, \Omega \, \text{cm}^2$) showed significantly increased R_{CL} compared to the MEAs with the modified membranes ($0.051, 0.0306 \, \Omega \, \text{cm}^2$ for MEA with C–HC and MC–HC, respectively). From this result, it can be found that the delamination at the interface restricted the proton transport to CL, which causes an increase and the inhomogeneity of R_{CL} .^{24,37} On the other hand, both the MEAs with C–HC and MC–HC had tightly bonded interfaces due to plasma–induced improved bonding adhesion forces and therefore, showed much lower R_{CL} and R_0 (detailed values are summarized in **Table 4.2**).

Especially, for the MEA with MC–HC, the CL layer is conformally formed along the shape of the MC–HC by completely filling the micro–sized holes. This enlarged interfacial contact area provides extended proton transport pathways, and improved compatibility between the HC–PEM and the CL, and lower laminating pressure results in better uniform ionomer distribution in the CLs compared to the reference MEA. Next, by comparing the electrochemical active surface areas (ECSAs) of each MEAs, the CV spectra were obtained (**Figure 4.12**) and the calculated ECSA values were summarized in

Table 4.2. The ECSA of MEA with reference PEM was $36.23 \text{ m}^2\text{g}^{-1}_{\text{pt}}$ while the MEAs with C-HC and MC-HC showed a slightly increased by $\sim 2.6\%$ ($37.14 \text{ m}^2\text{g}^{-1}_{\text{pt}}$) and $\sim 4.4\%$ ($37.84 \text{ m}^2\text{g}^{-1}_{\text{pt}}$), respectively. This increase was caused by the conformal contact between the membrane and electrode, and enlarged surface area due to the micro- and nano-sized structure, but the differences were not large enough to affect the MEA performance.

After observing the I-V characteristics and the effect of reducing the protonic resistance with modified MEAs, limiting the current density of each MEAs was measured by using diluted oxygen gases and controlling back-pressures to analyze the significant reduction in the mass transfer resistance ($R_{\text{LF-HF}}$) which exhibited the greatest effect on the performance. The total oxygen transport resistance (R_t) can be calculated by the following equation:³⁸⁻⁴⁰

$$R_t = 4F \frac{X_{O_2}}{j_{lim}} \frac{P - P_W}{RT}$$

In the above equation, F stands for faraday number, X_{O_2} is oxygen mole fraction, j_{lim} is limiting current density, P and P_W are total gas pressure and water vapor pressure, R is gas constant, and T is cell temperature. **Figure 4.13** shows the limiting current density for each mole fraction of oxygen and total gas pressure for the samples with reference, C-HC, and MC-HC. To obtain the ratio of X_{O_2} and the

j_{lim} (i.e. slope), the regression straight line passing through the origin was fitted for each pressure. Then, the linear relationship between total oxygen transport resistance and total gas pressure can be graphically represented as shown in **Figure 4.14 a**. From the graph, the contribution of pressure-dependent (R_P , at channel and GDL) and pressure-independent (R_{NP} , at CL and ionomer film) oxygen transport resistance to R_t can be separately obtained through a linear trend line of R_t . The calculated R_P and R_{NP} for the prepared samples are depicted in **Figure 4.14 b**. As the same flow channels and GDLs were used, all of samples showed similar R_P values, which are affected by the flow channel geometry and macro-pores distribution of GDL. However, in the case of R_{NP} , the samples with C-HC and MC-HC show 33% and 65.23% decreased values compared to that of the reference of 45.214 s m^{-1} . To figure out the reason for reduced oxygen transport resistance in the CL, morphological characteristics of the CLs for each MEA were analyzed by SEM measurement (**Figure 4.14 c**). In the case of the CL on the reference PEM, a serious Nafion skin layer was observed on the surface of the CL, where the CL and GDL contact each other, therefore, this cause the restriction of the oxygen transport to the CL. It was also observed in the cross-sectional image of the CL as already mentioned in **Figure 4.10 d**. However, in the case of C-HC, the formation of the Nafion[®] skin layer

was alleviated. This suggests that a decrease in decal pressure is the reason for the reduction of the Nafion skin layer outside CL.⁴¹ Here, it is important to note that in the case of MC–HC, together with alleviation of the Nafion® skin layer, furthermore, it can be seen that a highly porous area was formed along the micro–sized holes array region. This highly–porous patterned region can provide oxygen transport highway into the CL and, therefore, a significant decrease in oxygen transfer resistance induced improved mass transport capacity for the MEA with MC–HC can be explained. The effect of this oxygen plasma mediated micro–structured HC PEM for improving mass transport is shown as a schematic in **Figure 4.14 d**.

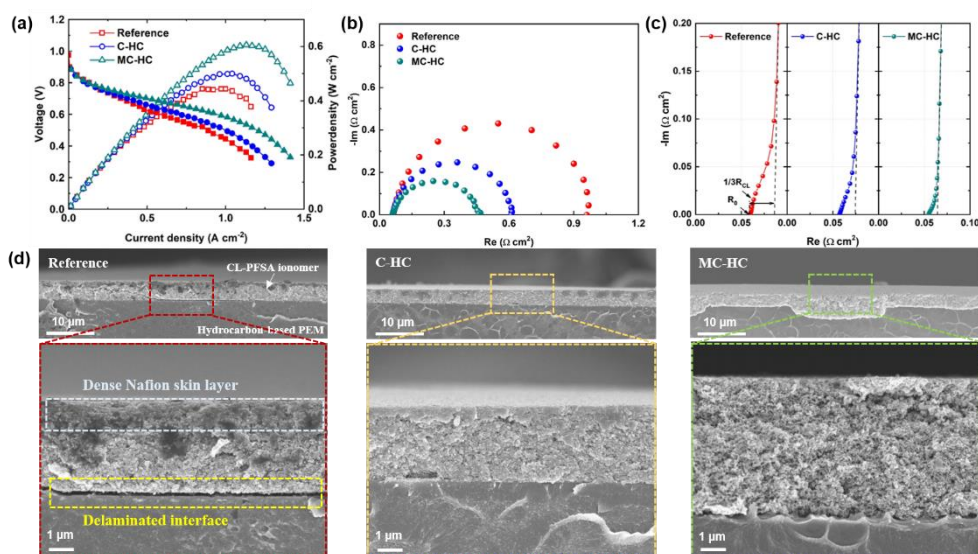


Figure 4.10. (a) Polarization curves at 80°C with supplying fully humidified H_2 (150 sccm)/air (800 sccm) without back-pressure. (b) Corresponding EIS spectra at 0.6 V for the MEAs with reference, C-HC, and MC-HC. (c) EIS spectra obtained in H_2/N_2 feed at 0.2 V. (d) Cross-sectional SEM images of the MEAs with reference, C-HC, and MC-HC.

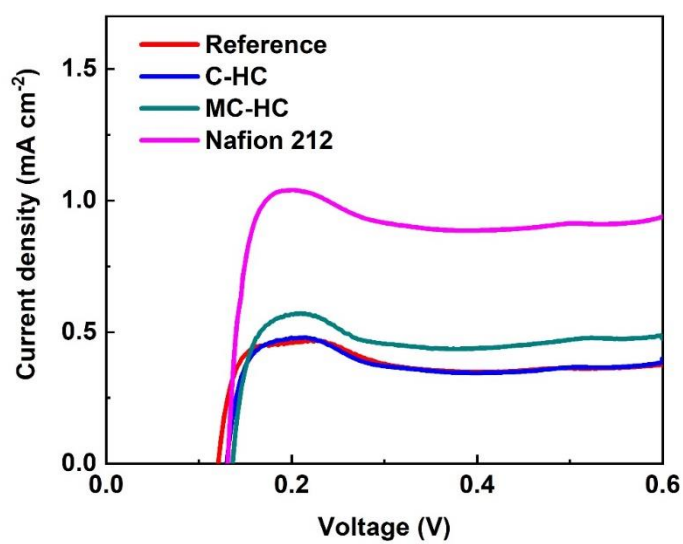


Figure 4.11. LSV spectra for the MEAs with Nafion 212, pristine and modified HC-PEMs.

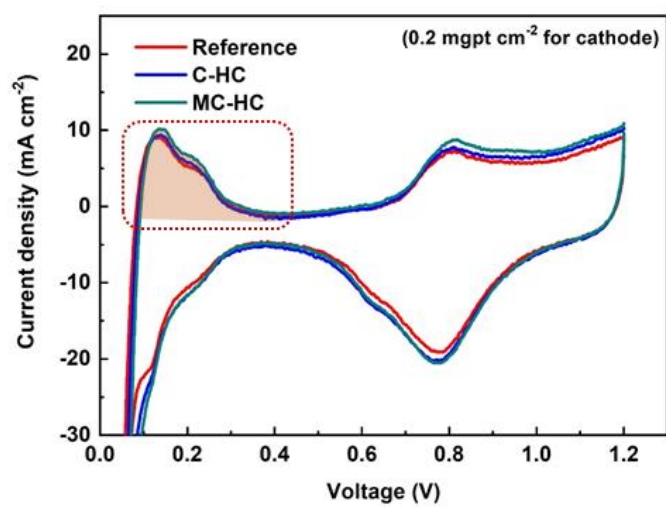


Figure 4.12. CV spectra for the MEAs with the reference, C-HC, and MC-HC PEMs.

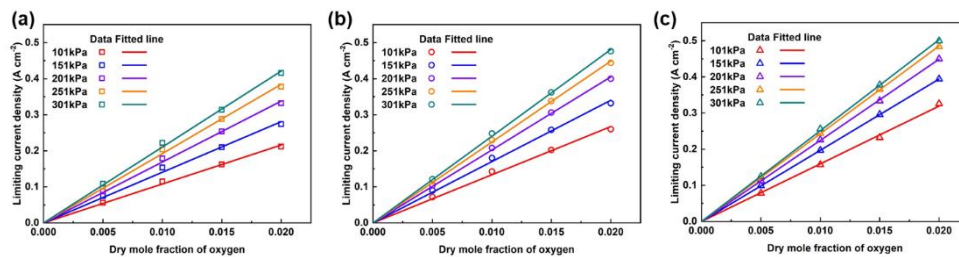


Figure 4.13. Limiting current densities of the (a) reference, (b) C-HC, and (c) MC-HC according to the oxygen mole fraction and pressure.

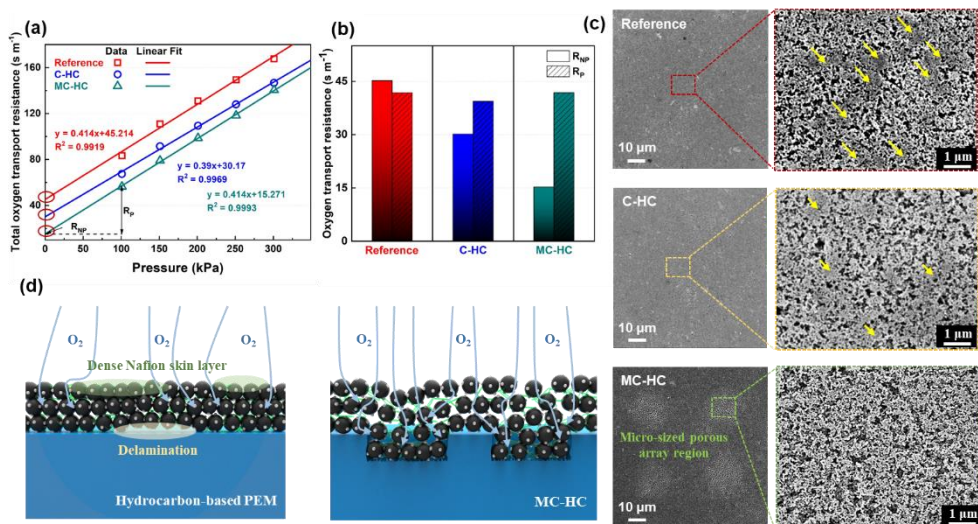


Figure 4.14. (a) Total oxygen transport resistance of MEA with reference, C-HC, and MC-HC according to the pressure (b) Pressure-independent oxygen transport resistance and pressure-dependent oxygen transport resistance (at 101kPa) obtained from Figure 6a. (c) Surface SEM images of MEA with reference, C-HC, and MC-HC. (d) Schematic illustrations of MEAs with pristine and MC-HC PEM.

Samples	Polarization curve	EIS (H ₂ /N ₂ , @0.2 V)		EIS (H ₂ /Air, @0.6 V)	CV
	Peak power density (mW cm ⁻²)	R ₀ (Ω cm ²)	R _{CL} (Ω cm ²)	R _{L,F-HF} (Ω cm ²)	ECSA (m ² g _{pt} ⁻¹)
Reference	450	0.05979	0.0822	0.9018	36.229
C-HC	504	0.05732	0.051	0.5519	37.135
MC-HC	606	0.05471	0.0306	0.3989	37.839

Table 4.2. Summary of key parameters from I–V curves and EIS spectra.

4.4. Conclusion

In summary, a mechanical and chemical modification technique for a hydrocarbon-based membrane (HC membrane) was proposed to improve both interface adhesion and mass transport capacity in PEMFC. Through an oxygen plasma process with a polymer stencil having regular openings, micro-sized holes and oxygen functional groups were successfully introduced onto the surface of the HC membrane. This modified HC membrane enabled low pressure and temperature decal transfer and results in a highly-porous patterned electrode region that can provide an oxygen transport highway. By taking these advantages, the MEA with a modified HC membrane exhibited much higher PEMFC performance compared to the reference MEA. The physical, chemical and electrochemical characteristics of the modified HC membrane and the MEA were extensively investigated.

4.5. References

- (1) Yee, R. S. L.; Rozendal, R. A.; Zhang, K.; Ladewig, B. P. Cost Effective Cation Exchange Membranes: A Review. *Chemical Engineering Research and Design* **2012**, *90* (7), 950–959.
- (2) Nguyen, H. L.; Han, J.; Nguyen, X. L.; Yu, S.; Goo, Y.-M.; Le, D. D. Review of the Durability of Polymer Electrolyte Membrane Fuel Cell in Long-Term Operation: Main Influencing Parameters and Testing Protocols. *Energies* **2021**, *14* (13).
- (3) Wang, L.; Wan, X.; Liu, S.; Xu, L.; Shui, J. Fe-N-C Catalysts for Pemfc: Progress Towards the Commercial Application under Doe Reference. *Journal of Energy Chemistry* **2019**, *39*, 77–87.
- (4) Zatoń, M.; Rozière, J.; Jones, D. J. Current Understanding of Chemical Degradation Mechanisms of Perfluorosulfonic Acid Membranes and Their Mitigation Strategies: A Review. *Sustain. Energ. Fuels* **2017**, *1* (3), 409–438.
- (5) Du, S. Recent Advances in Electrode Design Based on One-Dimensional Nanostructure Arrays for Proton Exchange Membrane Fuel Cell Applications. *Engineering* **2021**, *7* (1), 33–49.
- (6) Ahmad, S.; Nawaz, T.; Ali, A.; Orhan, M. F.; Samreen, A.; Kannan, A. M. An Overview of Proton Exchange Membranes for

- Fuel Cells: Materials and Manufacturing. *Int. J. Hydrog. Energy* **2022**, *47* (44), 19086–19131.
- (7) Rui, Z.; Liu, J. Understanding of Free Radical Scavengers Used in Highly Durable Proton Exchange Membranes. *Progress in Natural Science: Materials International* **2020**, *30* (6), 732–742.
- (8) Kim, K.; Heo, P.; Hwang, W.; Baik, J. H.; Sung, Y. E.; Lee, J. C. Cross-Linked Sulfonated Poly(Arylene Ether Sulfone) Containing a Flexible and Hydrophobic Bishydroxy Perfluoropolyether Cross-Linker for High-Performance Proton Exchange Membrane. *ACS Appl. Mater. Interfaces* **2018**, *10* (26), 21788–21793.
- (9) Kumar, A. G.; Singh, A.; Komber, H.; Voit, B.; Tiwari, B. R.; Noori, M. T.; Ghangrekar, M. M.; Banerjee, S. Novel Sulfonated Co-Poly(Ether Imide)S Containing Trifluoromethyl, Fluorenyl and Hydroxyl Groups for Enhanced Proton Exchange Membrane Properties: Application in Microbial Fuel Cell. *ACS Appl. Mater. Interfaces* **2018**, *10* (17), 14803–14817.
- (10) Wang, L.; Deng, N.; Wang, G.; Ju, J.; Cheng, B.; Kang, W. Constructing Amino-Functionalized Flower-Like Metal-Organic Framework Nanofibers in Sulfonated Poly(Ether Sulfone) Proton Exchange Membrane for Simultaneously Enhancing Interface

- Compatibility and Proton Conduction. *ACS Appl. Mater. Interfaces* **2019**, *11* (43), 39979–39990.
- (11) Parnian, M. J.; Rowshanzamir, S.; Prasad, A. K.; Advani, S. G. High Durability Sulfonated Poly (Ether Ether ketone)–Ceria Nanocomposite Membranes for Proton Exchange Membrane Fuel Cell Applications. *J. Membr. Sci.* **2018**, *556*, 12–22.
- (12) Date, B.; Han, J.; Park, S.; Park, E. J.; Shin, D.; Ryu, C. Y.; Bae, C. Synthesis and Morphology Study of Sebs Triblock Copolymers Functionalized with Sulfonate and Phosphonate Groups for Proton Exchange Membrane Fuel Cells. *Macromolecules* **2018**, *51* (3), 1020–1030.
- (13) Higashihara, T.; Matsumoto, K.; Ueda, M. Sulfonated Aromatic Hydrocarbon Polymers as Proton Exchange Membranes for Fuel Cells. *Polymer* **2009**, *50* (23), 5341–5357.
- (14) Zhu, H. Speek Scaling Up. *Joule* **2022**, *6* (4), 718–720.
- (15) Pu, X.; Duan, Y.; Li, J.; Ru, C.; Zhao, C. Understanding of Hydrocarbon Ionomers in Catalyst Layers for Enhancing the Performance and Durability of Proton Exchange Membrane Fuel Cells. *J. Power Sources* **2021**, *493*.
- (16) Long, Z.; Miyake, J.; Miyatake, K. Partially Fluorinated Polyphenylene Ionomers as Proton Exchange Membranes for

- Fuel Cells: Effect of Pendant Multi-Sulfophenylene Groups. *ACS Applied Energy Materials* **2019**, *2* (10), 7527–7534.
- (17) Bi, C.; Zhang, H.; Xiao, S.; Zhang, Y.; Mai, Z.; Li, X. Grafted Porous Ptfе/Partially Fluorinated Sulfonated Poly (Arylene Ether Ketone) Composite Membrane for Pemfc Applications. *J. Membr. Sci.* **2011**, *376* (1–2), 170–178.
- (18) Sankir, M.; Kim, Y. S.; Pivovar, B. S.; McGrath, J. E. Proton Exchange Membrane for Dmfc and H₂/Air Fuel Cells: Synthesis and Characterization of Partially Fluorinated Disulfonated Poly (Arylene Ether Benzonitrile) Copolymers. *J. Membr. Sci.* **2007**, *299* (1–2), 8–18.
- (19) Balogun, E.; Mardle, P.; Nguyen, H.; Breitwieser, M.; Holdcroft, S. Catalyst Layers for Fluorine-Free Hydrocarbon Pemfcs. *Electrochim. Acta* **2022**, *401*.
- (20) Chae, J. E.; Yoo, S. J.; Kim, J. Y.; Jang, J. H.; Lee, S. Y.; Song, K. H.; Kim, H.-J. Hydrocarbon-Based Electrode Ionomer for Proton Exchange Membrane Fuel Cells. *Int. J. Hydrog. Energy* **2020**, *45* (57), 32856–32864.
- (21) Jeong, H. Y.; Yang, D.-S.; Han, J. H.; Lee, J. Y.; So, S.; Suh, D. H.; Hong, S. K.; Hong, Y. T.; Kim, T.-H. Novel Interfacial Bonding Layers with Controlled Gradient Composition

- Profile for Hydrocarbon–Based Membrane Electrode Assemblies. *J. Power Sources* **2018**, *398*, 1–8.
- (22) Nam, S.–W.; Yu, D. M.; Kim, T.–H.; Lee, J. Y.; Nam, S. Y.; Hong, Y. T. Synthesis and Properties of Bonding Layer Containing Flexible and Fluorinated Moieties for Hydrocarbon–Based Membrane Electrode Assemblies. *Int. J. Hydrog. Energy* **2016**, *41* (25), 10884–10895.
- (23) Oh, K.–H.; Bae, I. Engineered Membrane–Electrode Interface for Hydrocarbon–Based Polymer–Electrolyte–Membrane Fuel Cells Via Solvent–Vapor–Annealed Deposition. *ACS Applied Nano Materials* **2019**, *2* (6), 3857–3863.
- (24) Oh, K. H.; Kang, H. S.; Choo, M. J.; Jang, D. H.; Lee, D.; Lee, D. G.; Kim, T. H.; Hong, Y. T.; Park, J. K.; Kim, H. T. Interlocking Membrane/Catalyst Layer Interface for High Mechanical Robustness of Hydrocarbon–Membrane–Based Polymer Electrolyte Membrane Fuel Cells. *Adv Mater* **2015**, *27* (19), 2974–2980.
- (25) Yuk, S.; Yuk, J.; Kim, T.–H.; Hong, Y. T.; Lee, D.–H.; Hyun, J.; Choi, S.; Doo, G.; Lee, D. W.; Kim, H.–T. External Reinforcement of Hydrocarbon Membranes by a Three–Dimensional Interlocking Interface for Mechanically Durable

- Polymer Electrolyte Membrane Fuel Cells. *J. Power Sources* **2019**, *415*, 44–49.
- (26) Cho, H.; Kim, S. M.; Kang, Y. S.; Kim, J.; Jang, S.; Kim, M.; Park, H.; Bang, J. W.; Seo, S.; Suh, K.-Y.; Sung, Y.-E.; Choi, M. Multiplex Lithography for Multilevel Multiscale Architectures and Its Application to Polymer Electrolyte Membrane Fuel Cell. *Nat. Commun.* **2015**, *6* (8484), 1–8.
- (27) Endo, T.; Reddy, L.; Nishikawa, H.; Kaneko, S.; Nakamura, Y.; Endo, K. Composite Engineering – Direct Bonding of Plastic Pet Films by Plasma Irradiation. *Procedia Engineering* **2017**, *171*, 88–103.
- (28) Ma, W.; Panecka, M.; Tufenkji, N.; Rahaman, M. S. Bacteriophage–Based Strategies for Biofouling Control in Ultrafiltration: In Situ Biofouling Mitigation, Biocidal Additives and Biofilm Cleanser. *J Colloid Interface Sci* **2018**, *523*, 254–265.
- (29) Zhang, L.; Tu, L. Y.; Liang, Y.; Chen, Q.; Li, Z. S.; Li, C. H.; Wang, Z. H.; Li, W. Coconut–Based Activated Carbon Fibers for Efficient Adsorption of Various Organic Dyes. *RSC Adv* **2018**, *8* (74), 42280–42291.
- (30) Ohkubo, Y.; Endo, K.; Yamamura, K. Adhesive–Free Adhesion between Heat–Assisted Plasma–Treated Fluoropolymers (Ptfе,

- Pfa) and Plasma–Jet–Treated Polydimethylsiloxane (Pdms) and Its Application. *Sci. Rep.* **2018**, *8* (1), 18058.
- (31) Ohkubo, Y.; Ishihara, K.; Shibahara, M.; Nagatani, A.; Honda, K.; Endo, K.; Yamamura, K. Drastic Improvement in Adhesion Property of Polytetrafluoroethylene (Ptfe) Via Heat–Assisted Plasma Treatment Using a Heater. *Sci. Rep.* **2017**, *7* (1), 9476.
- (32) Jung, H.–Y.; Kim, J. W. Role of the Glass Transition Temperature of Nafion 117 Membrane in the Preparation of the Membrane Electrode Assembly in a Direct Methanol Fuel Cell (Dmfc). *Int. J. Hydrog. Energy* **2012**, *37* (17), 12580–12585.
- (33) Choi, J.; Kyeong, M.; Kim, M.; Lee, S. S.; Seo, B.; Park, H. S.; Park, H. Y.; Henkensmeier, D.; Lee, S. Y.; Kim, H. J. Synthesis of Sulfonated Poly(Arylene Ether Sulfone)S Containing Aliphatic Moieties for Effective Membrane Electrode Assembly Fabrication by Low–Temperature Decal Transfer Methods. *Polymers (Basel)* **2021**, *13* (11).
- (34) S., R. R. R.; W., R.; M., K.; Y., W. W.; J., P. Recent Progress in the Development of Aromatic Polymer–Based Proton Exchange Membranes for Fuel Cell Applications. *Polymers (Basel)* **2020**, *12* (5).

- (35) Li, G.; Pickup, P. G. Ionic Conductivity of Pemfc Electrodes. *J. Electrochem. Soc.* **2003**, *150* (11), C745–C752.
- (36) Lefebvre, M. C.; Martin, R. B.; Pickup, P. G. Characterization of Ionic Conductivity Profiles within Proton Exchange Membrane Fuel Cell Gas Diffusion Electrodes by Impedance Spectroscopy. *Electrochem. Solid–State Lett.* **1999**, *2* (6), 259–261.
- (37) Malevich, D.; Jayasankar, B. R.; Halliop, E.; Pharoah, J. G.; Peppley, B. A.; Karan, K. On the Determination of Pem Fuel Cell Catalyst Layer Resistance from Impedance Measurement in H₂/N₂cells. *J. Electrochem. Soc.* **2012**, *159* (12), F888–F895.
- (38) Kabir, S.; Myers, D. J.; Kariuki, N.; Park, J.; Wang, G.; Baker, A.; Macauley, N.; Mukundan, R.; More, K. L.; Neyerlin, K. C. Elucidating the Dynamic Nature of Fuel Cell Electrodes as a Function of Conditioning: An Ex Situ Material Characterization and in Situ Electrochemical Diagnostic Study. *ACS Appl. Mater. Interfaces* **2019**, *11* (48), 45016–45030.
- (39) Wan, Z. H.; Zhong, Q.; Liu, S. F.; Jin, A. P.; Chen, Y. N.; Tan, J. T.; Pan, M. Determination of Oxygen Transport Resistance in Gas Diffusion Layer for Polymer Electrolyte Fuel Cells. *International Journal of Energy Research* **2018**, *42* (6), 2225–2233.

- (40) Baker, D. R.; Caulk, D. A.; Neyerlin, K. C.; Murphy, M. W. Measurement of Oxygen Transport Resistance in Pem Fuel Cells by Limiting Current Methods. *J. Electrochem. Soc.* **2009**, *156* (9), B991–B1003.
- (41) Liang, X.; Pan, G.; Xu, L.; Wang, J. A Modified Decal Method for Preparing the Membrane Electrode Assembly of Proton Exchange Membrane Fuel Cells. *Fuel* **2015**, *139*, 393–400.

Chapter 5. Conclusion

The dissertation introduced novel strategies using interfacial structures to address the obstacles to the commercialization of PEFCs. First, the interface multi-functional structure was introduced to effectively enhance the efficiency and chemical durability of MEA. By quenching the radical at the surface of the membrane, the structure effectively prevents chemical degradation without reducing the ion-conductivity of the membrane. Moreover, the structure enhanced mass transport within the CL and secured the membrane from dehydration under low RH conditions. Secondly, the vertically aligned 1-D ionomer-free electrode was introduced to utilize a nonplatinum catalyst with the ultra-low amount and prevent degradation of the electrode for AEMFCs. The electrode dramatically decreased oxygen transport resistance due to the vertically aligned 1-D oxygen path and ionomer-free catalyst surface. Also, the ionomer-free electrode showed a more stable operation compared to the conventional porous electrode showing ionomer degradation at the CL. Thirdly, mechanical and chemical modification strategy was introduced for hydrocarbon-based membrane. the modified membrane showed enhanced compatibility and adhesion strength with the PFSA electrode. Also, the interfacial resistance and oxygen transport resistance were greatly decreased, resulting in enhanced power performance.

As described above, the appropriate design and fabrication of interfacial structures effectively improve the electrochemical characteristics even when the same materials are used. Therefore, the novel design and fabrication of MEA with functional structures will lead to further innovation of PEFCs along with the development of functional materials.

Acknowledgments

This work was supported by the Global Frontier R&D program of the Center for Multiscale Energy System and Mid–Career Research Program by the National Research Foundation (NRF) under the Ministry of Science and ICT (MSIT), Korea.

초 록

고분자 전해질 연료전지는 높은 에너지 변환 효율과 탄소를 배출하지 않는 친환경 구동 등의 장점으로 인해 차세대 에너지원으로서 각광받아 왔다. 이에 지난 수십 년간 고효율 막전극접합체를 제작하기 위한 집중적인 연구가 진행되어 왔으며, 그 결과 연료전지 제작의 기술적 성숙도는 상용화 단계에 이르게 되었다. 하지만, 현재 막전극접합체의 제작엔 고가의 촉매와 막이 필수적으로 사용되어 고분자 전해질 연료전지의 제작 가격이 높은 문제가 있다. 또한 막전극접합체의 낮은 안정성, 특히 막과 전극에 사용되는 이온전도성 고분자의 화학적 열화 역시 중요한 문제이다. 이러한 문제를 해결하기 위한 지금까지의 막전극접합체의 비용 절감 및 수명 향상에 대한 접근 방식은 고분자 전해질 연료전지의 성능을 심각하게 저하시킬 수 있다. 이에, 성공적인 상용화를 위해서는 연료전지의 효율을 향상시키면서 제작비용이 낮고 안정성이 높은 막전극접합체를 제작하기 위한 전략이 필수적이다. 본 논문은 성능이 향상된 고내구, 저가 막전극접합체를 개발하기 위한 새로운 계면 구조 접근법을 소개하는 것을 목적으로 한다.

먼저, 고분자 전해질 연료전지의 화학적 내구성 및 성능을 동시에 향상시키기 위해 막과 전극의 계면에 다기능 구조를 도입하였다. 계면 구조를 제작하기 위하여 이온전도성 고분자 수지 및 라디칼 소기 나노 크기 입자를 전기분사법을 이용하여 분무하였다. 전기분사법에 의해 형성된 미세 액적은 다른 증착법과 달리 반데르발스 힘 및 정전력에

의해 막 형태가 아닌 수지상 구조로 적층되어 증착되었다. 그 결과, 상기 구조는 전기화학적 표면적을 증가시키고 마이크로 크기의 공극 공간을 형성하여 촉매층 내의 산소 전달을 향상시킴을 확인할 수 있었다. 또한, 이러한 구조는 막전극접합체의 탈수를 방지하여 낮은 상대습도 조건에서 고분자 전해질 연료전지의 출력 성능을 향상시키게 되었다. 무엇보다, 제작된 구조는 전극에서 발생하는 유해한 라디칼을 환원 시킴으로서 막전극접합체의 화학적 안정성을 향상시키게 되었다. 이러한 막전극접합체의 효율 및 화학적 안정성의 향상을 분석하기 위하여 in-situ 및 ex-situ 가속 열화 시험을 포함하여 다양한 분석을 진행하였다.

둘째, 전극내 고가 촉매 함량을 감소시키기 위하여 1 차원 나노구조로 ionomer-free 전극을 제작하였다. 이러한 전극을 제조하기 위하여 1 차원 나노 구조체를 수직으로 성장시키고, 극저량의 촉매를 균일하게 증착하였다. 음이온 교환막 연료전지의 양극으로 적용된 전극은 짧은 확산 경로와 ionomer 층의 부재를 통해 촉매 표면으로의 반응물의 질량 전달을 획기적으로 향상시켰다. 이렇게 제작된 전극의 효과를 분석하기 기존의 전극과의 전기화학 분석을 진행하였으며 그 결과 ionomer-free 전극이 막전극접합체의 전력밀도와 한계전류밀도를 크게 향상시킴을 확인하였다. 또한 ionomer-free 전극을 갖는 음이온 교환막 연료전지의 양극에서의 물 소비 및 산소 확산특성을 전극 두께를 변화시켜 집중적으로 분석하였다. 또, 내구성 시험을 통해 제작된 ionomer-free 전극층이 기존의 전극층 보다 안정하다는 것 역시 분석하였다.

셋째, 저비용 탄화수소계 막으로 고효율 막전극접합체를 제작하기 위해 새로운 표면개질 기술을 도입하였다. 고분자 스텐실과 플라즈마 조사를 이용한 부분 식각공정을 통해 마이크로 크기의 구조와 산소 작용기를 막 표면에 도입하였다. 탄화수소계 막과 기존의 과불소계술폰산 고분자 간의 결합강도 시험을 통해 마이크로 크기의 구조와 표면의 화학적 작용기가 결합강도를 향상시킨다는 것을 확인할 수 있었다. 또한, 개질된 막전극접합체는 ohmic 및 산소전달 저항이 감소하여 출력 밀도가 크게 향상되는 것을 확인할 수 있었다. Transmission line 모델을 적용한 분석으로부터, 향상된 계면 결합력이 전극의 박리를 방지하고 계면 및 촉매층에서의 저항을 감소시키는 것을 알 수 있었다. 또, 한계전류밀도에 대한 상세한 분석을 통해 개질된 막전극접합체가 전극 내에서 낮은 산소전달저항을 보이는 것을 확인하였다.